UNIVERSITÉ DE LORRAINE
École Nationale Supérieure des Industries Chimiques
Laboratoire Réactions et Génie des Procédés
École Doctorale RP2E

THÈSE

Présentée pour obtenir le grade de

Docteur de l'Université de Lorraine
Spécialité : Génie des Procédés et des Produits

Par

Yining WU

Sujet :

ÉTUDE DES PHÉNOMÈNES INTERFACIAUX À MICRO-ÉCHELLE

STUDY ON MICRO-SCALE INTERFACE PHENOMENA

Soutenue publiquement le 30 Juin 2015

Membres du jury

Rapporteurs Mme. Laurence TALINI, Maître de Conférences HDR (SIMM-ESPCI, Paris)
M. Hui LIU, Professor (University of Chem. Eng. of Beijing, Beijing, China)
Examinateurs M. Chao YANG, Research Director (IPE-CAS, Beijing, China)
M. Youguang MA, Professor (directeur de thèse, Tianjin University, Tianjin, China)
M. Huai-Zhi LI, Professeur (directeur de thèse, LSGC-ENSIC, Nancy)

ABSTRACT

The multiphase flow with various interfacial phenomena and complex fluid dynamics behaviors widely exists in numerous industrial processes. In recent years, the combination of the multiphase flow and microfluidics has been becoming a cutting-edge technology to gain new insight into various applications. The two-phase flow in microchannel is of prime importance in this technology. Thus this thesis systematically investigates the involved droplet (bubble) formation, secondary breakup and coalescence processes in two-phase microfluidic flow, by using a high speed digital camera. The content of the thesis is arranged as follows:

The first part of this thesis focuses on the active control of the ferrofluid droplet generation in a microfluidic flow-focusing device. The expanding and breakup dynamics of the thread of a controllable dispersed phase under different flow rates in a microfluidic flow-focusing device was studied. The influences of the flow rates, magnetic flux density and magnetic field direction on the formation and breakup processes were extensively investigated. The whole formation processes of ferrofluid droplets under no magnetic field (NM), radial magnetic field (RM) and axial magnetic field (AM) were investigated and compared. It was found that the volume of ferrofluid droplets can be actively controlled by the magnetic field. Both the radial magnetic field and axial magnetic field remarkably affect the expanding and breakup process of the thread, respectively. The variation of the minimum width of the ferrofluid thread with the remaining time could be scaled with a power law.

Subsequently, the breakup dynamics of ferrofluid droplet in a symmetric microfluidic T-junction under magnetic field and the feedback effect on the breakup of bubbles at a microfluidic T-junction were investigated experimentally. In the first part, the breakup dynamics of the ferrofluid droplet under magnetic fields was studied. The whole breakup processes of the ferrofluid droplets under uniform and non-uniform magnetic fields were exhaustively considered. The influences of both the flow rates and magnetic flux density on the breakup were studied. Results showed that the type of breakup process could be changed and the breakup frequency of ferrofluid droplets could be actively modulated by applying a uniform magnetic field. While under

non-uniform magnetic field, the asymmetric breakup of ferrofluid droplets could be realized. The non-uniform magnetic field can exert attraction on ferrofluid droplets in a dissymmetrical way to avoid breakup. In addition, the asymmetrical breakup processes of bubbles without external field at a microfluidic T-junction divergence were also studied. The asymmetrical breakup stems from the feedback effect of bubble behaviors at the T-junction convergence in a loop with the symmetrical branches. The feedback effects of asymmetrical collision and staggered flow of bubble pairs on bubble behavior at the T-junction divergence were mainly investigated. The result showed that the feedback effect is negligible at relatively low flow rates when no collision of bubble pairs occurs. And the bubble pair asymmetrical collision at T-junction convergence or an amplified effect of structured blemish of microchannel at relatively high flow rates is primarily responsible for the asymmetric breakup of bubbles at the T-junction divergence.

Next, the emphasis is on the generation of satellite droplet (bubble). Firstly, the formations of satellite droplet during neck filament thinning in a microfluidic flow-focusing and a T-junction were investigated. In this part, the breakup dynamics of the neck during droplet formation process in a flow-focusing junction and droplet breakup process in a T-junction were primarily concerned. The results demonstrated that these exists an inevitable slow thinning process in last stage due to a new balance between viscous force and capillary force and the neck filament maintains a roughly constant volume in last stage. The final breakup point no longer locates at the center of the neck, in turn, the breakup occurs at the two ends of the neck caused by uneven surface tension generating a satellite droplet. The size of the satellite droplet is proportional function of the capillary number of the continuous phase. Secondly, the satellite droplets (bubbles) stemming from the shear-induced tail breakup of droplets (bubbles) flowing in a straight microfluidic channel were studied. The study is mainly focused on the influences of both the discrete droplets (bubbles) size and two-phase average flow velocity on the formation of tip stream in the rear of a droplet (bubble). It was found that the droplet deformation increased with the droplet length or the capillary number. There exists a critical droplet (bubble) length dependent on capillary number, beyond which the tip stream ejecting tiny daughter droplets (bubbles) will take place. The generated tiny droplets are usually three orders of magnitude smaller than primary droplet.

The final part of this thesis aims at the coalescence of droplets (bubbles). At first, bubble coalescence at a microfluidic T-junction convergence was presented. The responses of bubble collisions at the T-junction convergence have been investigated within a wide range of dimensionless bubble size and capillary number *Ca*. Colliding coalescence, squeezing coalescence and non-coalescence were observed at the junction. The results showed that for whatever colliding coalescence or squeezing coalescence, the coalescence efficiency decreased with the increase of the two phase superficial velocity in moderate liquid viscosities, and the transition from colliding to squeezing coalescence due to the increase of the two phase superficial velocity enhanced the coalescence of bubbles. The decrease of the bubble size and the augment of the liquid viscosity were not conducive to the coalescence. Then the coalescences of ferrofluid droplets under various magnetic fields were investigated. A continuous dripping ferrofluid from a capillary was studied in this work under various magnetic fields applied. The emphasis was given to the consecutive coalescence and breakup between two coaxial ferrofluid droplets with conic edges attracting one another under applied magnetic field. By means of a high-speed digital camera, it could be observed that a small amount of ferrofluid would pierces the tip surfaces of the approaching droplet cones and then forms a liquid bridge or neck with a visible gap in the order of tens of micrometers between the leading edges. The inertia of the ferrofluid originating from the magnetic attraction fields becomes the driving force at the initial stage of coalescence instead of capillary force. After the coalescence, a ferrofluid column was formed; A critical magnetic flux density above which the column will collapse was found and different pinch-off patterns were observed by varying the intensity of magnetic flux density.

KEY WORDS： microfluidic, droplet, bubble, satellite droplet, ferrofluid, formation, breakup, coalescence

摘　要

多相流广泛存在于多种工业过程中，其通常伴随着界面现象与流体力学相互耦合。 近年来，将多相流与微流控技术结合已逐渐成为一种前沿技术，具有广泛的应用前景。微通道内两相流是该领域的重要研究内容。本文利用高速摄像仪研究了微通道内液滴（气泡）的生成，破裂及聚并过程。具体研究内容包括：

第一部分主要研究了磁场调控下聚焦型微通道内磁流体液滴的生成过程。重点关注了磁流体液滴在通道内的扩张及破裂动力学行为。考察了流体流速、磁场强度及磁场方向对扩张及破裂的影响。研究并比较了无磁场（NM）、径向磁场（RM）和轴向磁场（AM）下的液滴形成过程。结果发现，磁流体液滴的体积可通过所施加的磁场来进行有效调控。径向磁场和轴向磁场分别通过影响液滴的扩张阶段和破裂阶段来影响液滴的尺寸。磁流体破裂过程的颈部最小宽度与剩余时间呈幂指数关系。

第二部分研究了磁场对磁流体液滴破裂的影响以及反馈作用对气泡破裂的影响。首先研究了匀强磁场及非匀强磁场下 T 型微通道分叉处磁流体液滴破裂动力学。研究发现在匀强磁场下，可以通过改变磁场强度来调控液滴破裂方式以及液滴破裂频率。在非匀强磁场下，通过改变磁场强度可以调控液滴破裂的不对称度从而使液滴的临界破裂点发生迁移。此外，还研究了气泡在 T 型微通道分叉处的不对称破裂行为。气泡不对称破裂行为主要归因于破裂所形成的子气泡在下游通道内动力学行为的反馈作用。考察了下游汇聚口处子气泡碰撞以及交替通过出口时的反馈作用对破裂的影响。结果表明，当流速较小且子气泡不发生碰撞时，反馈作用可以忽略。当子气泡在下游汇聚口出发生碰撞时反馈作用较为明显。此外，在高流速下通道瑕疵所带来的影响亦不可忽略。

第三章研究了卫星液滴（气泡）的生成过程。本章前半部分主要关注聚焦型和 T 型微通道内液-液界面收缩破裂过程中形成的卫星液滴。实验结果表明，在颈部夹断后期，由于粘性力和表面张力的平衡和强弱转换，液滴的颈部不可避免从快速夹断区进入慢速断裂区。研究发现在慢速夹断区颈部的体积几乎保持不变，最细颈部位置也由中间过渡到颈部细丝的两侧，最后在颈部细丝两侧发生断裂并形成卫星液滴。在实验范围内卫星液滴尺寸随连续相毛细数的增长而增长。其后研究了直通道内剪切力引起的液滴（气泡）尾部断裂过程。重点关注了液滴（气泡）尺寸及流速对尾部尖端流的影响。结果表明，随着液滴（气泡）的尺寸或毛细数的增长，其形变愈发显著。存在一个临界毛细数，当大于这一数值，液滴（气泡）尾部将发生破裂并产生尖端流。由尖端流所生成的卫星液滴的尺寸通常比主液滴小三个数量级。

论文的最后部分研究了液滴（气泡）的聚并过程。首先研究了气泡在 T 型微通道汇聚处的聚并行为。在不同的毛细数及气泡尺寸下，实验观测到了三种主要行为：碰撞式聚并、挤压式聚并及不聚并。实验结果表明，中等粘度下不论是碰撞式聚并还是挤压式聚并，其聚并效率都随两相表观流速的增加而降低。两相表观流速的增加将致使碰撞式聚并过渡到挤压式聚并，同时聚并效率小幅增加。此外，连续相粘度的增加或者气泡尺寸的减小都会降低聚并效率。此外，研究了磁流体液滴在不同磁场强度下的聚并过程。两个同轴的磁流体液滴在磁场作用下相互吸引并变形为圆锥体。实验重点关注了两个圆椎体液滴相互靠近相继发生聚并及断裂的过程。通过高速摄像仪发现当液滴之间的距离在 10 微米左右时液滴相互靠近的界面会形成柱状突起并在两个液滴间形成搭桥。实验结果表明，磁流体液滴聚并的推动力为惯性力而不是表面张力，磁流体液滴聚并后会形成液柱。存在一个临界磁场强度，高于临界磁场强度磁流体液柱将变得不稳定甚至发生破裂，液柱破裂的形式与磁场强度有关。

关键词：微流体；液滴；气泡；卫星液滴；磁流体； 生成；破裂；聚并

Table of Contents

Introduction

From the second half of the 20th century, one of the most important developing trend in engineering technology is miniaturization. For instance, the revolution in computation by miniaturization of electronic circuits contributes the prevalence of personal computer and our society profits from this advancement. Similarly, the miniaturization of the fluidic units was motivated in the later of the 20th century. Subsequently, the concept of Lab-on-a-chip (LOC) or micro-Total Analysis Systems (μ-TAS) was put forward. The reason why researchers put emphasis on LOC is its inherent advantages. The miniaturization affords many profits including reduced reagent consumption, shorter analysis time, improved sensitivity, easier flow manipulation, easier engineering enlargement through massive parallelization. But due to the lack of fabrication facilities and high cost the engineering applications were limited for a long time in ink-jet printers and gas chromatography [1-3]. Recently, based on the developments in fabrication technique in the microelectronics industry, the micro-devices could be fabricated in glass or silicon or other materials by soft lithography and precise milling. Meanwhile, the performance of conventional macro-size devices cannot satisfy the demand from biomedical research. Consequently, the development of LOC devices has intensified over the past decade. Now, LOC devices have attained a number of applications in clinical diagnostics, drug discovery, chemical synthesis, genetics research, protein research, and toxic substance detection [4-8]. Moreover, the combination of LOC concept and chemical engineering as micro-chemical technology is becoming a new development direction. Remarkable number of research work has been focused on the micro-emulsification, micro-mixer, micro-heat exchanging and micro-reaction etc[9-23]. Simultaneously, several companies such as IMM, DUPONT, BASF, PNNL pumped capital into microfluidic technology to commercialize their microfluidic devices and to make the way to the marketplace.

Although some achievements have been made, there are still many challenges. Due to scaling down, the characteristics of the flow in micro-sized space are deviated from the flow in macro-sized space. The dominant forces shift from gravity and inertia

forces on the macro scale to the viscous and capillary forces on the micro scale. For example, the Reynolds number ($Re=\rho UL/\mu$) and Bond number ($Bo=\Delta\rho g d^2/\sigma$) in microfluidic devices are typically very small ($Re<<1$, $Bo<<1$) and therefore the flow is strictly laminar and buoyancy force is relatively small. These differences demand a fully understanding of the fluid dynamics information in micro-scale as the base of the aforementioned engineering application, the flow in micro-sized space still needs to be systematically studied. In this thesis, the dynamics of the formation, breakup and coalescence of droplets (bubbles) in different microchannels were studied, respectively.

Chapter 1 Literature Review

Multiphase flow due to the presence of interface brings in complex phenomena that have a long history in fluid mechanics. Several significant studies such as Laplace and Young's study of the wetting and capillarity, Rayleigh and plateau's study of the instability of a liquid thread, Taylor's study of the breakup of droplet in shear and elongation flows, and Bretherton's investigation into segmented flows in capillaries show the rich contents of multiphase flow[24-26]. In this thesis, the emphasis is mainly put on the multiphase flow in microchannel namely multiphase microfluidics. Multiphase microfluidics is the field of research and technology that deals with the manipulation of multiphase flow in channels with dimensions typically smaller than a millimeter. The foremost of the multiphase microfluidics is two-phase flow in microchannel.

Microdroplets and microbubbles have been a hot area of research in two-phase microfluidics [2, 27]. One of the ideas behind microdroplet characterized by such small length scales is to increase the surface -to-volume ratio [27, 28]. And each microdroplet (microbubble) is essentially an attractive micro reactor that compartmentalizes reagents preventing them from diffusing away when it passes through the conduits of a microfluidic network. Under well-defined wetting conditions, droplets are separated from the channel wall by a thin film of carrier fluid which prevents adsorption and cross-contamination between droplets and the channel walls. Furthermore, the small size of the droplets usually over a range of picolitres to nanolitres results in minimal consumption of materials and excellent dictation of reactants [29, 30]. Mixing is also enhanced due to the formation of counter rotating vortices by shear force within moving droplets [31].The precise manipulation of microdroplet's (microbubble's) size plays a pivotal role in removing the barrier for engineering applications. In this thesis, the droplet's (bubble's) formation, breakup and coalescence processes were systematically studied.

1.1 Changes due to scaling down

1.1.1 Change of the relative importance of the four forces

The behaviors of microdroplet (microbubble) were influenced by the operating conditions, fluids properties, surface and geometries of the channel [32-36]. Nevertheless, there exists scaling law of general form to predict the flow pattern, the droplet size and the critical breakup length etc. within certain limits [32-36]. The reason is that under micro-scale the primary forces in different processes which have crucial influence on the two-phase flow are the same. Usually, a balance exists in two-phase flow between four primary forces: viscous shear, interfacial tension, inertia, and buoyancy. The relative importance of these forces is characterized by some dimensionless numbers for instance the Reynolds number (inertia/viscous), capillary number (viscous/interfacial), Bond number (buoyancy/interfacial), Weber number (inertia/interfacial), Ohnesorge number (viscous / (interfacial* inertia) $^{0.5}$) [6, 37-41]. These dimensionless numbers are summarized in Table 1.1. Due to the tiny characteristic length, low flow velocities and high surface-to-volume ratio in micro flow, inertia and gravity forces become insignificant compared to viscous and interfacial forces. Thus the capillary number is the most useful descriptor for analyzing micro scale two-phase flow phenomena including droplet formation, breakup, coalescence and transport. It evaluates the competition between viscous stresses, acting to elongate the interface, and surface tension attempting to minimize the surface area. Typically, the capillary number is calculated from the properties of the continuous phase.

Table 1.1Summary of relevant dimensionless numbers in micro scale two-phase flow

Dimensionless number	Equation	Definition
Reynolds	$\mathrm{Re} = \frac{\rho d u}{\mu}$	inertia/viscous
Capillary	$Ca = \frac{\mu u}{\sigma}$	viscous/interfacial

Bond	$Bo = \frac{\Delta\rho g d^2}{\sigma}$	buoyancy/interfacial
Weber	$We = \mathrm{Re}\,Ca = \frac{\rho u^2 d}{\sigma}$	inertia/interfacial
Ohnesorge	$Oh = \frac{\mu}{(\rho d\sigma)^{1/2}}$	viscous/(interfacial* inertia)$^{0.5}$

Günther & Jensen (2006) studied the variation of *Bo* in several microchannels with different sizes. The results demonstrated that the *Bo* << 1 in micro scale channel, which means the gravitational force is neglected as shown in Fig.1.1a. Furthermore, they analyzed the variation tendency of *Ca, We* and *Bo* under different operating conditions and different channel sizes; they confirmed the crucial role of the viscous force and interfacial force (Fig.1.1b).

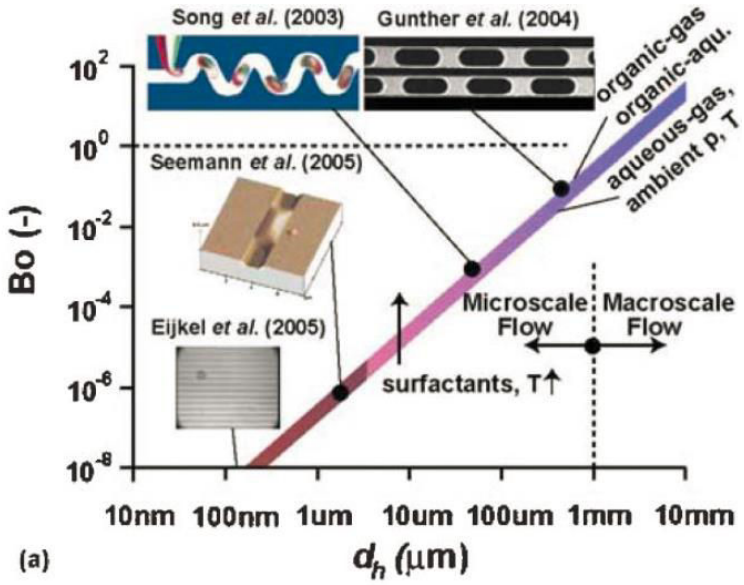

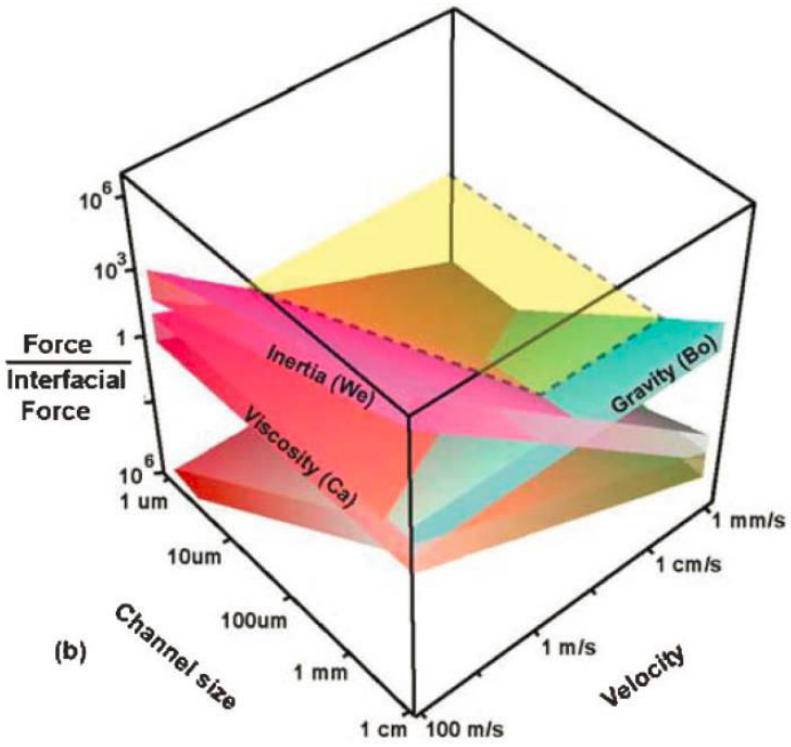

Fig. 1.1 (a) Variation of Bond number with different channel size (b) Influence of inertia, viscous and gravity forces with respect to interfacial forces in multiphase microfluidic systems (Günther et Jensen (2006))

1.1.2 Confinement

The previous literature indicates the droplet or bubble has minimal influence on the flow field and the flow field away from the vicinity of the interface will quickly reach a bulk value in the context of unbounded flows. While in microscale flow where the close proximity of the channel walls strongly influences the fluid dynamics, the situation is totally different. As show in Fig.1.2a, during the droplet formation process, the interface of the droplet occupies a large space and deviates from sphere due to intense confinement from the channel wall. Similarly, the breakup of microdroplet in microchannel (Fig.1.2b) confronts the same situation. This fierce confinement helps suppress the occurrence of hydrodynamic instabilities. Simultaneously, droplets occupy the majority of the microchannel cross-section they also influence the global pressure and flow fields (Fig.1.2). The role of confinement is an interesting aspect of multiphase flow in microchannels. Precisely due to the confinement, the microbubbles and microdroplets have less degree of freedom compared to their counterparts in macro scale. As a consequence, the degree of the interface stability and the

mechanism that leads to break-up of the interface are not the same for confined and unconfined bubbles and droplets.

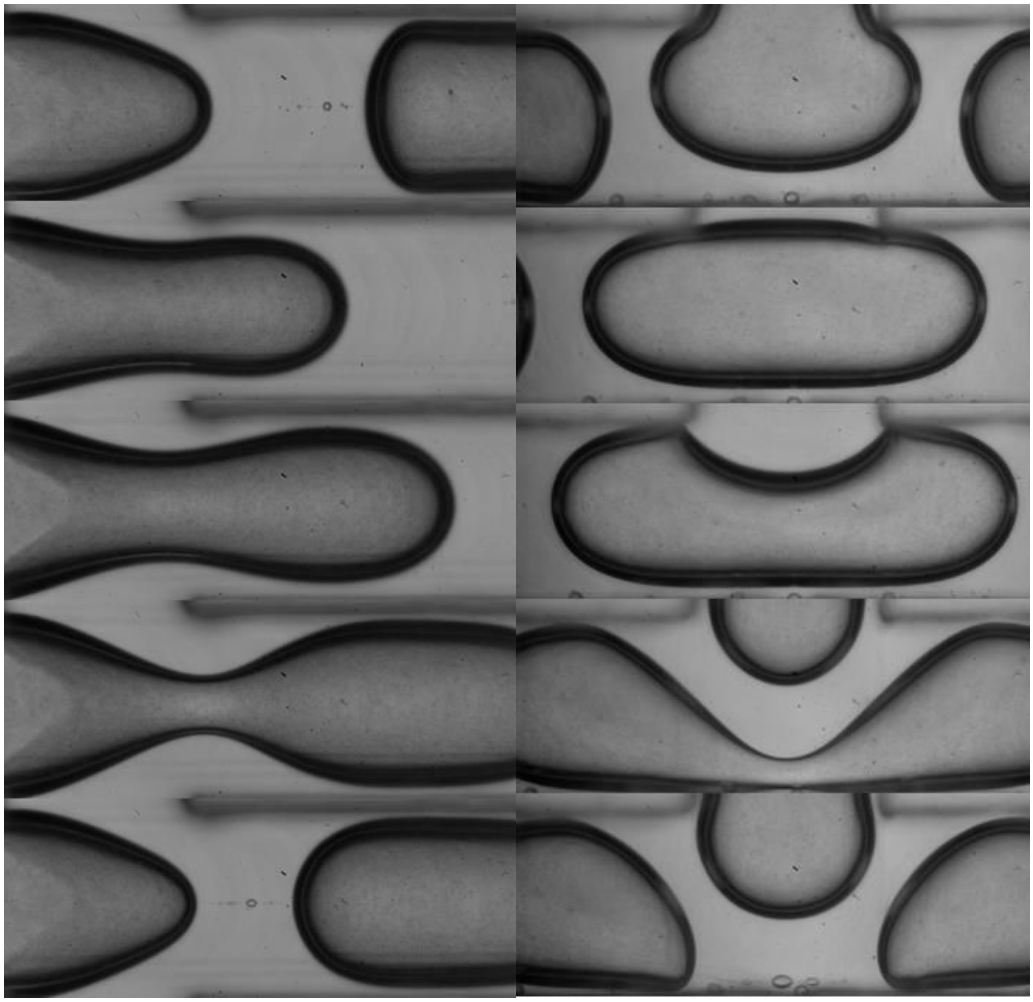

(a) (b)

Fig. 1.2 (a) Droplet formation process in flow-focusing microchannel and (b) droplet breakup process in T-junction microchannel

1.1.3 Specific surface area

Decreasing the scale of a flow to the range of micrometres certainly leads to high specific surface area. The specific surface area of two-phase flow in the microchannels may reach 10000 to 50000 m^2 / m^3, while it is usually of the order of 1000 m^2 / m^3 for laboratory reactors and 100 m^2 / m^3 in commercial unit[42]. High specific surface area induces a larger exchange surface: the transfer of heat and mass will be intensified at this scale. Surface effects will take a more prominent place in the system compared to the macro scale and will dominate volume effects. Indeed, the

ratio of the surface forces to the body forces is proportional to the inverse of the characteristic length of the system, resulting in an important increase of the surface effects when the size of the system decreases.

1.1.4 Wettability and Surfactants

As we have seen, the channel walls are of considerable importance to the micrometer scale. Characteristics such as wettability and slip in the surface of channel wall, with less emphasis on macro scale cannot be ignored.

1.1.4.1 Wettability

In microchannels, the walls in close proximity raise the importance of the wettability. From a static point of view, when a droplet is in equilibrium on a solid surface, three phases are present (Fig.1.3). If the droplet only partially wets the surface wetting is then characterized by an angle of contact defined by the relationship of the Laplace-Young: $\sigma_{lg}\, cos\theta = \sigma_{sg} - \sigma_{sl}$ here σ_{lg} , σ_{sg} , σ_{lg} denote the surface tension of Liquid/Gas, Solid/Gas, Liquid/Gas, respectively.

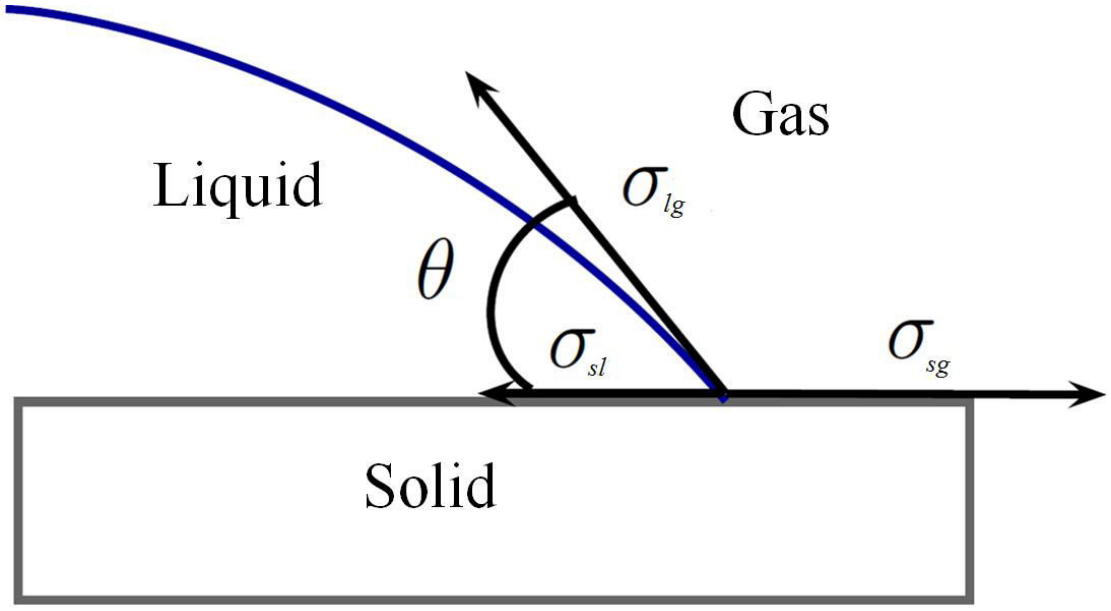

Fig. 1.3 Contact angle on a flat surface

If the contact angle is zero, the liquid spreads completely on the solid surface. On the contrary, if θ = 180˚, the liquid does not spread on the surface and remains, if the volume is quite low, in the form of a perfect sphere on the surface on which it is

deposited. The intermediate values of contact angles reflect a partial wetting roughly good (for poor wetting contact angles at 90˚). The wettability of the walls will therefore take an important place in the microchannels, in particular for the case of two-phase bubbles or droplets. Wetting conditions are parameters which determine the flow pattern. To illustrate, the material constituting the micro-structured system determines the type of emulsion that can be formed in microchannels. The hydrophilic walls of microsystems will promote the formation of direct emulsions (i.e. oil in water), while hydrophobic walls of microsystems, such as PAAM, encourage inverse emulsions (i.e. water in oil). The fluid that preferentially wets the walls had better serve as the continuous phase. To work around these conditions, the technologieswhich modifies the surface properties of the walls have been used. For example, Barbier et al. transformed the PDMS surface from hydrophobic to hydrophilic by a low pressure plasma reactor [43]. The surface properties of the PDMS were able to be controlled and keeping a stable hydrophilic surface for several days. The flow regimes changed drastically by varying the wetting condition. The use of suitable materials in terms of wetting conditions facilitates the control of the flow pattern.

1.1.4.2 Surfactant

Wetting conditions may be modified by the addition of a surfactant with a certain concentration, due to the adsorbing of the surfactants at the liquid / solid interface. Dreyfus et al. have changed the flow pattern by varying the wetting conditions though altering the concentration of surfactants [44].

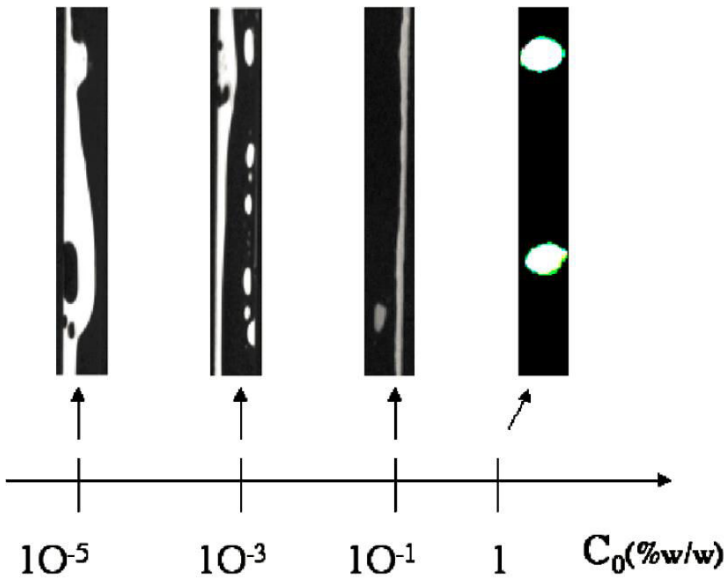

Fig. 1.4 Evolution of the flow patterns with the span 80 concentration (Dreyfus et al. (2003))

The presence of surfactant does affect not only the properties of the fluid / walls interfaces, but also the properties of the interface between two immiscible fluids in the case of movement of droplets or bubbles in microchannels. Indeed, the stability of the droplets can be modified by the kinetics of the diffusion of a surfactant to the interface. The purpose of this study is to decrease the consumption of surfactants during producing micro-emulsification while simultaneously, to limit the coalescence of droplets.

1.2 Droplet and bubble

Droplet (bubble) is the foundation of engineering application of microfluidics. An integrated microfluidic device usually contains droplet (bubble) generation, breakup and coalescence processes. These processes are results of a complex interplay between viscous, capillary, electrostatic and van der Walls forces over a wide range of spatial and time scales. Thus on the one hand the complexity of these processes is inevitable. On the other hand, it is necessary to precisely manage these processes. Therefore many researchers put emphasis on this field. Recently, passive methods have been developed to induce formation, breakup and coalescence of droplets. Active techniques based on thermocapillary, magnetic, optical trapping, electrophoresis and electrophoresis can also be used to control droplets. Below the

various passive and active methods for generating, splitting and merging droplets are summarized.

1.2.1 Droplet (bubble) formation

The dispersion of a liquid (gas) into another immiscible one in a microfluidic device is usually a basic and necessary operation to form droplets or bubbles. Compared with traditional production equipment, the microfluidic devices with the advantages of the controllability, small size and producing monodispersed droplets attract much attention [32, 36, 39, 45]. In micro device, the length scales of the channels are comparable to the size of the droplets being formed. Moreover, the flow in microchannel is laminar, which is highly controllable and stable. These characters endow microfluidic droplet generators with the high degree of controllability. According to the governing factors, the methods to generate microfluidic droplet or bubble may be divided into passive and active types. Below, we will give the detailed discussion to presents the most common types of droplet generators.

1.2.1.1 Passive method

Passive method means the droplet formation is determined by the geometry of the generators. Next, we will present three common types of droplet generators used in microfluidics: co-flowing (Fig.1.5a), cross-flow (Fig.1.5b) and flow-focusing (Fig.1.5c) designs.

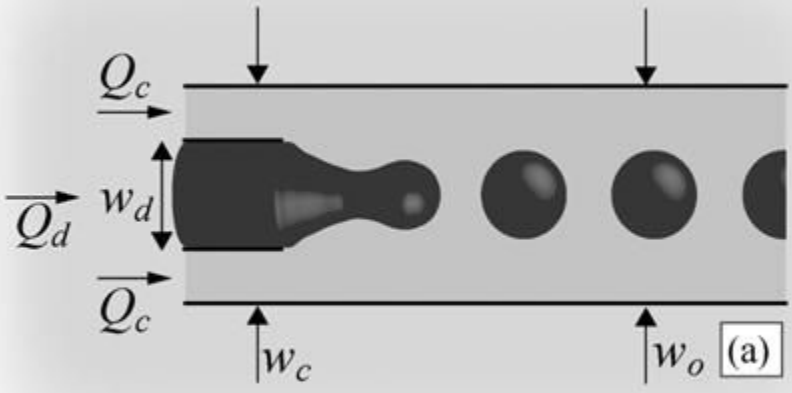

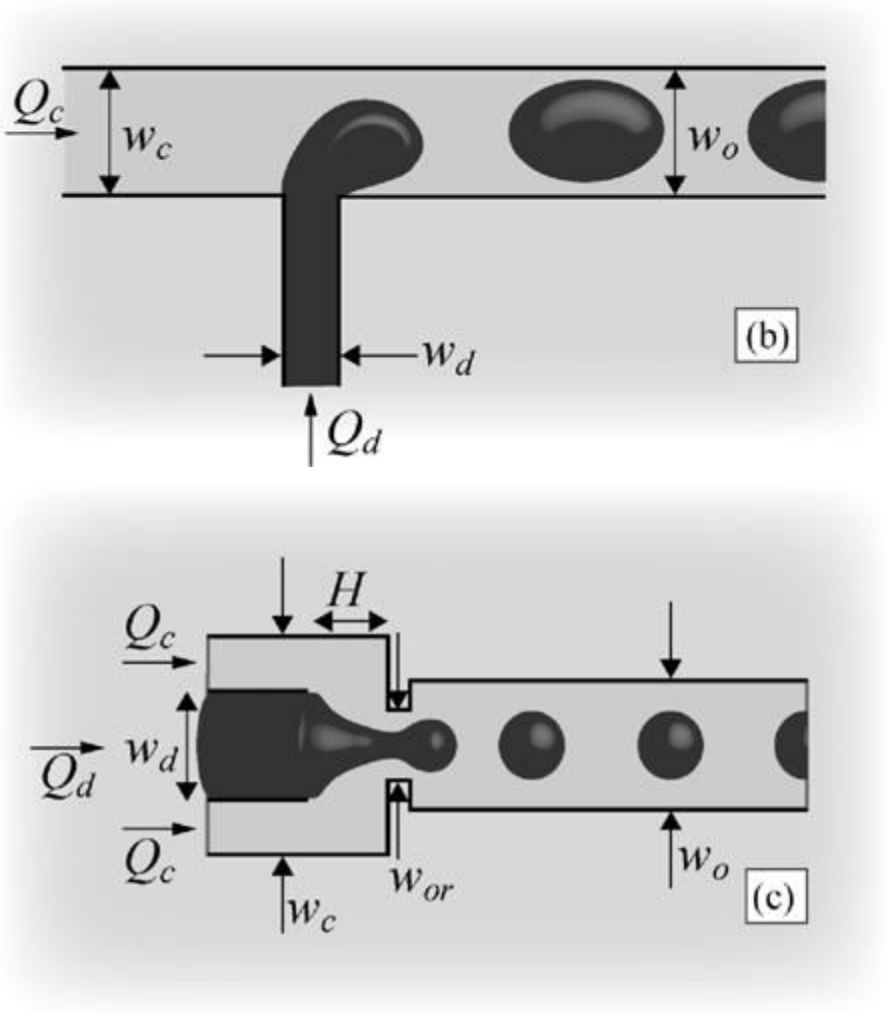

Fig. 1.5 Formation of droplets in microchannel (Christopher and Anna (2007))

Co-flowing designs

The co-flowing microfluidic device consists of two concentric capillaries with the inner channel carrying the dispersed phase and the continuous phase in the outer. As the dispersed phase enters the main channel the viscous stresses created by the continuous phase stretch the interface until it breaks forming a droplet. Cramer et al. found that there are two distinct droplet generating regimes: (a) dripping, where the droplet pinches off near the capillary tip, and (b) jetting, where droplet breakup occurs at the end of an extended liquid thread. A critical velocity exists that defines the transition between the two regimes [46, 47]. Guillot et al. systematically studied the transition between the dripping regime and the jetting regime using lubrication theory and found that the transition is caused by a change in the breakup mechanism from an absolute instability to a convective instability [48-50]. At lower Reynolds number the wave created by the Rayleigh-Plateau instability is able to propagate in both

directions resulting in pinch off first near the capillary tip. While at higher Reynolds number the wave is transported downstream thus leads to the elongation of the thread. The transition point between the two regimes is a function of the viscosity ratio, capillary number and the degree of confinement the jet experiences in the outer channel [48-50]

Furthermore, the co-flow is a perfect micro structure for generating double emulsions in a single step as show in Fig.1.6. Simultaneously, it allows the precise control of the outer and inner drop sizes as well as the number of droplets encapsulated in each larger drop [10]. However, co-flowing design is not often used in planar microfluidic chips due to the difficult fabrication process to maintain the concentrically aligned capillaries within the microchannels.

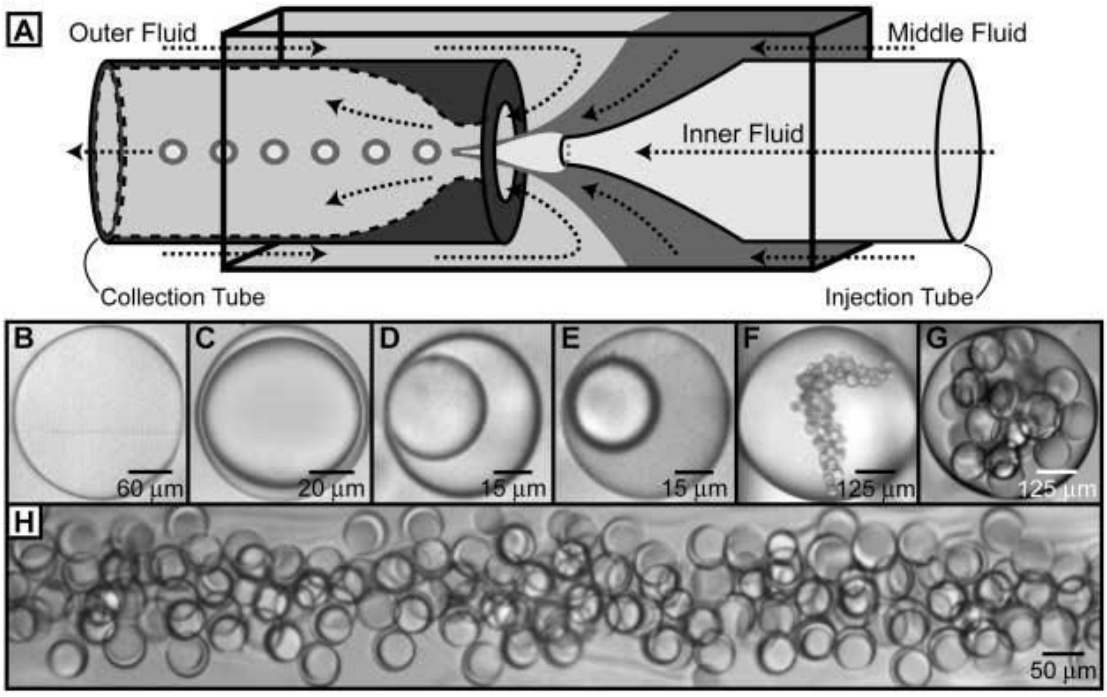

Fig. 1.6 Formation of double emulsions in microchannel (Utada et al. (2005))

Cross-flow Designs

Thorsen et al. were the first researcher to use cross-flow to generate aqueous droplets in oil phase [51]. In cross flow designs, the continuous phase channel and the dispersed phase channel meet at a junction where they are forced to flow into a single exit channel. Under pressure driven flow the interface is injected into the main channel

where shear forces created by the cross-flowing oil phase elongates the interface downstream until eventually a droplet breaks off. Thorsen et al. presented a predictive model of the diameter of the new formed droplet [51]:

$$d \propto 2\sigma / \mu_c \gamma \tag{1-1}$$

Here d, σ, μ_c and γ denote the diameter of the droplet, interface tension, viscosity of continuous phase and the shear rate, respectively. Subsequently, some other researchers studied the formation process in succession [52-55].

There are three mechanics of droplet (bubble) formation in T-junction generators: squeezing (confined regime), dripping (unconfined regime) and jetting. The transformation between these regimes is a function of the Capillary number and the flow ratio between two phase [56-59].

The squeezing (confined) regime usually locates at low capillary number and high flow rates ratio of dispersed phase to continuous phase. In this regime, the dispersed phase will form a large size droplet (bubble) and occupy the entire main channel quickly. Then, the new generated droplet penetrates to downstream, simultaneously, begins to influence the local flow field significantly. During this period, the surface tension forces always overwhelm the squeezing pressure. Subsequently, due to the obstruction, the squeezing pressure augments launching the necking process until the last pinch-off. Drops formed in the squeezing regime are designated as slugs (length greater than the channel width). Droplet formation in this regime is determined by the structure of the T-junction generator and the flow rate ratio [53]. Garstecki et al. found the augmented pressure in continuous phase due to obstruction is the principle driven force promoting the final pinch-off. And according to this they developed a scaling law that captures the physics of the process: $L = W_c + dQ_d/Q_c$, where L is the length of the plug, W_c the width of the main channel, d the width of the neck and Q_d, Q_c, are the dispersed and continuous phase flow rates, respectively. This equation implies that the process is only influenced by the flow rate ratio and is independent of either the capillary number or viscosity ratio, which already have been verified [54, 57].

van der Graaf et al. investigated the formation of a droplet in T-junction by the lattice Boltzmann method[60]. They developed a two-step process model to predict the droplet size. In their model, the first step is in the force balance; the droplet grows to a

critical volume V_g at the end of the first step. Then the droplet glows continuously for a period t_c, until final pinch-off: $V= V_g+ t_c Q_d$. Once the flow rate of continuous phase is superior to the counterpart, the pattern enters the dripping (unconfined) regime. Confinement is not an important issue in this regime. Usually, the main channel is wider than the perpendicular channel. Droplet breakup is governed by the balance between the shear force on the emerging droplet that penetrates into the main channel and the surface tension resisting detaching of the newly formed droplet. Experimental results show that droplet size depends strongly on the continuous phase flow rate but weakly on the disperse phase flow rate in the dripping regime. Recently, Xu et al. has built models that bridge the gap between the squeezing and dripping regimes; they consider that the formation process is governed by the capillary number and the flow rates ratio of dispersed phase to continuous phase [61]. In the squeezing regime the model of Garstecki et al. proposed an empirical correlation which works well with experimental data.

Jetting occurs at high capillary numbers where viscous force is superior to surface tension. In jetting regime the dispersed phase penetrates into main channel and its thread never recoils and remains in downstream. To produce monodispersed droplets, the generator is often operated in the dripping or squeezing regimes. The main difference between these two regimes is the degree of confinement that the droplet experiences when it forms.

Flow-Focusing designs

Anna et al. (firstly use the flow focusing geometry in a planar microfluidic chip to produce emulsion [45]. In this design, the dispersed phase is introduced from the central main channel at a flow rate of Q_d and the continuous phase is driven into two branches with the same flow rate $Q_c/2$. These three flow streams focus at the intersection downstream to generate droplets. The continuous phase flows symmetrically about the center channel of dispersed phase, which results in more symmetric shearing which improves stability and control over droplet formation. There are also three mechanics of droplet (bubble) formation in Flow-Focusing designs: squeezing, dripping and jetting. The transformation between these regimes depends on the flow rate ratio of dispersed phase to continuous phase.

The squeezing regime appears when the flow rate ratio is relatively high (φ>1) so the dispersed phase is the dominant phase in the microchannel. The breakup process is as follows. Firstly, the dispersed thread expands in both the axial and radial directions in the intersection region. The tip of the thread is reminiscent of a half dome. Secondly, the expanding thread reaches the edges of the outlet channel and continues to move downstream with the outlet channel blocked. During this time the continuous phase thins the dispersed thread in the radial direction and elongates it in the axial direction until the presence of the neck. Thirdly, the neck forms and thins progressively. In this process, the film between the thread tip and the wall of outlet channel becomes very thin. Finally, the neck pinches off until to form a new droplet. As the continuous phase flow rate is increased the flow focusing generator operates in the dripping regime. In this regime, the interface extends to downstream with an obvious film between the droplet and channel walls. The final breakup occurs away from the center channel. After breakup the remaining interface does not retract. Droplets are typically smaller than the outlet channel's width with a high monodispersity. Breakup occurs due to a combination of capillary instabilities and the viscous drag effects on the detaching droplet.

As the increase of the continuous flow rates, jetting occurs when the length of thread of dispersed phase elongating downstream is several times than the channel width. The transition between dripping and jetting is believed to occur when the viscous stresses on the interface are large enough to convey instabilities downstream before they are formed. In the jetting regime droplets are less uniform than droplet in other regimes as breakup is more erratic.

1.2.1.2 Active Methods

Currently, there are two primary active methods to control the droplet (bubble) formation process. First, the external fields for instance: electrical field, magnetic field and laser heating etc. are utilized to exert body forces or surface forces to manipulate the generation. The second method usually utilizes the sudden change of the generator geometry taking pneumatic chamber for example.

Electric fields have a long history to be used to manipulate droplet [62-67]. Link et al.

combined electrostatic charge on the droplets and electric fields on the devices and developed a module that created droplets one by one with a fine control, high purity and high throughput [68]. Kim et al. used an electric field to generate droplets in a hydrodynamic-flow-focusing geometry in microchannels. The droplet size could be adjusted by the strength of the electric field. Furthermore, the formed Taylor cone generated very fine droplets, usually less than 1μm in diameter [69]. Moreover, formation can also be controlled by adjusting the wettability of the two phases using electrowetting[70]. Recently, magnetic field becomes prevalent. Magnetic manipulation isn't affected by pH, ionic and surface charge concentration. Additionally, the magnetic field doesn't induce thermal effect, thus it attracts many researchers and some unique works have been carried out [71-73] to control droplet production and transport. The performance of most passive device can be modulated by using temperature fields using the thermocapillary effect. Baroud et al. used localized heating from a laser to block the motion of a water-oil interface, and then controlled droplet generation. They developed a theoretical model to explain the forces acting on a drop due to thermocapillary flow, and predicted a scaling law that favors miniaturization [74].

The second method to manipulate actively the formation process is realized by physically breaking up the fluid often called "choppers". Several pneumatic choppers have been developed based on the PDMS valve design. Bransky et al. integrated a piezeoelectric actuator that was able to specifically output a single droplet on demand from a reservoir [75].

1.2.2 Droplet (bubble) breakup

As the droplet (bubble) passes through the microchannel with complex geometry, the droplet (bubble) behavior will change. In microchannel, the shear force will deform the interface resulting in complexity of the flow field. Under certain condition, the breakup will occur which increases the operational capacity and functionality of a device. Several techniques have been developed to effectively break up a droplet into two or more droplets of predetermined size. There are two main kinds of micro geometry to conduct breakup process: T-(Y-) junction (Fig1.7a, b) and channel with obstacle (Fig1.7c). The previous studies demonstrate that there exists a critical elongation point beyond which the droplet past where breakup occurs [76-79].

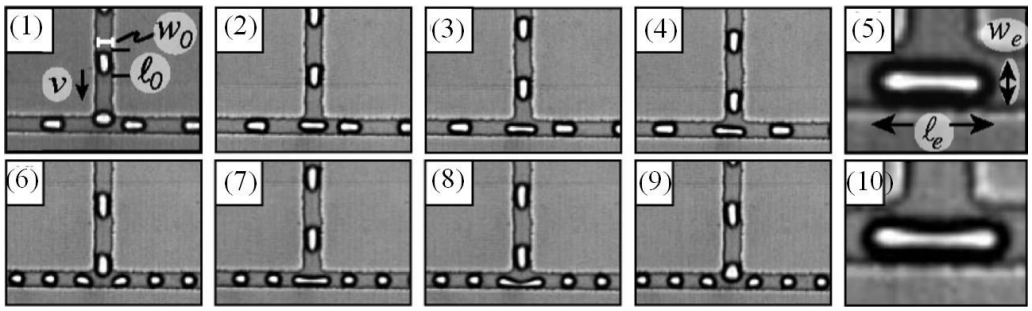

(a)

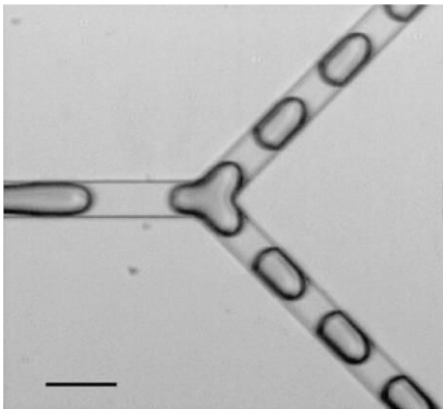

(b)

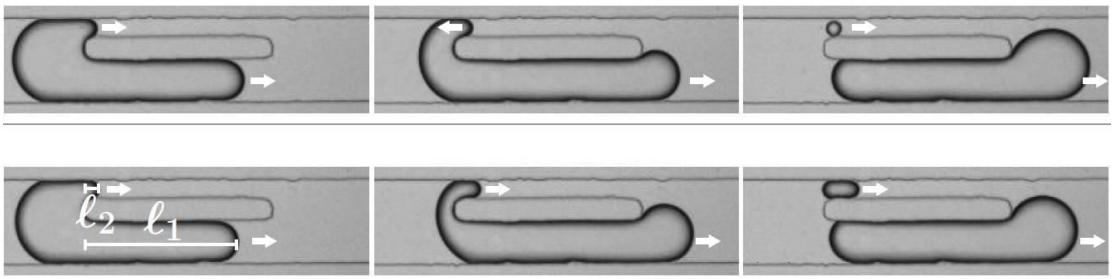

(c)

Fig. 1.7 droplet breakup processes in different microchannel (Link et al. (2004) (a)), (Yamada et al. (2008) (b)), (Salkin et al. (2012) (c))

T-junction

The most common geometry used to droplet (bubble) breakup is the T-junction bifurcation. Link et al. were the first researcher who systematically studied the breakup dynamics in T-junction [77]. Experimental results indicate droplet breakup is controlled by the flow rate of the continuous phase and the relative resistances of the two outlet channels. A model on base of Rayleigh-Plateau instability gives a critical capillary number for each droplet size predicting whether the droplet will breakup or

not as shown in Fig.1.8. Above this value the droplet will break up into two daughter droplet. By contrast, below this value the droplet will instead be transported down one of the outlet channels. It is obvious that the equation was derived for the critical capillary that was in excellent line with experimental results, $Ca = \alpha\varepsilon_0\left(1/\varepsilon_0^{2/3} - 1\right)^2$, where α is a fitting constant relating the viscosity ratio and geometry, and ε_0 is the extension of the droplet. The channel that the droplet chooses depends on which one has the highest flow rate when droplet reaches the junction.

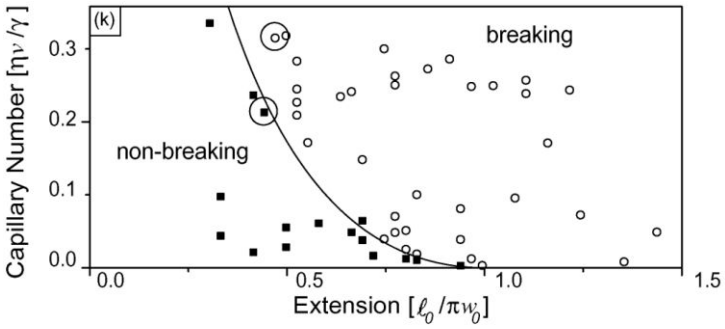

Fig. 1.8 The phase diagram for breaking (■) and non-breaking (○) droplets versus capillary number and the initial extension of the droplets (Link et al. (2004)).

Leshansky and Pismen proposed a different view from Link et al.; they argued that the Rayleigh-Plateau instability was probably not the cause of the breakup due to the confined nature of the flow [78]. They instead developed a 2D analytical model based on lubrication theory and the pressure accumulation due to the droplet blocking the outlet channels as it was being elongated. The elongating droplet blocks the flow to the outlet channels resulting in the augmenting pressure upstream. When this augmenting pressure overwhelmed the interface tension the droplet started to neck at the stagnation point until it pinched off into two separate daughter droplets. Their model still linked the capillary number and the droplet size: $l_0 / w_c = 1.3Ca^{-0.21}$; this relationship that was in good agreement with 2D numerical data and has a similar profile to the curve of Link et al..

Y-junction

Yamada et al. used a Y-junction to precisely control the droplet division at a bifurcation point in a microchannel [80]. By continuously introducing a new flow into the downstream of one of the branch channels, and by controlling the flow rates distributed into the two branch channels, the sizes of the daughter droplets in each

channel could be precisely adjusted. The authors regarded the microchannel network as a resistive circuit. Based on this, they developed a model which successfully predicted the ratio of the volumetric flow rates into the branch channels [80]. Salkin et al. investigated the break-up dynamics of deformable droplets and bubbles in microchannel with a linear micro-obstacle. The experiment results shed light on the role of the viscosity contrast between dispersed and continuous phases on the evolution of the critical breakup capillary number. When the viscosity of dispersed phase was superior compared with the viscosity of continuous phase, the experiments and modeling revealed the existence of an unexpected critical object size for which the critical capillary number for breakup is minimum. Salkin et al. derived a model that well described experiment data, provided diagrams distinguishing the four different hydrodynamic regimes, and demonstrated that the critical size originating from confinement solely depended on geometrical parameters of the obstacle [81]. The size of the two daughter droplets can be controlled by making the two outlet channels asymmetric, either through design of the channels, or through manipulation of the flow rate and pressure or through adding external field [77, 80, 82].

However, the bubble or droplet behavior is sometimes nonlinear at the junction owing to the hydrodynamic collective feedback or hydrodynamic memory—both the interplay of coherent resistance of the channels and the additional resistance arisen by the bubbles and droplets and any deviation from the desired setting can cause erratic droplet breakup [83-89]. Therefore, to precise control breakup process, it requires not only reaching the required critical capillary number for breakup but also controlling the influence of feedback in the outlet channels. Currently, there are two primary methods: (1) using constrictions at the breakup junction to locally increase the capillary number for breakup, and then expand the outlet channels to reduce the hydrodynamic resistance of the droplets or (2) by using external field to offset the hydrodynamic collective feedback.

1.2.3 Satellite Droplet formation

The presence of the surfactants in multiphase flow usually complicates the interface phenomena. Under micro scale, the capillary force, viscous and Marangoni effect are coupled tightly and can cause the appearance of some unique phenomena such as Rayleigh-Plateau instability and tip-streaming. The main problem caused by these

satellite droplets is that they increase the polydispersity of the emulsions. However, under certain condition, the satellite droplets may be useful. Indeed, due to the relative small size, the satellite droplets can allow to obtain emulsions with very small droplet size which may be less than one micrometer. Thus, more emphasis must be put on the mechanism of the satellites formation to control precisely the processes.

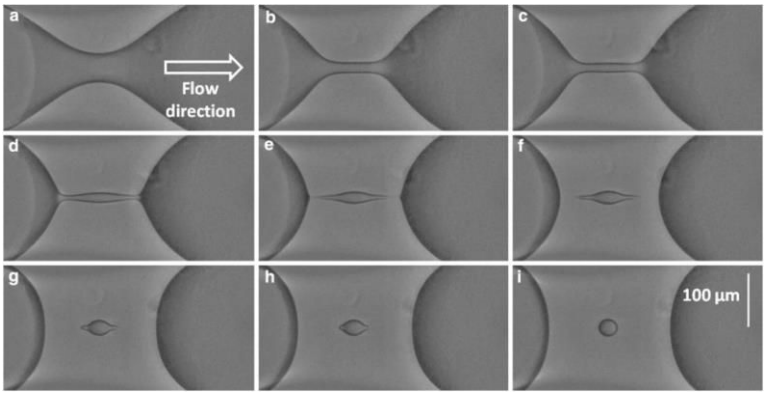

(a)

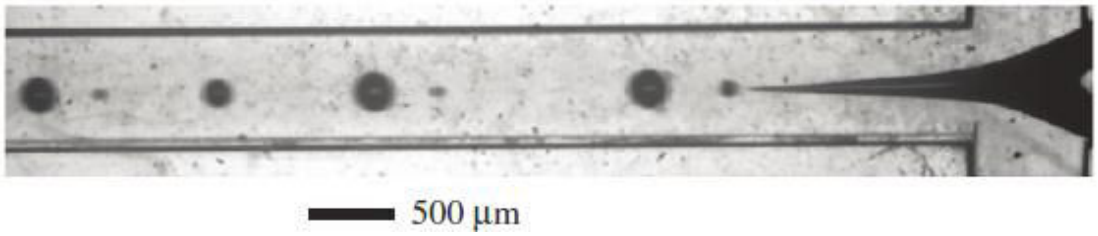

(b)

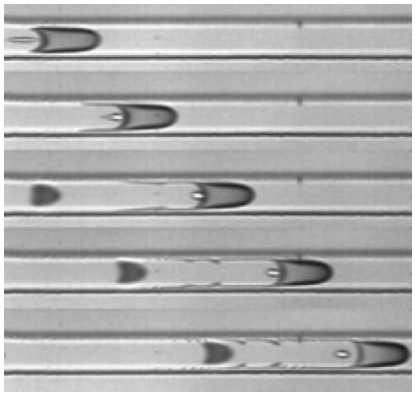

(c)

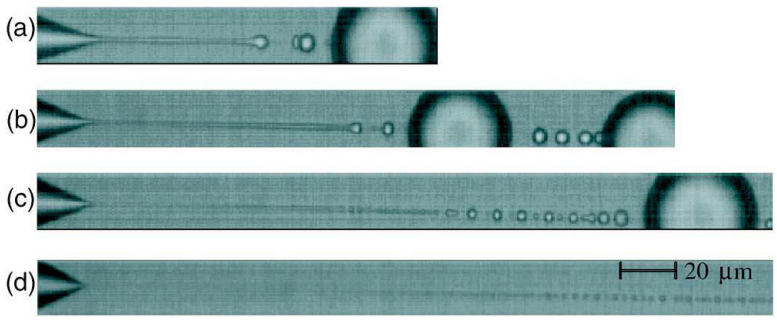

(d)

Fig. 1.9 Formation of satellite droplets in micro geometry (a) Carrier et al. (2013), (b) Fu et al. (2009), (c) Mulligan and Rothstein (2011) and (d) Anna and Mayer (2006)

Interface instability

When droplets are formed in flow focusing micro device, it is possible to observe the formation of satellite droplets at the behind of the primary droplet (Fig. 1.9a). Fu et al. observed the formation of satellite bubbles at very high liquid flow rate [90]. The diameter of the satellite bubble was inferior to a tenth of the microchannel's width and sometimes, the number of satellite bubbles could be more than one (Fig. 1.9b). The formation of satellite bubbles (or droplets) is due to complex competition between capillary force and viscous phase, causing interface instability, which leads to multiple breakup sequences of the cylindrical thread formed during the creation of primary bubble.

Carrier et al. studied the rupture of the neck of a main droplet which leaded to the formation of satellite droplets in a flow-focusing junction [91]. They reported that the size of the satellite droplet was a function of the capillary number of the continuous phase and there existed a critical capillary number of 0.01 dividing two different areas. Below this critical capillary number, the size of satellite droplet remained constant. Above this critical value, the size of the droplet increases almost linearly with the capillary number. Furthermore, the critical value also divided the rupture mode into two regimes: symmetrical for low capillary numbers and asymmetrical rupture of the neck of the droplet for higher capillary numbers. Recently, some devices were designed to control the fission or fusion of droplets, Tan et al. developed a technique to "sort" droplets according to size using an asymmetric bifurcation to separately recover satellite nano-droplets [92]. Tan and Lee also developed a technique by a passive filtering to eliminate such satellite droplets if they were not desired [93]. Mulligan and Rothstein reported the breakup of de-ionized water droplets in a hyperbolic contraction micro device [94]. The addition of surfactant to the system resulted in the formation of tails, which stemmed from the rear of the droplets and produced satellite droplets much smaller than the parent droplet as shown in Fig.1.9d. In the partially confined limit, where the flow was purely extensional, a single tail was formed at the center of the droplets trailing edge. At such condition, shear effects from the wall became important, the droplets were observed to take on a bullet-like

shape, and two tails formed at the trailing edge of the droplet. The generation of satellite droplets is linked to the capillary number, the surfactant used and confinement from the channel.

Tip-streaming

Anna and Mayer studied the mechanism of the surfactant-mediated tip-streaming to synthesize micrometer-scale and smaller droplets in flow-focusing geometry as show in Fig.1.9c [95]. In the typical system, surfactants are dissolved in the continuous phase and molecules can diffuse to the interface and adsorb onto or desorb from the interface. The flow of continuous phase stretches the interface and leads to gradients of surfactant concentration along the interface. Under conditions in which surfactants cannot desorb fast enough compared with their rate of compression along the interface due to the shear effect stemming from continuous phase, the tip of the droplet can become packed with surfactants. This leads to a sharp decrease in the interfacial tension and thus a highly curved tip. Eventually the highly curved tip is drawn into a thin thread, which subsequently breaks into tiny surfactant-laden droplets namely tip-stream.

1.2.4 Coalescence of droplet (bubble)

Coalescence is a daily phenomenon familiar to everybody and is related to many fields from biology to astronomy and also related to a variety of practical problems in industry. Up to now, numerous investigations have been devoted to droplet (bubble) coalescence inside or outside the realm of microfluidics [96-103]. The film drainage theory is one of the most widely accepted theories for coalescence. According to this theory, the coalescence process could be divided into three stages: (Ⅰ) the colliding of bubbles, besieging a small amount of continuous phase between two bubbles; (Ⅱ) the thinning of film, continuous phase draining out to a critical value; (Ⅲ) the rupture of film, the film collapsing and resulting in coalescence [104]. Currently, researcher put emphasis on two hotspots: (1) how to give rise to contact and collision, (2) what is the predominant force controlling the evolution of the liquid bridge.

For the first hotspot, it is the premise of coalescence. The collision between droplets is usually caused by their relative velocity. The relative motion may occur due to a

variety of mechanisms. In unbound flow, at least five sources can be distinguished in a turbulent flow: (1) motion induced by turbulent fluctuations in the surrounding continuous phase; (ii) motion induced by mean-velocity gradients in the flow; (iii) different bubble rise velocities induced by buoyancy or body forces; (iv) bubble capture in an eddy; (v) wake interactions or helical/zigzag trajectories[104]. In the realm of microfluidics, the state of flow maintains in laminar flow as mentioned before. Therefore the most common method is to induce collision by designing a special geometry.

The most direct approach is to utilize the convergence geometry. The droplets flow in the microchannel subjected to fierce confinement; the trajectory of the droplet can be predicted. Thus, as long as there is superposition between two trajectories, the droplets will collide. Wang et al. used a cross-shaped microchannel junction designed to realize head-on microdroplet coalescence without strict control of droplet synchronism as shown in Fig.1.10 [101]. They examined the flow characters of contacting microdroplets in confined microchannels and found a critical capillary number (Ca≈0.005) for the occurrence of coalescence.

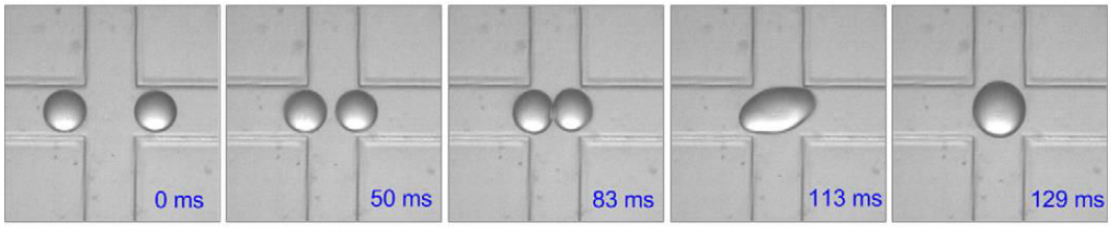

Fig. 1.10 Coalescence of droplets in convergence geometry (Wang et al. (2012))

Based on the same principle, researchers exploited T-convergence, Y-convergence and symmetric loop etc. micro-device to realize coalescence experiments [35, 105]. The second approach was to trigger relative velocity. The most prevalent design involved passing the droplets through an expansion region where the droplets slowed down, and the continuous phase is allowed to drain around the droplets. The droplets then exited through a sudden contraction that increases the flow rate and creates the disturbance required to break the film. Bremond et al. studied the coalescence process in a microfluidic antrum [106]. They utilized an expansion region to drain out the continuous phase between two droplets and then induced the collision. The coalescence occurred during the separation phase but not during the impact due to the

formation of two facing nipples in the contact area that hastened the connection of the interfaces prior to fusion.

Niu et al. used a series of pillars in the expansion region to trap the incoming droplet and hold it in place until the droplet behind merged [107]. Their approach involved exploiting the difference in hydrodynamic resistance of the continuous phase and the surface tension of the dispersed phase through the use of pillars contained within a microfluidic channel. Initial experiments demonstrate that such a merging element could controllably adjust the distance between adjacent droplets. The experiments indicated that such a merging process was independent of the inter-droplet separation but rather dependent on the droplet size.

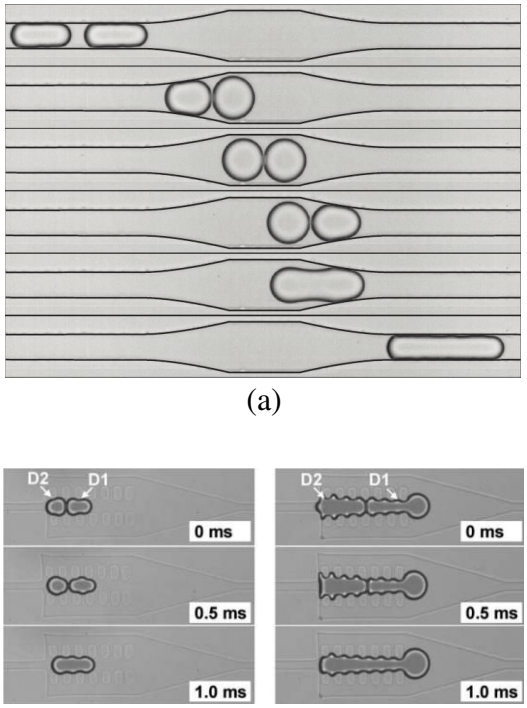

(a)

(b)

Fig. 1.11 (a) Coalescence of droplets in convergence geometry (Bremond et al. (2008))
(b) Pillar-induced droplet merging in microfluidic circuits (Niu et al. (2008))

After effective contact, a microscopic connecting liquid bridge between two droplet forms and rapidly grows as the two drops merge into one (Fig. 1.12 (a)). The dynamics of the expanding neck attract a lot of researcher, and several models were developed to predict the expanding velocity of the neck [41, 97-99].

Paulsen et al. studied the merging of gas bubbles and liquid drops in an external fluid

[99]. The data indicated that the flows occur over much larger length scales in the outer fluid than inside the drops themselves. They assemble these results in a phase diagram for bubble and two-fluid coalescence, as shown in Fig. 1.12b. Coalescence begins (at asymptotically early times) in the ILV regime where the outer fluid is unimportant, no matter how large its density or viscosity is. In making the axes non-dimensional, an important dimensionless number emerges to determine from where the inertial stress (given by the inner or outer fluid) is equal to the viscous stress in the outer fluid.

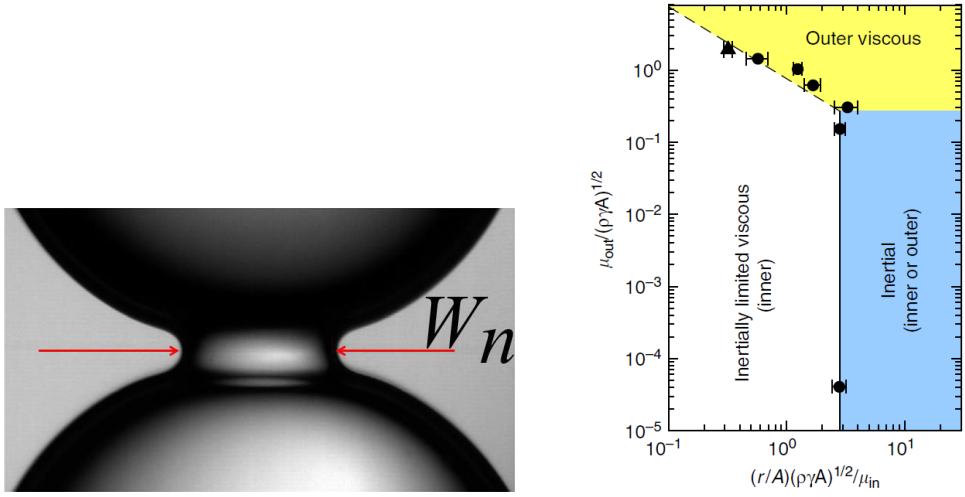

(a) (b)

Fig. 1.12 (a) Salt water drops coalesce in silicone oil (b) operation diagram (Paulsen et al. (2014))

The advantage of passive techniques to induce coalescence is that they require no interaction and are easy to implement; their disadvantage is that they lack degree of freedom to control over the coalescence process and each design has a limited operational range. To improve the viability and control of the droplet process a number of active methods have been developed utilizing the external field.

The most common active method to merge droplets is through electro-fusion using external fields. A non-uniform electric field can be used to control droplet motion by dielectrophoresis (DEP) due to the difference dielectric properties between the continuous phase and dispersed phase. Two droplets in the electric field align their dipoles and are attracted to each other by a Columbic force. The strength of the force is proportional to the square of the applied electric field. The applied electric field and the frequency govern the electrocoalescence process.

There exist both an upper and lower limits for the electric field. Ristenpart et al. reported the existence of a critical field strength above which the droplets approach each other quickly but the oppositely charged droplets do not coalesce [108]. They observed that appropriately positioned and oppositely charged droplets migrate towards one another in an applied electric field; but whereas the droplets coalesce as expected at relative low field strengths, they are repelled from one another after contact at higher field strengths. At the lower limit, the instability is not strong enough to break the thin film between the droplets. Priest et al. used two closely spaced electrodes to induce successfully coalescence of tightly packed droplets in a microchannel [109].

Droplet fusion can also be controlled using thermocapillary effects. A laser was used to heat the interfaces of two adjacent droplets until they fused [110]. The local irradiation will lead to a temperature gradient which induced the Marangoni effect due to the temperature dependent surface tension and viscosity of the fluids. This will bring the disturbance to the interface contributing to the coalescence.

To manipulate and control droplets (bubble) in microchannels requires an understanding of the underlying physics and various forces involved. Methods for generating, transporting, splitting and combining were reviewed. Throughout the review an emphasis was put on identifying methods and conditions where droplets can be controlled effectively resulting in stable device operation.

1.3 Outline

This thesis comprises a collection of papers. Chapters 3 - 6 are therefore self-contained. In chapter 2, we point the reader to literature on microfabrication, high-speed camera and image processing, since this information was not, or only briefly, included in chapters 3 - 6. Our work on the formation of ferrodroplet is described in chapters 3. In brief, we report the influence of the external magnetic field on formation process in flow-focusing geometry in chapter 3. In chapter 4, we show the ferrodroplet breakup process under different magnetic fields and the influence of hydrodynamic memory on the breakup of bubbles. In chapter 5, firstly, we show that the formation of satellite droplet during the thinning thread of primary droplet in flow-focusing geometry. Subsequently, we demonstrate the tip stream which produces

countless satellite droplets is generated in the tail of primary droplet. In chapter 6, we present the work on bubble coalescence in a T-junction as well as the coalescence of ferrodroplets. We analyzed the dynamics of the expanding liquid bridge.

Chapter 2 Experimental

2.1 Fabrication Methods and Experimental Techniques

The devices used in experiments contain channels with sub-millimeter dimensions and usually are made by transparent materials such as silicon wafer, glass and organic polymer, etc. thereby enabling researcher to monitor the flows in real time. The images of the micro-channel flow are magnified by a microscope then recorded by a high-speed camera; subsequently, analyzed in post-processing by self-written programs.

This chapter is to offer the reader the information on microfabrication, high-speed camera and image processing, since this information is not, or only briefly, included in next chapters. There are 3 topics covered including device fabrication, experimental setup and image processing.

2.2 Micro machining and Wettability of PMMA

2.2.1 Precise milling

The devices used in chapters 3 to 6 contain channels with sub-millimeter dimensions (width =height = 400 μm). We fabricated those devices by milling the channels in a flat plate of poly (methyl methacrylate) (PMMA). PMMA is a rigid thermoplastic that is optically transparent. The microchannel was fabricated by milling cutter with high precision in one slide of PMMA. We sealed our PMMA channels to a cover slide of the same material by bolt.

2.2.2 Wettability of PMMA

In multiphase microfluidics, the wetting properties of fluids and channel walls dominate the flow pattern. In our work, we were interested in a well-defined system with the liquid fully wetting the channel walls. This was achieved by choosing the proper combination of materials and fluids. PMMA is the materials we used to fabricate our devices. The polymer is low-energy materials with a surface free energy

of $\sigma_s = 41$ mN/m. Generally, liquids cannot fully wet low-energy surfaces. For instance, water partially wets the surface of PMMA, with an equilibrium contact angle of $\theta_c = 72°$. With a contact angle less than 90° PMMA is regarded as a hydrophilic material.

For PMMA, the critical surface tension is $\sigma_c = 40$ mN/m. A liquid with surface tension inferior to 40 mN/m will fully wets a surface and partially wets a surface when the surface tension is superior to 40 mN/m. Sometimes the surfactants were used to change the surface tension, thereby producing direct emulsion (oil phase in aqueous phase) or invers emulsion (aqueous phase in oil phase) in the same micro-device.

2.2.3 PMMA Microchannels

Four microfluidic devices were used in this thesis. Fig. 2.1 shows the layout of the devices. All these four microchannels contain a flow-focusing geometry to form droplet (bubble). The continuous phase was guided into two equal lateral branches with the same flow rate $Q_c/2$, the dispersed phase was introduced from the main channel at a flow rate of Q_d. These three flow streams focused at the intersection downstream to generate discrete droplet or bubble. Then according to different research objectives, the new formed droplet or bubble will flows downstream passing some given geometries, such as symmetric loop (Fig2.1 b,c), snakelike microchannel (Fig2.1c), straight channel (Fig2.1d) etc. In a symmetric loop (Fig2.1 b,c), the microchannel divides into two symmetric parts at the first T-junction, and then the two channels reconvert to a single channel again at the second T-junction. By this geometry, the breakup of droplets (bubbles) could be studied at the T-junction divergence; while at the T-junction convergence, the responses of droplets (bubbles) collision could be studied. The snakelike microchannel (Fig2.1c) is mainly utilized to added local resistance which could damp the changes in pressure caused by droplets (bubbles) flowing through the loop to ensure that the process of bubble generating would not be interrupted. The straight channel (Fig2.1d) is used to studied the evolution of the morphological shape of the droplets flowing in the microchannel.

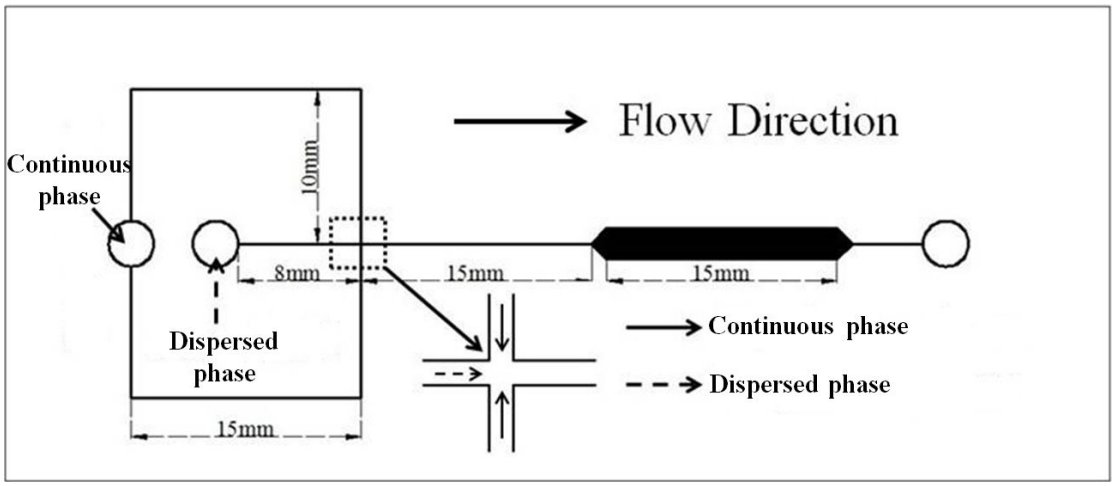
Flow Direction
Continuous phase
10mm
8mm
15mm
15mm
Dispersed phase
15mm
Continuous phase
Dispersed phase

(a)

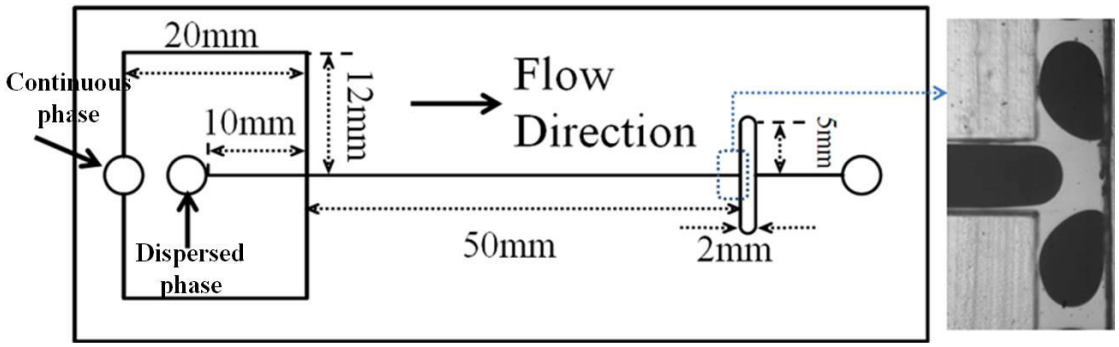
20mm
Continuous phase
12mm
Flow Direction
10mm
5mm
Dispersed phase
50mm
2mm

(b)

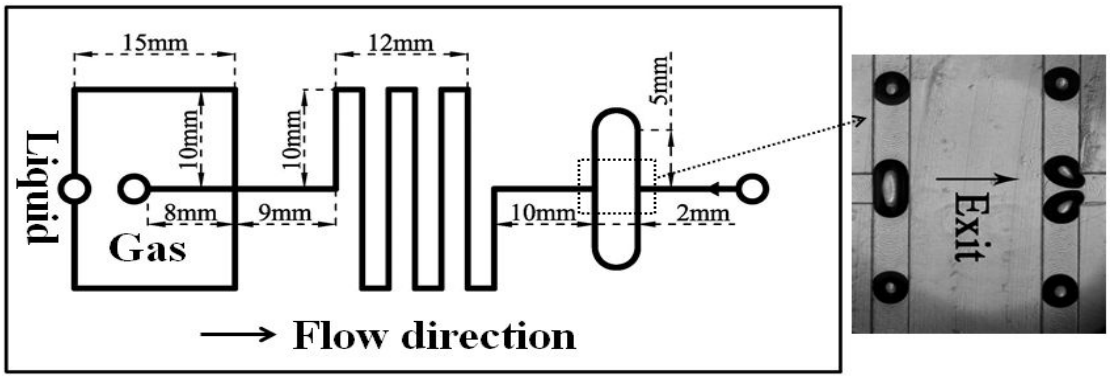
15mm
12mm
5mm
10mm
10mm
Liquid
8mm
9mm
10mm
2mm
Gas
Flow direction
Exit

(c)

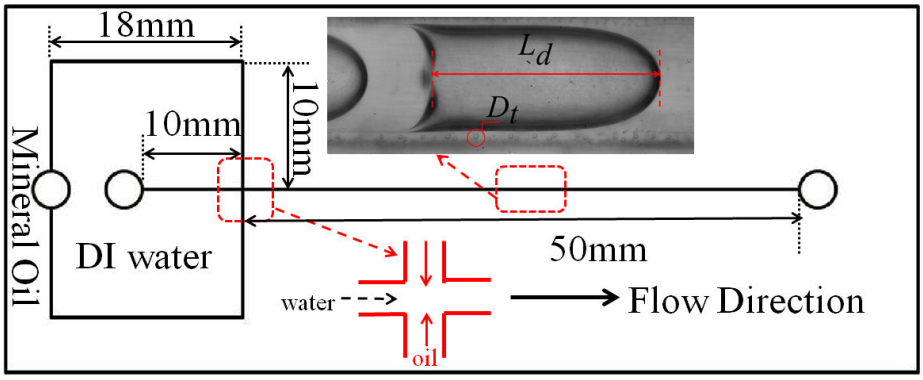

(d)

Fig 2.1. (a)-(d) Schematic diagrams of the microfluidic devices. (a) used in chapter3and 5, (b) used in chapter4 and5, (c) used in chapter4 and6, (d) used in chapter5.

2.3 Experimental Setup

2.3.1 Experimental setup for microsystems

The experimental setup is presented in Fig.2.2. Droplet devices were visualized using an inverted microscope system (Leica, Germany). The inlets are connected to different equipment depending on the experimental contents. Gas was fed by a N_2 cylinder and the flow rate was controlled by a high precision micro-metering valve (KOFLOC, Japan). Liquid was delivered from syringes (5 mL, 10 mL and 60 mL, Hamilton, Germany) by a syringe pump (Harvard Apparatus, PHD 22/2000, USA). The magnetic flux densities and the directions of magnetic field could be easily adjusted by changing the location of the magnets and the separation distance between the ferrofluid and magnets. Illumination was provided by a 100 W halogen lamp for bright field applications and phase contrast.

Three high-speed cameras were used in our experiments, depending on the speed of the phenomena observed. The speed camera CamRecord 600 (Optronis, Germany) and Redlake Motion (Pro Y-5, USA) were mainly used to record the relative slow phenomena in transparent micro-geometries. The maximum camera resolution of these two cameras is of 1280 × 1048 pixels. The shutter speed of the camera in this work varied between 1/1000 and 1/10000 s according to the lighting conditions (microscope objective used) and the speed of the observed phenomena. The image

capture speed is between 50 fps and 2000 fps.

The evolution of the final pinch-off of the neck filament and the coalescence process are faster, a camera with higher frame speed was used. The minimum shutter interval of the Phantom Speed Sense V711 camera (Vision Research, USA) is 1μs. Its maximum resolution is 1280 × 800 pixels and up to 7500 fps at full resolution. With our lighting conditions, it is possible to achieve a shutter speed 1/250000 s. The image pickup speed is mounted to the maximum 50,000 fps in our experiments.

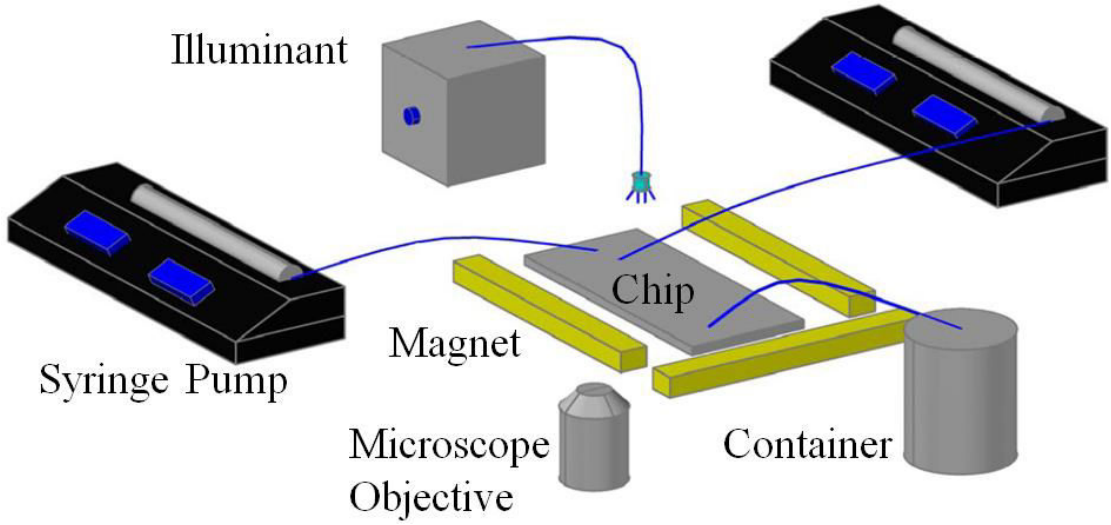

Fig. 2.2 Scheme of the experimental setup for microsystems

2.3.2 Experimental for ferrodroplet coalescence in the ambient air

The experimental setup is shown in Fig .2.3. A vertical stainless steel needle（external diameter = 0.98mm） plated with Teflon was connected to an independent syringe (5 mL, Hamilton, Germany) driven by syringe pumps (Harvard Apparatus, USA) to form ferrofluid droplets. The tip of the needle was placed above the center of a neodymium iron boron (NdFeB) round magnet (with diameter of 60 mm, Supermagnete, France). A liquid bath of square section (7×7 mm) with a depth of 5 mm filled up with the same ferrofluid was placed between the needle and the magnet. The center of magnet, the tip of needle and the ferrofluid cusp were coaxial by adjusting the platforms. The distance between needle tip and ferrofluid cusp as show in Fig.2.3 was constant D = 1.80 ± 0.04 mm and the flow rate set as a constant Q_c = 1.5 μL/min. In our

experiments, oil-based ferrofluid (Supermagnete, France) was used with an average diameter of magnetic particles 10 nm, the magneto-viscous effect could be negligible. The whole processes were recorded at 30 008 frames per second with the Phantom V711 camera.

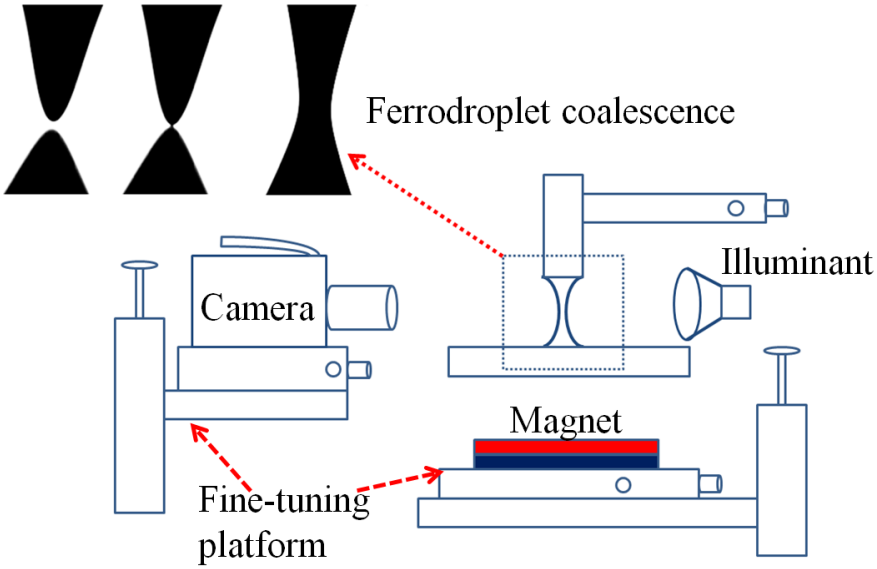

Fig. 2.3. Scheme of the experimental setup.

2.4 Numerical methods

In this study, FLUENT 6.2.26 (2-D) CFD software was used to simulate the flow fields in the liquid phase at the microfluidic T-junction convergence. The volume of fluid (VOF) method based on the piecewise linear interface representation (PLIC-VOF) was used to capture and track the precise location of the interface of bubbles. The two fluids can avoid interpenetrating by using VOF method. For each qth fluid phase in the system, it has a corresponding variable volume fraction (Ωq). For each computational control volume, the sum of all volume fractions must equal to unity. All variables and properties (such as the density ρ, and the dynamic viscosity μ) in every computational control volume are volume-averaged values. The governing equation of the VOF includes continuity Eq. (6-1) and the momentum Eq. (6-2). For gas-liquid two phase flow, the VOF method accomplishes interface tracking by solving an additional continuity-like Eq. (6-3) for the volume fraction of the gas phase, which yields the value of Ω_G. The volume fraction of liquid Ω_L is equal to (1 - Ω_G). The surface tension force F was modeled using the continuum surface force (CSF) model proposed by Brackbill et al., as shown in Eq. 6-4. Here σ denotes the coefficient of surface tension, κ is the radius of curvature, δ(r) denotes the Dirac delta

function and n denotes the unit normal vector on the interface. With this model, the surface tension force results in a source term in the momentum equation.

$$\frac{\partial \rho}{\partial t} + \nabla \cdot \left(\rho \vec{v} \right) = 0 \tag{2-1}$$

$$\frac{\partial (\rho \vec{v})}{\partial t} + \nabla \cdot \left(\rho \vec{v} \vec{v} \right) = -\nabla \rho + \nabla \cdot \left[\mu \left(\nabla \vec{v} + \nabla \vec{v}^{T} \right) \right] + \vec{F} \tag{2-2}$$

$$\frac{\partial \Omega_G}{\partial t} + \vec{v} \cdot \nabla \Omega_G = 0 \tag{2-3}$$

$$\vec{F} = \sigma \kappa \delta (r - r_{int}) n \qquad \kappa = \nabla \cdot n \tag{2-4}$$

A pressure based solver was used along with the implicit body force formulation. Air was designated as the primary phase and water as the secondary one. Wall adhesion was turned on and the contact angle (θ = 160°) could be set and a constant surface tension value (σ = 72 dyn/cm) was set. The PISO (pressure-implicit with splitting of operators) scheme was used for pressure-velocity coupling, and the second-order up-wind differencing scheme was used for the momentum equation. Geo-Reconstruct scheme was used for volume fraction. For discretization, the PRESTO! (Pressure staggering options) scheme was used for pressure interpolation. For the inlets, the velocity inlet boundary condition was used, while pressure outlet boundary condition was used for the outlet. The time step was set as 1×10^{-7}s. In our simulations, the grids at the left and right sides of symmetry axis are refined and the minimum interval size is 1×10^{-7} m with 20 rows in each side. The mesh dependence study was investigated to determine the interval size of volume elements. When changing the interval size from 1×10^{-7} m to 0.5×10^{-7} m, the variations of the location where coalescences occur and the bubble interface shape were negligible. Therefore, the mesh with minimum interval size 1×10^{-7} m was adequate and then exported to the FLUENT solver.

2.5 Image analysis

The images obtained were analyzed with different programs Matlab (R2006b version 7.3.0.267). In particular, a program that we performed was used to determine the droplet size based on the number of pixels occupied and with the assumption of cylindrical symmetry for the main droplets:

In a first step, a mean image is created from a hundred images of the flow. It will be used to eliminate noises which remain motionless on the image to be analyzed (walls of channel, stains and defects on the channel exterior etc.).

Secondly, the image to be analyzed is then ‘‘divided’’ into pixel per pixel by the mean image. The new gray scaled divided image is transformed in a black and white image by applying a threshold chosen by the user. If necessary, it is possible to add elements to help the analysis, such as boundaries of the wall when the edges of the droplet are not clearly defined where two black lines were added which could be done using a sub-function according to Bresenham's algorithm for drawing a segment between two pixels defined by the user. The final image is obtained by “filling” the droplets edges. The volume is then calculated by counting the pixels occupied by the droplet. The droplet is “cut” into one pixel large slices and considering each slice as a disc of the same thickness. A calibration is then applied to evaluate the volume in SI units rather than cubic pixels.

The objective of the microscope has been chosen so that satellite droplets have at least a diameter around 15 pixels. To ensure the validity of the measurements, droplet formation was determined with two different objectives, and the difference was found negligible. Each droplet measurement has been repeated at least 10 times on different images. The standard deviation of satellite droplets is about 23 %. The size of the droplet neck is measured in function of time. The Matlab algorithm is based on the same principles as the droplet size determination. Images are transformed in black and white with the same method as above-mentioned. The edges of the forming droplet are then detected (transition from white to black pixel) for the length of the droplet. The minimum value between the two edges is considered as the neck width at the instant the image was taken.

2.6 Physical properties of materials used in the experiments

The surface tension σ was measured using a tensiometer, by the pendant drop technique on a Tracker apparatus (Dataphysics, Gemany). The viscosity of the fluids μ

was measured by capillary viscosimetry (TA instrument, NewCastle DE, USA). The density of the liquid phase ρ was measured using a vibrating tuber density meter (Anton Paar DMA-4500-M, Austria). The surface tensions of ferrofluids in different ambient were measured in our laboratory, while other physical properties of ferrofluids are observed from the fabricators (oil-based ferrofluid, Supermagnete, France; water-based ferrofluid, Ferrotech, Germany). The particles volume concentration of water-based ferrofluid was 1.8% and the initial susceptibility χ = 0.39. In our experiments, the two kinds ferrofluid were used with an average diameter of magnetic particles 10 nm, the magneto-viscous effect could be negligible. In addition, the surfactant Sodium dodecyl sulfate (SDS, Sigma-Aldrich, Germany) and Sorbitanlauric acid ester (Span20, Sigma-Aldrich, Germany) were added in the continuous phase, respectively to stabilize the flow pattern and prevent the coalescence. The various properties of the experimental systems were gathered in following Tables.

Table 1 Physical properties of the materials used in the experiments

	Density ρ (kg/m^{-3})	Viscosity μ (mPa.s)
Aqueous phase		
Deionized water	999.00	1.01
5% glycerol / water	1010.71	1.16
10% glycerol / water	1023.10	1.41
15% glycerol / water	1035.33	1.54
20% glycerol / water	1052.29	1.83
25% glycerol / water	1060.07	2.10
30% glycerol / water	1078.87	2.51
40% glycerol / water	1107.75	3.84
50% glycerol / water	1131.62	6.14
62% glycerol / water	1150.42	9.76
Ferrofluid (EMG807)	1100.00	2.00
Oil phase		
Mineral oil	838.00	35.21
Oil-based ferrofluid	1200.00	11.25

Gaseous phase		
Nitrogen	1.25	1.78×10^{-2}
Air	1.18	1.85×10^{-2}

Table 2 Surface tension between two phases

Continuous phase	Dispersed phase	Surface tension σ (mN m^{-1})
Liquid -gas		
Deionized water	air	73.19
5% glycerol / water	air	72.55
10% glycerol / water	air	72.08
15% glycerol / water	air	71.34
20% glycerol / water	air	71.08
25% glycerol / water	air	70.98
30% glycerol / water	air	70.86
40% glycerol / water	air	69.55
50% glycerol / water	air	68.32
0.24% SDS/deionized water	nitrogen	34.32
gas-Liquid		
air	oil-based ferrofluid	23.65
Liquid –Liquid		
4% Span20/ mineral oil	water-based ferrofluid	1.55
2% Span20/ mineral oil	deionized water	3.15

Chapter 3 Water-based ferrofluid droplet formation in a microfluidic flow-focusing device

Droplet formation is an indispensable part of microfluidics. Remarkable number of articles shed light on this process. Combining the magnetic field with conventional passive methods could improve the controllability of microfluidics, simultaneously, enrich the knowledge in micro two-phase flows. This chapter aims at utilizing external magnetic field to precisely control the droplet generation process. We studied the expanding and breakup dynamics of the thread of a controllable dispersed phase under different flow rates in a microfluidic flow-focusing device. The whole formation processes of ferrofluid droplets under no magnetic field (NM), radial magnetic field (RM) and axial magnetic field (AM) were investigated and compared. It was found that the volume of ferrofluid droplets can be actively controlled by the applied magnetic field. Both the radial magnetic field and axial magnetic field affect mainly the expanding and breakup process of the thread, respectively. The influence of the flow rates, magnetic flux density and magnetic field direction on the formation and breakup processes was extensively studied. The variation of the minimum width of the ferrofluid thread with the remaining time could be scaled with a power law.

3.1 Introduction

Recently, magnetic particle and microfluidics were combined as micro-magnetofluidics to gain new insight into various applications [13, 111]. Magnetofluid is a kind of suspension of magnetic particles, and the investigation devoted to magnetofluid can be classified into four categories: ferrohydrodynamics, magneto-hydrodynamics, magnetophresis and magnetorheology [111]. Taking advantage of the magnetofluid, it is possible to realize pumping [112], switching and adjusting flow rate [113], mixing [114], transporting [115, 116], sorting [117], detecting [118] and dynamical wetting [119]. Among numerous types of magnetofluid, ferrofluid possesses magnanimous attractive characteristics. The size of magnetic particles is of nanometer order. Without external magnetic field, the magnetic anisotropy energy (proportional to particle volume) is then smaller than thermal energy at room

temperature [111]. This implies that there is no remnant magnetization after removal of the magnetic field. Therefore, we can easily turn on or switch off the influence of the magnetic field. Furthermore, the ferrofluid displays high efficiency for heat transfer [120]. Combining the characteristics of ferrofluid and microfluidic device, micro-ferrofluidic droplets can be formed to find wide applications in biology, engineering, medical treatment and chemical analysis [120-124].

In particular, a ferrofluid droplet in presence of magnetic field undergoes magnetic force and this provides an interesting opportunity to actively manipulate the droplet such as the volume control or transport [120, 123, 125]. Compared to other active methods, magnetic manipulation isn't affected by pH, ionic and surface charge concentration. Moreover, the magnetic field doesn't induce thermal effect [111].

Some works were devoted to the formation mechanism of the ferrofluidic droplet in the microfluidic T-junction and flow-focusing devices. For ferrofluid droplet formed in a microfluidic T-junction under the magnetic field owing to magnet, the relative size V_m/V_n (here V denotes droplet volume and subscripts m and n means 'with' and 'without' magnetic field) depends on the formation pattern, in particular the location of magnet. When the magnet is placed upstream of the T-junction, the magnetic force favours the breakup process causing the relative size $V_m/V_n < 1$ [120, 123]. When the homogeneous magnetic field is applied in the axial direction, the droplet formation in a flow-focusing device is facilitated with $V_m/V_n > 1$ [11]. The increase of both the initial susceptibility of the ferrofluid χ and the magnetic flux density B stimulates this effect. During the experiments, lines of nanopaticle could be observed. These lines and internal secondary flows delay then the thinning process of the neck of the disersed phase [121, 122]. Some authors reported the role of applied magnetical fields [120, 122, 123]. However, the influence of physical properties of fluids and flow rates on the droplet size is still missing to our best knowledge. In particular, there is very few information on the expanding and breakup dynamics of the thread of dispersed phase under different magnetic fields in a microfluidic flow-focusing device.

The present work aims at investigating experimentally the formation of ferrofluid droplets in a microfluidic flow-focusing device under various configurations: radial magnetic field (RM), axial magnetic field (AM) and without magnetic field (NM).

The droplet expanding mechanism and breakup dynamics were explored under different flow rates and magnetic flux density.

3.2 Results and discussion

3.2.1 Droplet formation in the dripping regime under three configurations of magnetic fields

Three typical formation scenarios of water-based ferrofluid (EMG 807) droplets are illustrated in Fig. 3.1: under no magnetic field (NM), under radial magnetic field (RM) and under axial magnetic field (AM).

(1) Type NM: firstly, the dispersed thread expands in both the axial and radial directions in the intersection region of the main inlet channel (left) and two side channels (top and bottom). The tip of the thread is reminiscent of a half dome (Fig. 3.1 NM a & b); secondly, the expanding thread reaches the edges of the outlet channel and continues to move downstream with the outlet channel partially blocked. During this time the continuous phase thins the dispersed thread in the radial direction and elongates it in the axial direction until the presence of the neck (Fig. 3.1 NM c); thirdly, the neck forms and thins progressively. In this process, the film between the thread tip and the wall of outlet channel becomes very thin (Fig. 3.1 NM d & e); finally, the neck pinches off until to form a new droplet. Besides the primary droplet, the neck rupture induces usually satellite droplets (Fig. 3.1 NM f). The formation of ferrofluid droplets under NM condition is similar to the classical droplet formation mechanism reported previously [90, 126]. This implies that, without a magnetic field, the ferrofluid behaves similarly as homogeneous fluid.

(2) Type RM: at the beginning, the dispersed thread also expands in the axial and radial directions in the intersection region. But under RM the thread is obviously stretched in the radial direction (Fig. 3.1 RM a & b); then, as the thread reaches the edges of the outlet channel and plugs into the channel, it seems that the thread blocks the entire channel (Fig. 3.1 RM c); thirdly, during the whole thinning process, the outlet channel is always blocked by the thread tip. The curvature of the tip is much smaller compared to NM case (Fig.3.1 RM d & e); lastly, the final pinch-off is similar

to the NM scenario (Fig. 3.1 RM f).

(3) Type AM: at the beginning, the dispersed thread expands in the intersection region and the axial expanding is much more tenuous than the NM case. The curvature of the thread tip is larger than NM and RM (Fig.3.1 AM a & b); after then, the film between the thread tip and the wall of outlet channel is noticeable (Fig.3.1 AM c) when the thread propagates into the outlet channel; thirdly, during the thinning process of the neck, the film is always visible. The curvature of the dispersed neck in the three scenarios varies according to the following order: AM $<$ NM $<$ RM (Fig. 3.1 AM d & e); finally, the droplet detaches with the neck broken into several satellite droplets (Fig. 3.1 AM f). Comparing the formation mechanism of ferrofluid droplets under AM, NM and RM, the ratio of length to diameter can be classed in the following order: RM $<$ NM $<$ AM.

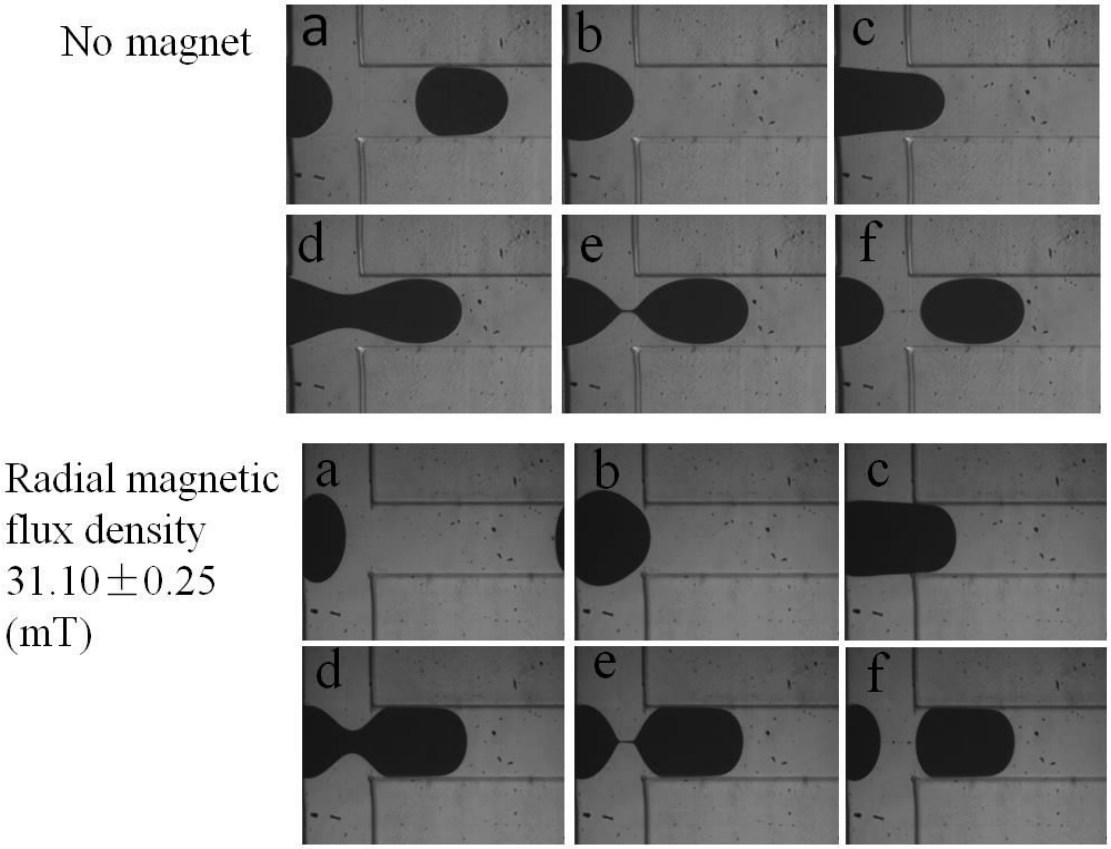

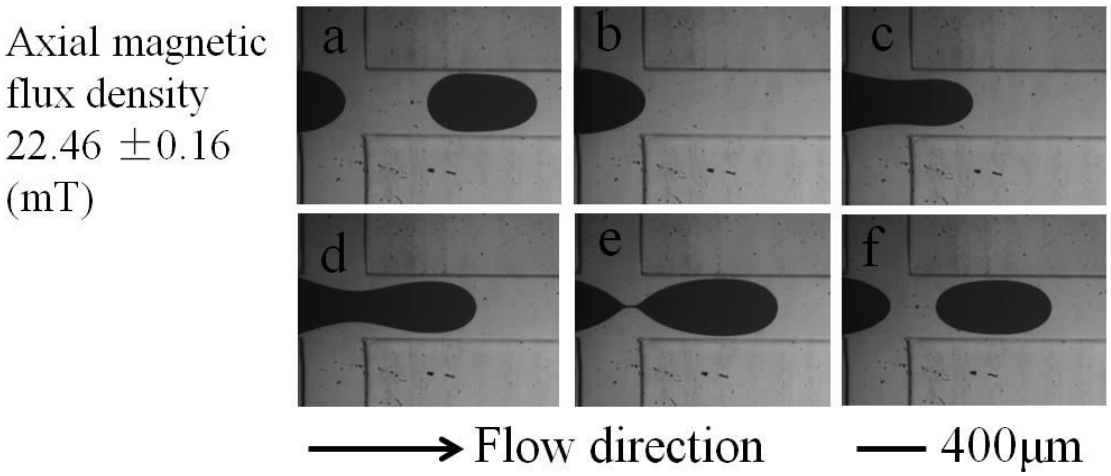

Fig. 3.1. Formation sequence of ferrofluid droplets in the dripping regime.

3.2.2 Volume of ferrofluid droplet and the formation mechanism

Fig. 3.2 shows the normalized volume V_m/V_n (here V denotes droplet volume and subscripts m and n means 'with' and 'without' magnetic field) of formed ferrofluid droplets as a function of the flow rate of the continuous phase Q_c under four different configurations of the magnetic field. In general, in the presence of the radial and axial magnetic fields, the sizes of the droplets are larger than those formed without magnetic field and the normalized volume of ferrofluid droplets increases with the increase of the magnetic flux density. At a fixed flow rate ratio ($Q_c/Q_d = 8$), the normalized volume of ferrofluid droplets and the difference between four magnetic fields decrease with the increase of Q_c (Fig. 3.2). Obviously, we should focus on the droplet formation and breakup mechanism to better understand these phenomena.

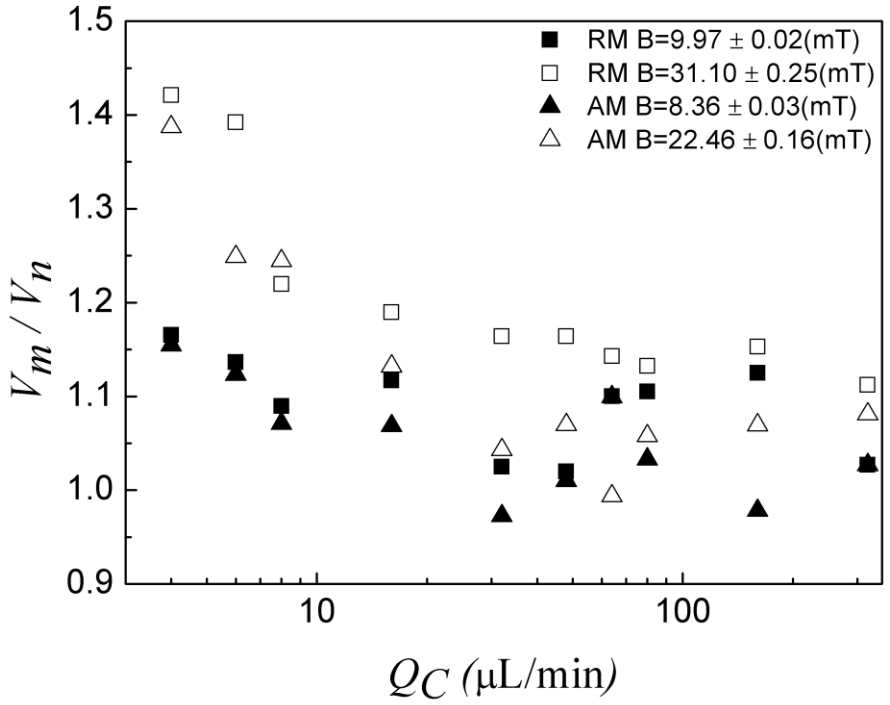

Fig. 3.2. Size of ferrofluid droplet as a function of the flow rates of continuous phase under different magnetic fields. $Q_c/Q_d = 8$.

In this work, the whole formation process of ferrofluid droplets is divided into two parts. The first one is the expanding of droplets in the intersection region and the second the thinning of the dispersed neck until the final pinch-off. According to Fig 3.2, the roles played by the magnetic fields in the droplet formation are different according to the operating conditions: significant influence of the magnetic field in lower flow rates and relative small effect in higher flow rates. In our experiments, the Reynolds number of the continuous phase ($Re_c = (\rho_c u_c w_c)/\mu_c = 0.5$) could be chosen to distinguish high and low flow rate regions.

As shown in Fig. 3.3a, b and c, W_l, W_s and L_d denote respectively the maximum width of the expanding tip, the minimum width of the thinning neck and the length of the dispersed thread in the outlet channel. An example of the temporal evolution of the maximum width of the thread tip W_l in low flow rate region ($Re_c = 0.0793$) is illustrated in Fig.3. 4a. At the initial expanding process, when there is no magnetic field or the radial direction magnetic field, W_l is larger than the channel width W_c and W_l increases with the increase of the radial magnetic flux density. This is mainly

caused by the magnetic force which stretches the thread in radial direction. We use the magnetic Bond number to represent the ratio between magnetic force and surface tension $Bo = \mu_0 \chi W_c H^2/\sigma$ [111]. Here $\mu_0 = 4\pi \times 10^{-7}$ N/A^2 is the permeability of the free space, H is the magnetic field strength. For B equal to 31.10 and 17.10 mT ($B = \mu_0 H$), Bo ranges from 80 to 24. This implies the magnetic force is much higher than the surface tension, W_l is logically much larger than W_c. Due to the stretch, the curvature of the tip becomes smaller, then leads to a smaller capillary force. This results in a much easier expanding process, so the difference between W_l and W_c increases along with the expanding stage. While the magnetic field is added in the axial direction, due to the thread tip detaches from the main channel walls, W_l is smaller than W_c in the initial expanding process as shown in Fig 3.3c. This maximum width of the thread tip W_l is always observed at the exit of the main channel. When the thread tip reaches the edge, W_l has the maximum before starting the thinning process.

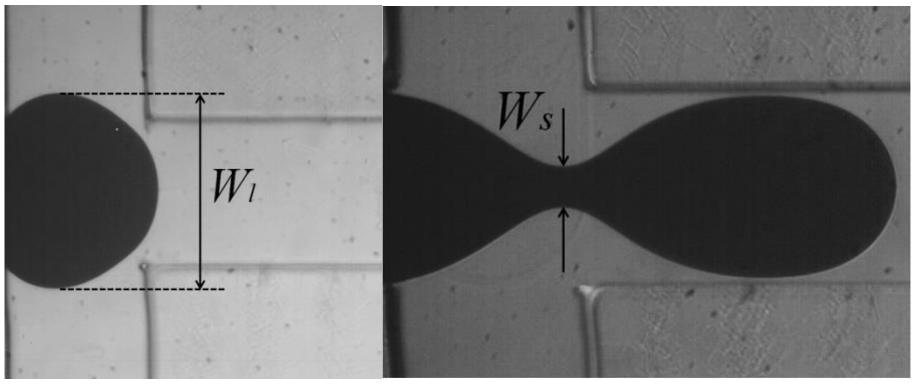

(a) (b)

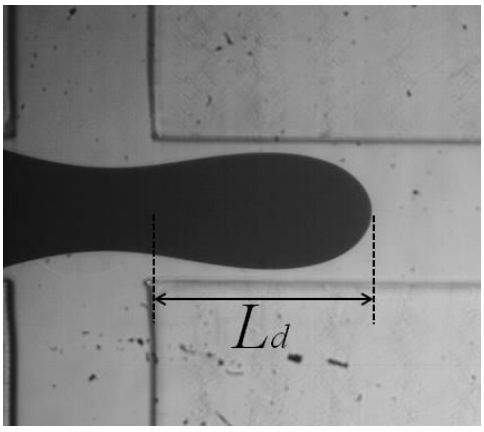

(c)

Fig. 3.3. (a)-(c) Sketch of the maximum width of the expanding thread tip W_l (RM B = 31.10 $\pm$ 0.25 mT), the minimum width of the thinning neck W_s (NM B = 0 mT) and

the thread length in the outlet channel L_d (AM $B = 22.46 \pm 0.16$ mT), respectively.

Fig. 3.4b shows the temporal evolution of the minimum width of the thinning neck W_s in low flow rate region ($Re_c = 0.0793$). The time zero is set as the moment of the final pinch-off of the newly formed droplet. When smaller than channel width W_c, W_s decreases non-linearly with time. According to the previous works, the thinning of the neck is an unstable process [127]. It is found that W_s could be scaled with the remaining time $[-(t-t_c)]$, here t_c is the final pinch-off time before the final detachment by the following function:

$$W_s = a[-(t-t_c)]^b \tag{3-1}$$

When under no magnetic field ($B = 0$ mT), radial magnetic field ($B = 31.10$ and 17.10 mT) and axial magnetic field ($B = 22.46$ mT), the couple parameters (a, b) vary respectively (47.51, 0.32), (53.62, 0.37), (52.26, 0.35) and (34.58, 0.35). When there is no magnetic field, the exponent $b = 0.32$ is within the scope of 0.32 to 0.34 reported by Fu et al. under low Reynolds number [126]. This implies that there is no significant difference between ferrofluid and ordinary fluid. Under the magnetic field in the radial direction, the two parameters (a, b) are bigger than without magnetic field and (a, b) increases with the magnetic flux density. This indicates that the thinning velocity is significantly accelerated by the magnetic field. Under magnetic field in the radial direction, the tip of the dispersed thread is stretched in the radial direction. The initial width of neck increases with the magnetic flux density. This also leads to an increase of the prefactor a. As the degree of obstruction of the channel by the thread tip increases with the radial magnetic flux density, the pressure difference between the two ends of the emerging droplet increases with the magnetic flux density, resulting in the increase of both a and b. When the magnetic field is added in the axial direction, the thread is elongated in the axial direction by the magnetic force. The cross-section of the outlet channel entrance (Fig. 3.4c) is chosen to investigate the accessible area by the continuous phase. S_d and S_c are the area occupied by droplet and the accessible area by the continuous phase in the channel, respectively. Fig. 3.4d shows the ratio of S_d and S_c as a function of time. The time zero starts when the thread tip reaches the edge of outlet channel. Clearly, the droplet only blocks a fraction of the outlet channel. The pressure difference between the two ends of the emerging droplet is then relatively small, so the squeezing from the continuous phase is relative limited.

Therefore at the initial stage, the thinning velocity is small. This explains why *a* is smaller than without magnetic field. At the final pinch-off the head of ferrofluid droplet expands gradually as shown in Fig. 3.1 AM e. This leads to the decrease of the accessible area by the continuous phase, then the pressure difference between the two ends of droplet increases. Meanwhile, the forces (magnetic dragging force and viscous force) acting on the head direct downstream, thus the thinning velocity increases and is closed to that under no magnetic field. And this leads to a relatively greater *b*.

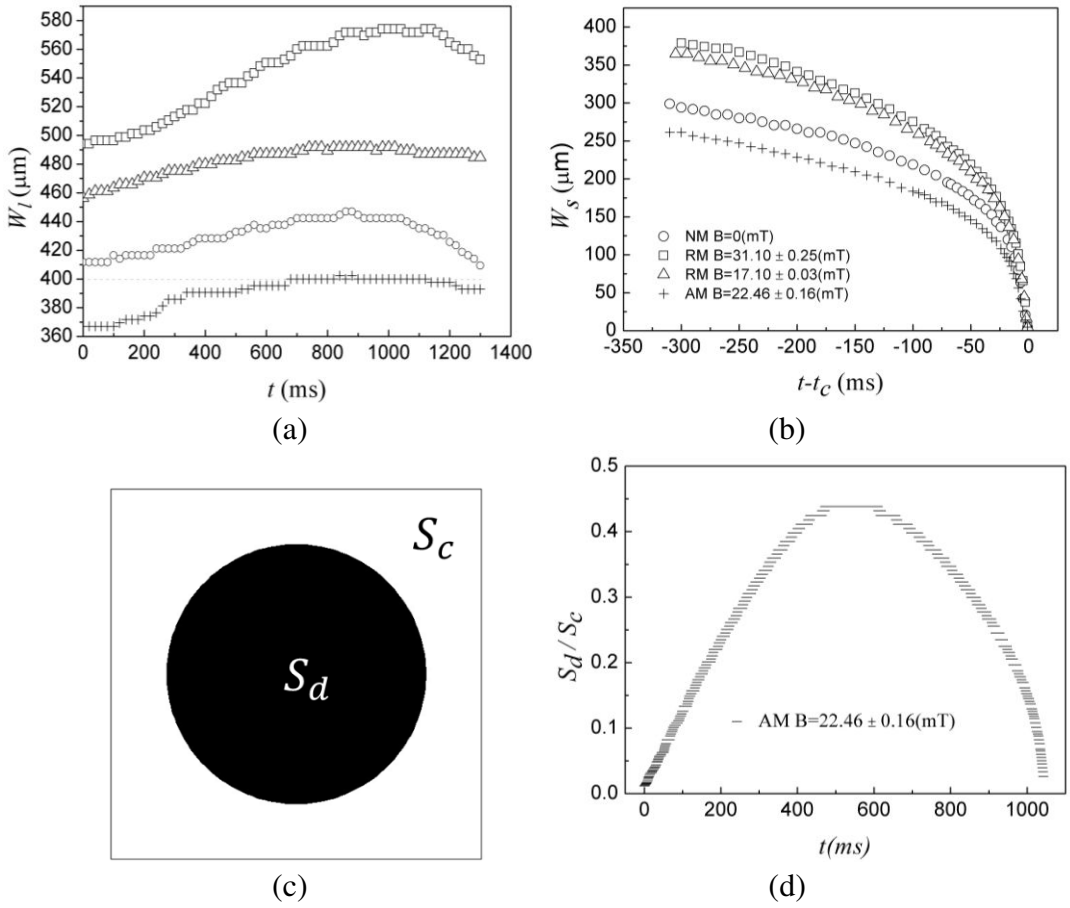

Fig. 3.4. (a) Temporal evolution of the maximum width of the expanding thread tip W_l in low flow rate region (Re_c = 0.0793), here (□), (△), (○), (+) and（⋯）denote RM B = 31.10 ± 0.25 (mT), RM B = 17.10 ± 0.03 (mT), NM B = 0 (mT), AM B = 22.46± 0.16 (mT) and the width of channel (400 μm) (b) temporal evolution of the minimum width of the thinning neck W_s in low flow rate region (Re_c=0.0793), (c) Sketch of the cross-section of the outlet channel entrance, (d) ratio of S_d and S_c as a function of time.

The temporal evolution of the thread tip L_d and the instantaneous velocity V_d is shown in Fig. 3.5a and 3.5b. The time zero T_S is set as the thread tip reaches the edge of the outlet channel and the terminal point T_E corresponds to the moment at which a newly formed droplet detaches from the thread. L_d is the distance from edge of the outlet channel to the thread tip. As shown in Fig. 3.5b, at the first stage, due to the leakage of continuous phase in the space between droplet and outlet channel walls, the instantaneous velocity V_d is smaller than the total superficial velocity $V_t = (Q_c + Q_d) / W_C$. The instantaneous velocity V_d varies according to the order: AM < NM < RM. Under AM, the thread is stretched in the axial direction. However the leakage space exists still. The pressure difference between thread tip and the intersection region pushing forward the thread downstream is relatively smaller comparing with RM and NM conditions. Furthermore, the expanding thread in the intersection region under RM and NM is squeezed into the outlet channel by the continuous phase during this period, results consecutively in much higher velocity. When the cap moves forward, the accelerations under RM and NM stem from the enhanced thinning of neck due to the increasing pressure difference, while the acceleration under AM is mainly due to viscous force. Under RM and NM, the pressure increase makes the ferrofluid in the thinning neck to flow partially into the thread tip. The instantaneous velocity V_d can exceed V_t. Under AM, the thread tip expands gradually (Fig. 3.1 AM d and e). The combined effect of the increased pressure difference, viscous force and magnetic force acting on the cap leads to an exceeding of V_d over V_t. Fig. 3.5a indicates that L_d increases non-linearly with time into outlet channel under three different configurations, in particular L_d much longer under AM than RM and NM. The time interval $\Delta t = T_E - T_S$ follows the order: RM < NM < AM, logically in agreement with the dynamic thinning velocity: AM < NM < RM as stated before. When the magnetic field is added in the axial direction, the time interval Δt increases significantly but the Δt difference between RM and NM is relatively limited. The explanation arises from the fact that the initial W_s is larger under RM. In summary, the main difference between RM and NM exists during the expanding stage, owing notably to the acceleration by RM. The thread is much larger in the intersection region. While the main difference between AM and NM occurs for the thinning process, more time is required to pinch-off under AM. Obviously, the magnetic field facilitates the generation of larger droplets under AM and RM.

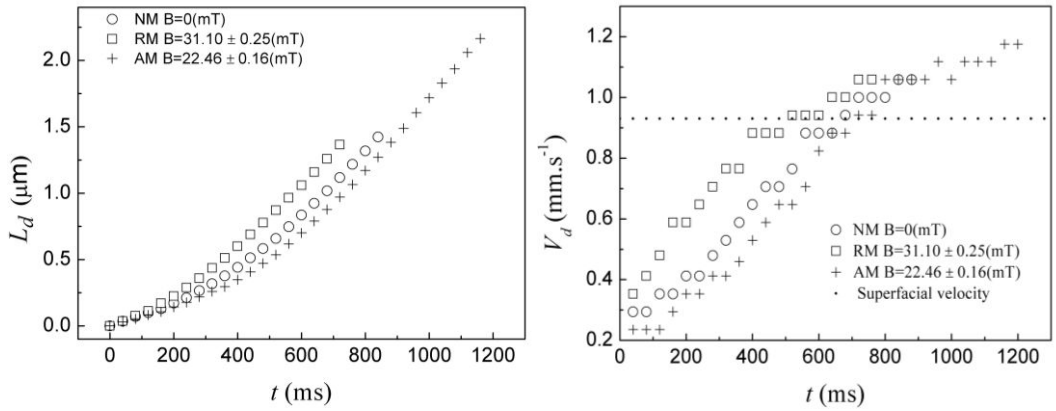

(a) (b)

Fig.3. 5. (a) Temporal evolution of the thread length in the outlet channel L_d, and (b) front velocity of the thread tip in low flow rate region (Re_c = 0.0793).

When the droplet is formed in the high flow rate region (the Reynolds number of continuous phase Re_c > 0.5), the relative volume V_m / V_n is closed to 1. This implies that the effect of the magnetic force is negligible. An example (Re_c = 0.793) of the temporal evolution of the maximum width of the expanding thread tip W_l and the minimum width of the thinning neck W_s is illustrated in Fig. 3.6a and 3.6b. As shown in Fig. 3.6a, W_l under RM is close to W_c, but the W_l under NM and AM is less than W_c. This indicates that the magnetic field applied in the radial direction plays a role in the initial expanding stage. While under AM or NM, the expanding mechanism is similar, the thread tip detaches from the main channel. Although there is a difference between W_l under different magnetic fields， the magnitude is relatively small compared with the observation in the low flow rate region. The tendency of W_l is quite similar under RM, AM and NM. The expanding period is shorter than the low Reynolds number of the continuous phase. This explains also the reduction of the influences of magnetic field.

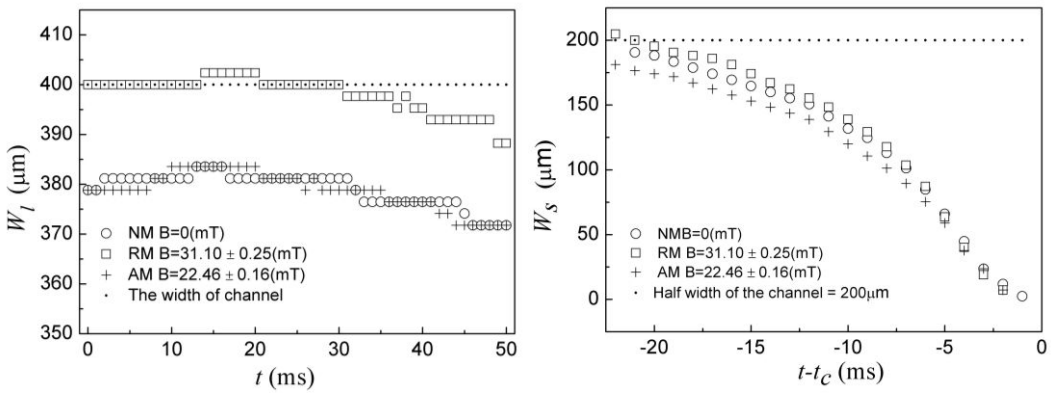

(a) (b)

Fig. 3.6. (a) Temporal evolution of the maximum width of the expanding thread tip W_l in high flow rate region (Re_c = 0. 793), (b) temporal evolution of the minimum width of the thinning neck W_s in high flow rate region (Re_c = 0. 793).

Fig. 3.6b illustrates the minimum width of the thinning neck W_s in function of time. W_s is also well scaled with the remaining time before the final pinch-off as a power-law relationship: $W_s = a[-(t-t_c)]^b$. When under no magnetic field (B = 0 mT), radial magnetic field (B = 31.10 mT) and axial magnetic field (B = 22.46 mT), (a, b) belong to (31.73, 0.60), (32.67, 0.61) and (27.58, 0.62), respectively. The relative difference is smaller in comparison with the regime of low Reynolds number. The thinning period is much shorter as shown in Fig.3.6. According to the previous works [90, 126, 128], the size of droplet decreases with the increase of the continuous phase flow rate. In high flow rate region, the droplets formed are smaller. As the magnetic field acts as a volume force [123], the influence of the magnetic force decreases with the increase of the continuous phase flow rate. Furthermore, the magnetic particles in ferrofluids could organize in lines in a magnetic field [120]. The alignment would be reduced with the increase of the flow rate of the dispersed phase. The influence of magnetic field on the droplet formation diminishes consecutively. In summary, the relative volume V_m / V_n decreases with the increase of the continuous phase flow rate.

3.3 Conclusions

In this chapter, both radial and axial magnetic fields were applied to realize the active control of the ferrofluid droplet formation in flow-focusing configuration. A critical Reynolds number of the continuous phase ($Re_c = \rho_c u_c w_c/\mu_c$ = 0.5) can be proposed to distinguish high and low flow rate regions. In general, the applied magnetic field

facilitates the formation of larger droplets but the effects of magnetic field decrease with the increase of flow rates. The different application types of magnetic field affect various stages during the droplet formation. The magnetic field applied in the radial direction plays mainly a role in the expanding stage. The expanding velocity of the thread is faster under this kind of magnetic field. The volume of the expanding tip exceeds that under NM and AM. While the magnetic field applied in the axial direction modifies essentially the thinning stage by elongating the thread and delaying the breakup.

Chapter 4 Droplet (Bubble) breakup process in a microfluidic T-junction

Once droplets are generated they probably travel along a series of conduits that compose the microfluidic network. For the simple case of a straight outlet channel, droplets move along the channel at a fixed speed and spacing. However, when junctions are added, droplets can breakup or choose one path flowing away. Large number of previous work studied the droplet (bubble) behaviors at microchannel node and developed suitable models to predict the critical condition for breakup. These models also demonstrate the dependence between the node geometry and the droplet behaviors. Therefore, some active methods such as magnetic field and electrical field were utilized to offer additional degree of freedom. Additionally, the behaviors of droplet will increase the complexity no matter it breakup or not. The increasing complexity lies in the fact that droplets alter the hydrodynamic resistance of the channel they travel within which influences the global flow field. This creates a feedback effect, whereby the decision made by a preceding droplet influences the decision of subsequent droplets. In addition, due to the higher surface tension in gas-liquid system compared to the counterpart in liquid-liquid system, the feedback effect is particularly notable when bubble appears at micro-node. Thus, in this chapter, we focus on the influences of external field and the feedback effect.

The first part aims at investigating the influence of external magnetic field on the breakup dynamics of the water-based ferrofluid (EMG 807) droplet in a microfluidic T-junction, thereby utilizing the magnetic field to precisely control the droplet behaviors. In this part, the whole breakup processes of the ferrofluid droplets under uniform magnetic field and non-uniform magnetic field were exhaustively considered. The influence of both the flow rates and magnetic flux density on the formation and breakup were extensively studied.

Moreover, the previous works demonstrate that bubble and droplet behavior is highly nonlinear at the junction owing to the hydrodynamic collective feedback or hydrodynamic memory. The interplay of coherent resistance of the channels and the

additional resistance arisen by the bubbles and droplets complicates the manipulation. And not only that, duo to the higher surface tension of bubble compared with droplet the feedback effect is more pronounced. Therefore, the second part studied the hydrodynamic feedback effect on the asymmetrical breakup of bubbles at a microfluidic T-junction divergence stemming from of bubble collision at the T-junction convergence downstream by a high-speed digital camera. The experiments were performed under gas/liquid flow rates ratio ranging from 0.084 to 4.333. The microfluidic channels have uniform square cross-section with 400μm wide and 400μm deep. Four bubble behaviors (bubble pair asymmetrical collision, bubble pair staggered flow, single bubble flow and dynamic transformation flow) were observed at the T-junction convergence in different gas and liquid flow rates. The feedback effects of asymmetrical collision and staggered flow of bubble pairs at the T-junction convergence on bubble behavior at the T-junction divergence were mainly investigated.

4.1 Introduction

4.1.1 The breakup of droplet under magnetic field

The droplet-based microfluidics is capable of precisely handling minute amounts of fluidic elements [129-131]. Under micro scale, these systems possess high interfacial areas and short diffusion distance which facilitate the heat and mass transfer [132]. Thus much attention has been paid to their applications in chemical engineering [133, 134], biochemistry analysis [27, 135], materials synthesis [136] and so on. To achieve successfully these applications, the control of droplets' size is of prime importance. In the present studies, the droplet size is controlled during droplet generation and the breakup/coalescence processes downstream [73, 83, 131, 137]. Most of these studies take advantage of geometry-based passive methods [137]. The formations of droplets take place usually in T/Y-junction [12, 78, 138-141], co-flow [46, 142] and flow-focusing [32, 143] micro devices. The generations of droplets under different operating parameters and various flow regimes such as squeezing, dripping and jetting were studied [32, 144-146] [147]. Some physical models were proposed and previous works show that the droplet size increases with the flow rate ratio of dispersed phase to continuous phase. The breakup and coalescence process downstream can be regarded as competing

mechanism: the former decreases the droplet size while the latter increases it. To breakup droplets in a microfluidic device, various geometries were employed. Besides T/Y junction, obstacles can be placed in microchannels [131, 137, 148]. In these devices, the size ratio of daughter droplet can be controlled [137, 148-150] by changing the length ratio, cross section ratio of the branches of the junction or by changing the position/length of obstacles. To realize the coalescence between droplets [102, 151, 152], divergent and convergent structures are mainly used to facilitate contact and collision between droplets.

Within geometry-based passive microdevices, the droplet size is mainly determined by the device geometry [144, 145, 148-150]. For a given geometry, it is difficult to casually modulate the size of droplets. It is then necessary to make use of external factors to regulate the size of droplets. Several works have elaborated local control coupled with the flow rate ratio to extending the droplet size distribution [69, 71-73, 153-155]. He *et al*. transformed the flow front of the dispersed phase to a Taylor cone in turn causing Rayleigh capillary instability to control the breakup processes. Ho *et al*. controlled the viscosity and interfacial tension by local heating to adjust the sizes of droplets. Cheung and Qiu utilised the acoustic actuation to bring periodic oscillation to control the sizes of droplet. Recently, the magnetic manipulation has attracted much attention [69, 71-73, 153-155]. The magnetic field will neither induce thermal effect nor affect pH, surface charge and ionic concentration [156]. In contrary to laser, acoustic actuation and electric field, it is simple and practicable to endow a fluid with the paramagnetic character by adding a minute amount of nano-scale magnetic particles [73, 156, 157]. Therefore, it is straightforward to manipulate the formation of ferrofluid droplets by an external magnetic field [71-73, 158, 159]. The effects of uniform and non-uniform magnetic fields on the droplet formation of ferrofluids are studied [158, 159]. The first work in T-junction concerns the active control of droplets' size by changing the magnet positions [72]. When the magnet is placed at the downstream of the T-junction, the formation of bigger droplets is favoured. Inversely, it forms smaller droplet. Some similar observations were also made in flow-focusing device, in particular under a uniform magnetic field [71-73, 158, 159]. Under a radial uniform magnetic field, the magnetic force acting on the droplet offsets some part of the impact force of the continuous phase during expanding process of droplet. While under axial magnetic field, the magnetic force stretches the droplet to enlarge the flow section for the

continuous phase within the microchannel to expel. The impact force of the continuous phase on droplet is then reduced. To our best knowledge, only a very few studies focus on the breakup dynamics of ferrodroplets. Our present work aims to study the breakup of ferrodroplets in T-junction under uniform and non-uniform magnetic fields.

4.1.2 Asymmetrical breakup of bubble due to feedback

Compared with Liquid-Liquid systems, the Gas-Liquid systems are afflicted heavily with the feedback effect due to much larger surface tension. This feedback particularly affects the performance of a microfluidic device. To illustrate, the feedback effect in a loop is notable. When a bubble/droplet flows into a loop it will choose a branch to flow away if no occurrence of breakup in the inlet node. This behavior will cause the resistance variation of each branch and accordingly influence the choice of subsequent bubble/droplet. In general, this feedback effect is nonlinear [86, 88, 129, 160-164]. Results show that flow patterns of bubble/droplet were mainly affected by operating conditions and the geometry of microchannel [59, 165].

More specifically, Sessoms *et al*. studied droplet flows in microfluidic networks both experimentally and numerically [88]. During their experiments, they found two kinds of flow patterns: filtering regime and repartition regime. The transformation of these two regimes depended on the spacing between droplets λ before flowing into the loop, excess resistance length L_d resulting from the presence of droplet in the branch and the ratio of two branches length Λ. When $2L_d > (\Lambda-1)\lambda$, the droplet flow followed repartition regime, contrarily it fell into filtering regime. The flow of droplets in the loop is simplified in their numerical simulation. Once λ, Λ and L_d are preset, the droplet reaching the loop inlet chooses a channel with lower resistance by logical judgment without knowing the details of flow fields in the loop. Their experimental results could be predicted successfully by the numerical simulation. Furthermore, Cybulski *et al*. studied the transformation between sub-regimes within repartition regime utilizing artificial disturbance method [160]. Belloul *et al*. investigated the influence of droplets' collision on flow patterns, and they proposed two physical mechanisms regulating flow pattern at the bifurcation: collision and collective hydrodynamic feedback affecting droplet, whether collision or hydrodynamic feedback remains dominant relied principally on the droplet confinement (the ratio of

droplet radius to microchannel radius) and the distance between two consecutive droplets [86, 129].

Although several experimental efforts have been devoted to the flow behaviors of droplet in a loop [86, 88, 160, 161], and similar bubble and droplet behaviours were found at a T-junction divergence [77, 78, 130, 166]. To our best knowledge, little attention has been paid to the feedback effect of bubble behaviors at the T-junction convergence on the bubble breakup at the T-junction divergence of a loop. This work is mainly focused on the asymmetric breakup of bubbles at the T-junction divergence, owing to the feedback effect of bubble collision at the T-junction convergence in a loop.

4.2 Results and discussion

4.2.1 Ferrodroplet breakup

4.2.1.1 Droplet breakup and non-breakup in the T-junction under uniform magnetic fields

Previous studies indicate the behaviors of droplets at the T-junction depend on the droplets' size L or the dimensionless length $\varepsilon = L/\pi W_c$ (here W_c denotes the width of the channel) and the capillary number Ca [131, 137, 148]. In our experiments, the influence of these two parameters and the magnetic flux densities will be addressed. To gain a comprehensive insight into the effect of a uniform magnetic field (UM), it is suitable to study different breakup regimes at T-junction of a symmetric loop (Fig.2.1b).

There are four main breakup regimes for water-based ferrodroplet at the T-junction both under uniform magnetic field (UM) and no magnetic field (NM) as illustrated in Fig. 3a, b, c, d. The breakup processes without magnetic field (NM) are introduced as a reference for comparison. These different regimes provide a visual description of the influence of a magnetic field.

(1) Breakup with permanent obstruction (BPO) as shown in Fig. 4.1a

Droplets penetrate T-junction with two branches obstructed by the droplet under UM and NM. The difference between the breakup processes under UM and NM is inconspicuous. Within optical resolution limits, there is no free flow section between the droplet and the walls adjacent the feed channel during the entire breakup process. The two dumbbell-like parts in each branch obstruct the continuous flow and finally breakup symmetrically into two daughter droplets.

(2) Breakup with temporary obstruction (BTO) as shown in Fig. 4.1b

At the beginning of neck forming process, the two dumbbell-like parts enter into contact with the walls adjacent the feed channel and the tunnel between them is not observable. With the development of the thinning process of the neck, the two dumbbell-like parts detach from the walls to give rise to flow tunnels. It is obvious that under UM the tunnel is much bigger than the case under NM as the ferrofluid droplet is stretched by the magnetic force which is perpendicular to the feed channel by posing two magnets on both sides of the device as shown in Fig. 2.2. Then after a moment, the droplet breaks into two identical daughter ones.

(3) Breakup without obstruct (BNO) as shown in Fig. 4.1c

After reaching at the T-junction, the droplet stretches but the neck is not formed immediately. The droplet approaches to the wall opposite to the feed channel, replaces the former droplet stops near the stagnation point until the arrival of the next droplet. After the impact of the new coming droplet, it breaks into two daughter ones. During the whole process, the flow tunnels are clearly visible between droplet and the side walls of the branches, allowing the continuous phase to flow through during the breakup. Moreover, there is no obvious difference between two breakup process under UM and NM.

(4) Non-breakup (NB) as shown in Fig. 4.1d

Droplets enter into the T-junction and then flow out from either of the bifurcations depending on the feedback of the former droplets which still flow in the loop[160]. This regime occurs under relative small flow rate and small droplet size.

The breakup of these droplets at the T-junction depends on the droplet size L or the dimensionless droplet size ε and the capillary number Ca [77, 131], as illustrated in Fig.

4.2 a, b, c, d. Non-breakup occurs at small droplet size. Between non-breakup (NB) and breakup without obstruct (BNO), there exists an unstable breakup (NS) region. In this region, the mother droplets are sensitive to the distribution of the continuous phase in the two branches. The feedback effect at T-junction due to impact of daughter droplets from two branches will bring a fine difference of flow rates between two branches. This could lead to a non-breakup of the mother droplet. Subsequently, the following will not breakup until the new balance is reached. Thus the droplets arrive at T-junction breaking into two daughter ones or not in an irregular way. Certainly, this configuration occupies relatively narrow domain. With the increase of the dimensionless droplet size, the BNO, BTO and BPO scenarios occur sequentially. It can be observed in Fig 4.2 a, b, c, d. that the BTO region gradually enlarges towards BPO with the increasing magnetic flux densities. Fig. 4.2e depicts the displacement of the frontier between BTO and BPO. This is caused by the elongation of ferrofluid droplets due to magnetic force [157]. The ferrofluid droplet is stretched in the direction of the uniform magnetic field. This direction is parallel to the branches of T-junction, thus the two dumbbell-like parts detach from the walls offering larger flow sections of the continuous phase in two branches as shown in Fig. 4.1b. According to the previous works [157], the magnetic force which stretches the droplet is proportional to the square of the magnetic field strength *H*. The stable shape of the droplet is determined by the ratio of interfacial tension and magnetic force in unbounded flow. The magnetic Bond number was used to represent the ratio between magnetic force and surface tension $Bo = \mu_0 \chi W_c H^2/\sigma$ (Nguyen 2012). Here $\mu_0 = 4\pi \times 10^{-7}$ N/A^2 is the permeability of the free space. For *B* increase from 0 to 24.1, 52.1 and 89.8 mT ($B = \mu_0 H$), Bo ranges from 0, 47.7, 222.8 to 661.9. The droplet aspect ratio *b/a* (*b* is the major axis of droplet and *a* the minor axis) increases with the magnetic Bond number *Bo*. Therefore, the increase of magnetic intensity enlarges the area of BTO region towards BPO region. As shown in Fig. 4.2, the area for BNO is barely changed. This is due to the small droplet size and the tunnels are inherent. The external magnetic field expands only the opening of the tunnels.

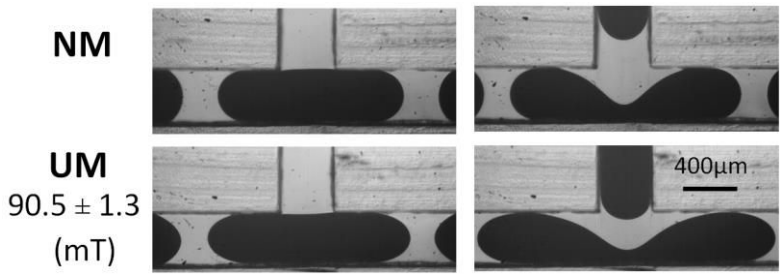

(a)

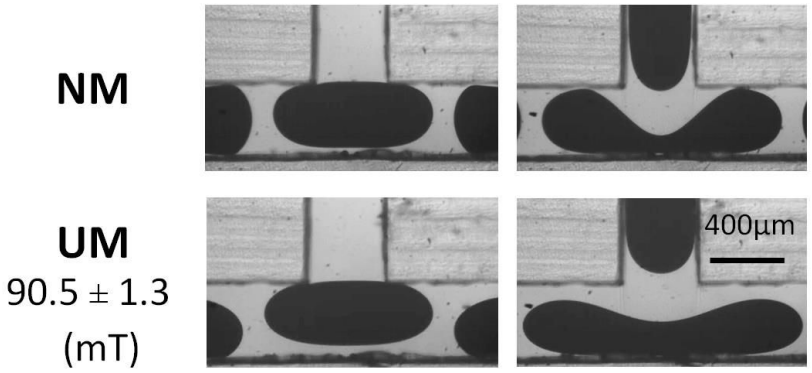

(b)

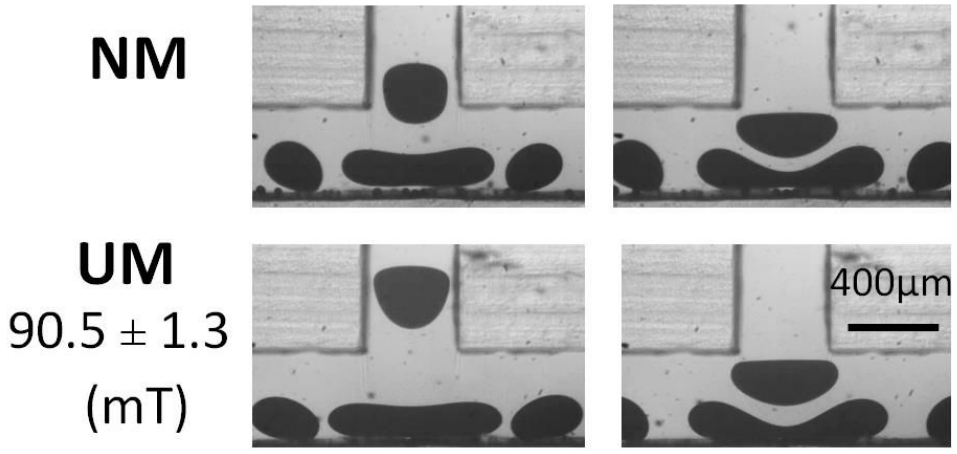

(c)

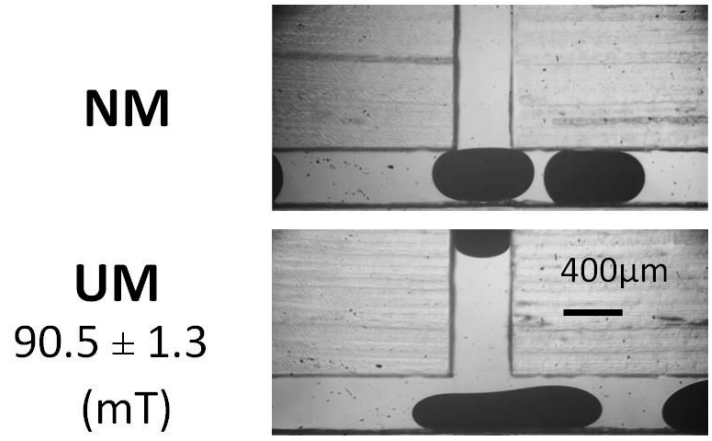

(d)

Fig. 4.1 Breakup process of ferrofluid droplets in the T-junction divergence.

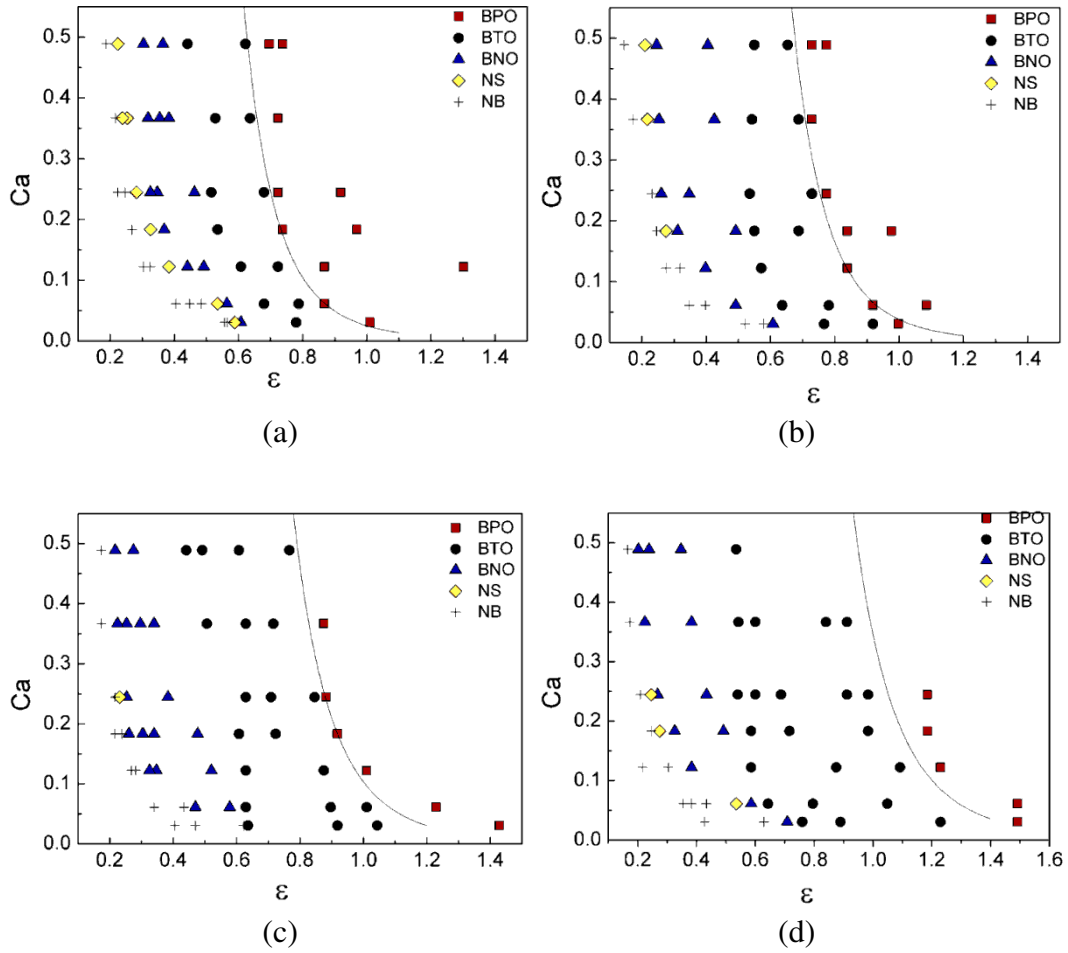

(a) (b)

(c) (d)

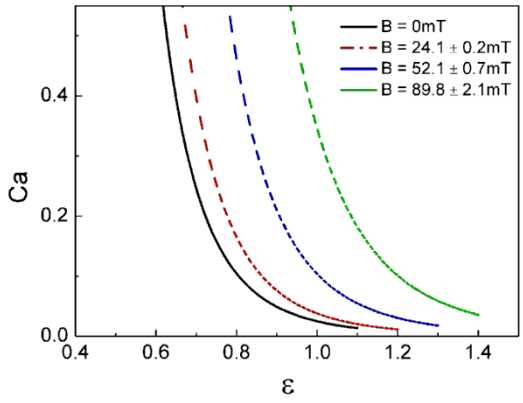

(e)

Fig. 4.2 (a)-(d) Operating diagram organizing droplet behavior as a function of capillary number *Ca* and the dimensionless bubble size ε under 4 different magnetic flux densities. The dotted line represents the critical capillary number for the transformed from BPO to BTO region. (e) The displacement of the critical capillary number as the increase of the magnetic flux densities.

The uniform magnetic field affects not only the type of breakup, but also the breakup processes. As illustrated in Fig. 4.3, the temporal evolution of the minimum width of the thinning neck W_n in BPO (Fig. 4.3a), BTO (Fig. 4.3b) and BNO (Fig. 4.3c) regions. The time zero is set at the moment of the droplet entirely penetrates into the branches. Obviously, the breakup process in BPO region is barely influenced by the external magnetic field. The evolution of the neck thickness W_n in the early stage ($W_n > 0.5W_c$)[149, 167] is approximately in agreement with the previous data in the literature [131, 149, 167]. As shown in Fig. 4.3a, the scaling law $(c\text{-}W_n) \sim t^{3/7}$ describes well the data in the early stage with c as a fitting constant here. Leshansky *et al*. deduced the scaling law based mainly on the mass conservation in the depression region [131]. This prerequisite imposes that the volume change of the depression region is equal to the inlet flow rate during the breakup. As a consequence, the tunnels as shown in Fig. 4.3 disappear with decreasing flow rates in those gutters. But the prerequisite is invalid in the second stage ($W_n < 0.5W_c$), where the neck starts autonomous pinching. During the second stage, the flow rate in the gutters cannot be ignored [149, 167]. The flow reversal from these gutters accelerates the pinch off of the neck [149, 167]. These explain why the scaling law deviates from the experimental data in this stage. In BNO region, the flow section is relative larger, thus the enlargement of the tunnels due to the elongation of the droplets are slight. The breakup process is slightly accelerated by the magnetic force. But the external magnetic field plays an important role while the

breakup processes locate within BTO region. With increasing magnetic flux densities, the breakup process takes longer. The deceleration of the thinning rate becomes increasingly dominant in the middle of the breakup process revealed in Fig. 4.3b. It is clear that the scaling law $(c\text{-}W_n) \sim t^{3/7}$ conforms to the data only at the beginning of the breakup processes. As the increase of the magnetic intensities, the deviations become more significant. We find that the appearance of the deviation can be related to the opening of the tunnels between the droplet and the walls.

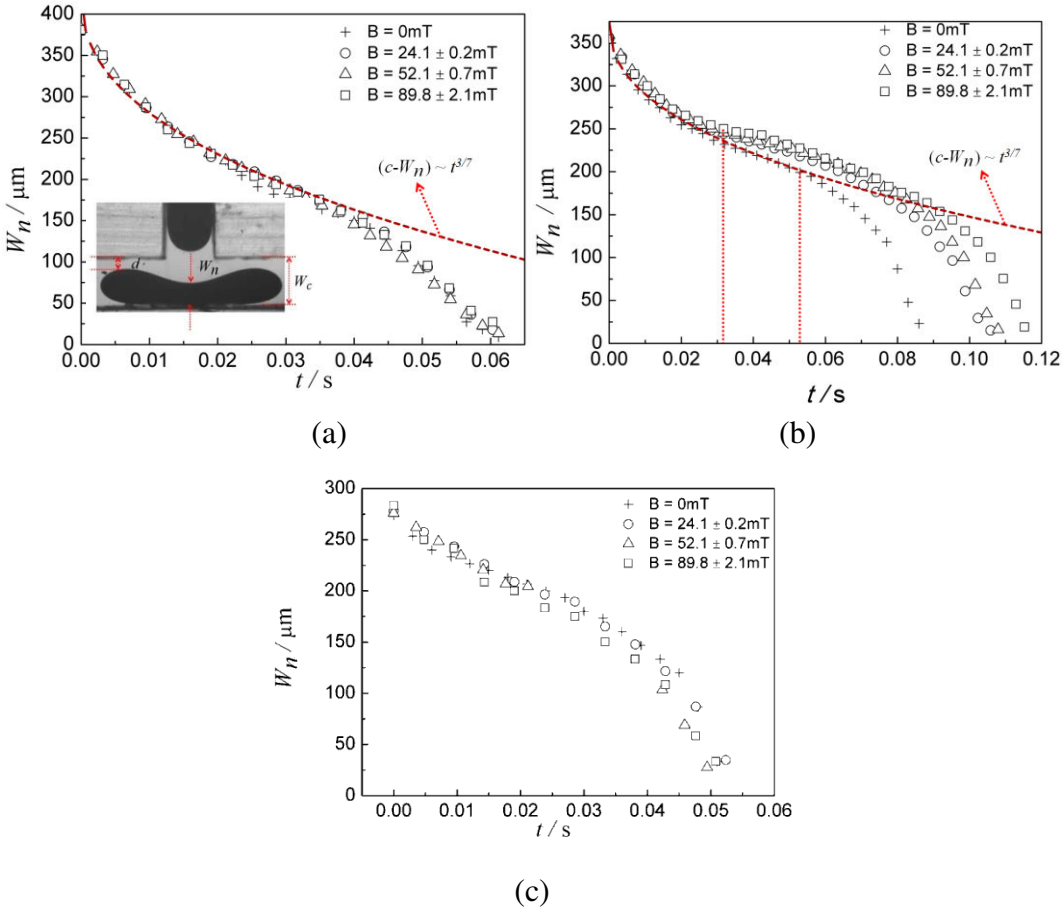

Fig. 4.3 (a)-(c) Temporal evolution of the minimum width of the neck W_n as a function of time in BPO, BTO and BNO region, respectively under 4 different magnetic flux densities.

Fig. 4.4 describes the temporal evolution of the minimum dimensionless width of the tunnel d / W_c. As shown in Fig. 4.4, the magnetic field causes an early appearance of the tunnels and the enlargement of the flow section. In our experiments, there is a critical value of the d / W_c. Above 0.08 ± 0.02, the deviations between the data and the scaling law appear. This reveals the leakage from the tunnels cannot be ignored

when d / W_c exceeds 0.08±0.02. Considering Fig. 4.3b and Fig. 4.4, as the difference of d / W_c increases, the difference of thinning rate becomes gradually pronounced, due to the augmentation of leakage of the continuous phase from the tunnels with the increase of d. Furthermore, it seems that the pressure difference between droplet cap and neck decreases and at the same time the shear of continuous phase acting on droplet increases. This implies that in BTO region, the pressure difference is the primary factor to determine the breakup process.

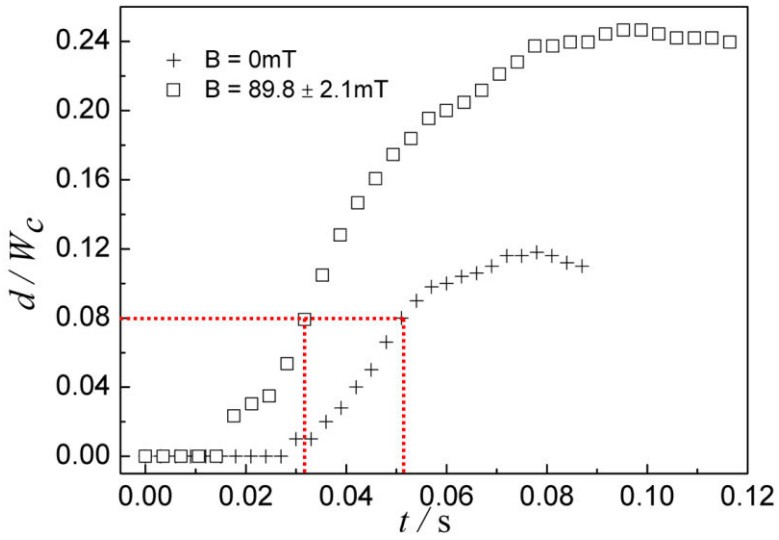

Fig. 4.4 Temporal evolution of the minimum dimensionless width of the tunnel d / W_c as a function of time under 2 different magnetic flux densities.

4.2.1.2Droplet breakup and non-breakup in the T-junction under non-uniform magnetic fields

Under a non-uniform magnetic field, the magnetic force F acting on droplet is not symmetrical [168]. In our experiments, the magnet was placed at the left side of the microchannel. Under such a magnetic field, the breakup of the ferrofluid droplet becomes asymmetrical due to the magnetic force applied in the left direction. Two daughter droplets with different sizes flow into two opposite branches as shown in Fig. 4.5. These daughter droplets bring additional flow resistances to the branch which they flow through [137]. And the additional flow resistance due to a droplet increases with the increase of droplet size [169]. This gives rise to feedback effects and affects then the flow distribution of continuous phase at the T-junction. In our experiments, the breakup of droplet occurs in a symmetric loop; the breakup process is mainly

controlled by the magnetic field and the continuous flow. But the T-junction divergence and the T-junction convergence is nearly of the equipotential line in the magnetic field. The magnetic field affects only the breakup processes but does not provide additional energy to the daughter droplets. The kinetic energy is only provided by the continuous phase. Thus the influences of the magnetic field and continuous phase are coupled to some extent.

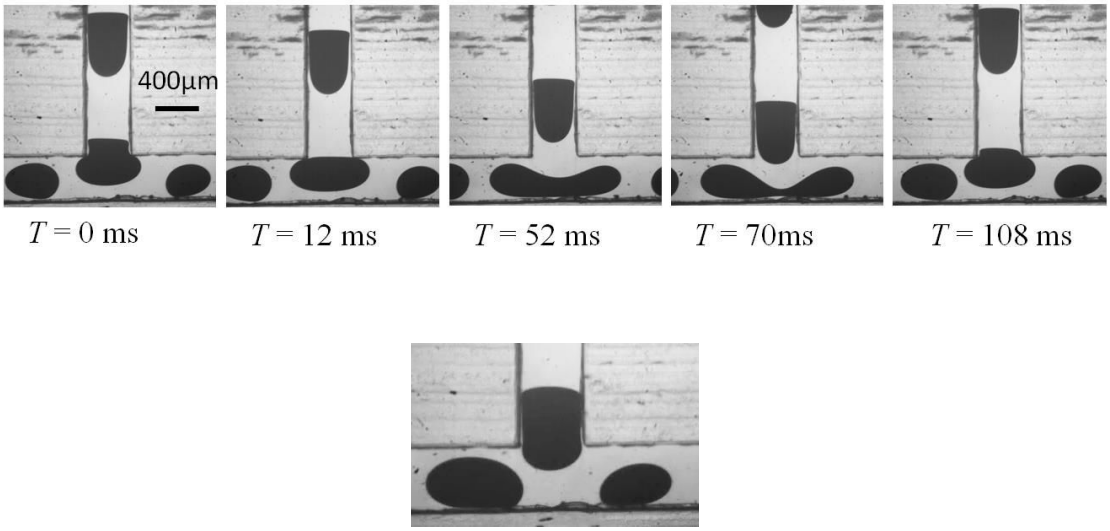

Fig. 4.5 Temporal evolution of the asymmetric breakup of a ferrofluid droplet.

Fig. 4.6a shows the volume ratio of the droplets flowing in the right branch and in the left branch V_R / V_L (here V denotes droplet volume and subscripts R and L mean 'right' and 'left') as a function of the total flow rate of both phases $Q_t = Q_c + Q_d$ under three different magnetic flux densities. The size of mother droplets is controlled by a fine adjustment of continuous and dispersed phases to maintain the length within a narrow range of 630 ± 30 μm. Fig. 4.6a reveals that the ratio V_R / V_L decreases obviously with the increase of the magnetic flux density. In general, the volume ratio V_R / V_L increases with Q_t. This implies that the hydrodynamic force plays an increasing role. To assess this point, we use the velocity ratio of droplets in the right and left branch U_R / U_L to represent the flow rate ratio in two branches. As shown in Fig. 4.6b, the velocity ratio U_R / U_L was measured as a function of Q_t. With the increase of Q_t, the ratio U_R / U_L decreases gradually towards an asymptotic value of one. The hydrodynamic force should be dominant when the total flow rate Q_t is very high.

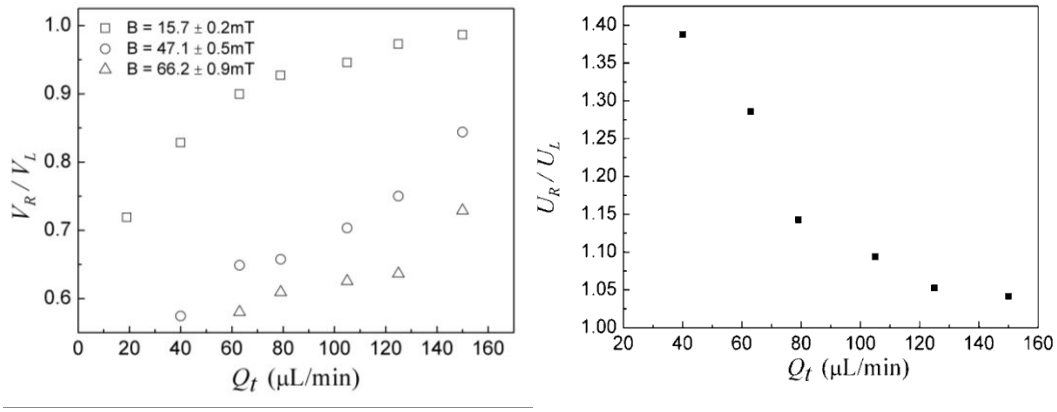

(a) (b)

Fig. 4.6 (a) Volume ratio of the droplets flowing in the right branch and in the left branch V_R / V_L as a function of the total flow rate Q_t under three different of magnetic flux density. (b) The velocity ratio of droplets in right and left branch U_R / U_L as a function of the total flow rate Q_t.

Furthermore, the flow rate ratio between the continuous phase and dispersed phase Q_C / Q_d exerts also an influence on the breakup of mother droplets. Keeping a constant total flow rate Q_t at 50 μL/min, the flow rate ratio Q_C / Q_d was varied. Fig. 4.7 shows the variation of the volume ratio V_R / V_L in function of the flow rate ratio Q_C/Q_d. V_R/V_L decreases with either the increase of the flow rate ratio Q_C/Q_d or the augmentation of the magnetic flux density. The decrease rate grows with the increase of the magnetic flux density, but the difference between these decrease rates diminishes. This is probably due to the feedback of daughter droplets in each branch. As illustrated in the inset of Fig. 4.7, the distance between droplets is small for relatively lower Q_C / Q_d. The daughter droplets in the left branch are larger due to the applied magnetics force. As a consequence, the flow residence grows in the left branch to lead to a decrease of the continuous flow rate in this branch. The velocity of these droplets pushed ahead by the continuous phase decreases logically. Moreover, the separation distance between daughter droplets in left side decreases also to induce some squeezing effects. During the breakup process of a mother droplet at the T-junction, the droplet cap in the left branch was hampered by the daughter droplet. The influence of the magnetic force is then limited when Q_C / Q_d is relative small. Fig. 4.7 shows that under the higher magnetic flux densities (B = 38.9±0.4mT, B = 52.1±0.7mT) and Q_C / Q_d, the volume ration V_R / V_L becomes zero: all droplets go to the left branch without breakup. The non-uniform magnetic field facilitates the

non-breakup of droplets.

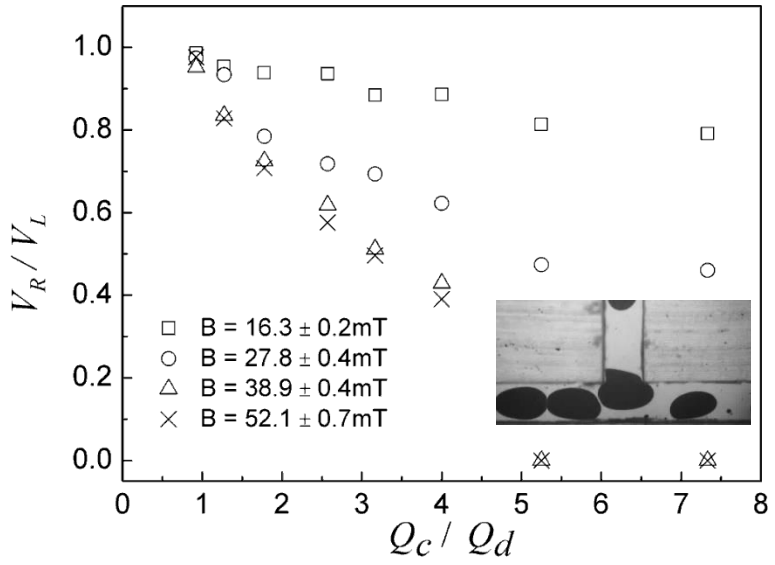

Fig. 4.7 Volume ratio V_R / V_L as the function of the flow rate ratio Q_C / Q_d. (Inset) The flow condition when Q_C / Q_d is equal to 1.778.

4.2.2 Bubble breakup

4.2.2.1 Bubble behaviors at the T-junction convergence

The bubble behaviors at the T-junction convergence and T-junction divergence of the symmetric loop (Fig. 2.1c) were systematically investigated. In our experiment, four categories of bubble behaviors at the T-junction convergence were observed (Fig. 4.8): bubble pair asymmetrical collision, bubble pair staggered flow, single bubble flow and dynamic transformation flow (an alternate presentation of symmetrical and asymmetrical collision of bubble pairs). Whether bubble collision takes place is determined by the relationship between the time for the first one of the two daughter bubbles flowing through the outlet of the loop t_L and the time difference of the two daughter bubbles arriving at the T-junction convergence t_d. The time t_L could be estimated as $t_L = L_B/U_A$, where L_B and U_A denote the length and the average velocity of the first one of the two daughter bubbles passing through the outlet, respectively. And $t_d = |L/V_1 - L/V_2|$, where L, V_1 and V_2 denote the branch length of the loop, the velocity of the bubble in the left and right branch, respectively. When $t_d < t_L$, the

asymmetrical collision of two daughter bubbles occurs. Under this circumstance, one of the two daughter bubbles can slip through another, then the two bubbles flow downstream into the exit channel in a pair end-to-cap (Fig. 4.8A1), or one bubble first enters into the exit channel and subsequently is sniped into two parts (Fig. 4.8A2), then the three bubbles travel downstream one after another. When $t_d > t_L$, staggered flow occurs without contact between the two bubbles (Fig. 4.8B). This means that one of the daughter bubble pair passes through the T-junction convergence first, and then the latter one arrives at the exit. As a result, no collision occurs. In this case two sub-regimes could be found: non collision of uniform daughter bubbles (Fig. 4.8B1): non collision of non-uniform daughter bubbles (Fig. 4.8B2). Fig. 4.8C shows the bubble behavior when gas flow rate is relatively low, for instance, less than 1mL/min in our experiment. In this situation, the mother bubbles enter into the divergence without breakup, then flows into the branch with higher instantaneous flow rate, consequently, no other bubble appears in the opposite channel while the bubble arrives at the exit, this phenomenon is named as single bubble flow. This flow regime has also been systematically studied by theoretical, numerical and experimental investigation [86, 129, 162-164]. In our experiment, dynamic transformation flow is also visualized. In this regime, bubble pair symmetrical collision (Fig. 4.8D1) and bubble pair asymmetrical collision (Fig. 4.8D2) present alternately. It is worth noting that the collision of bubbles at the microfluidic T-junction convergence is quite similar to the behavior of droplets at such a device [170]. However, late splitting (Fig. 4.8F) was rarely observed in our experiment owing to the lower density and viscosity of bubbles than those of droplets. More detailed information will be presented in the next section.

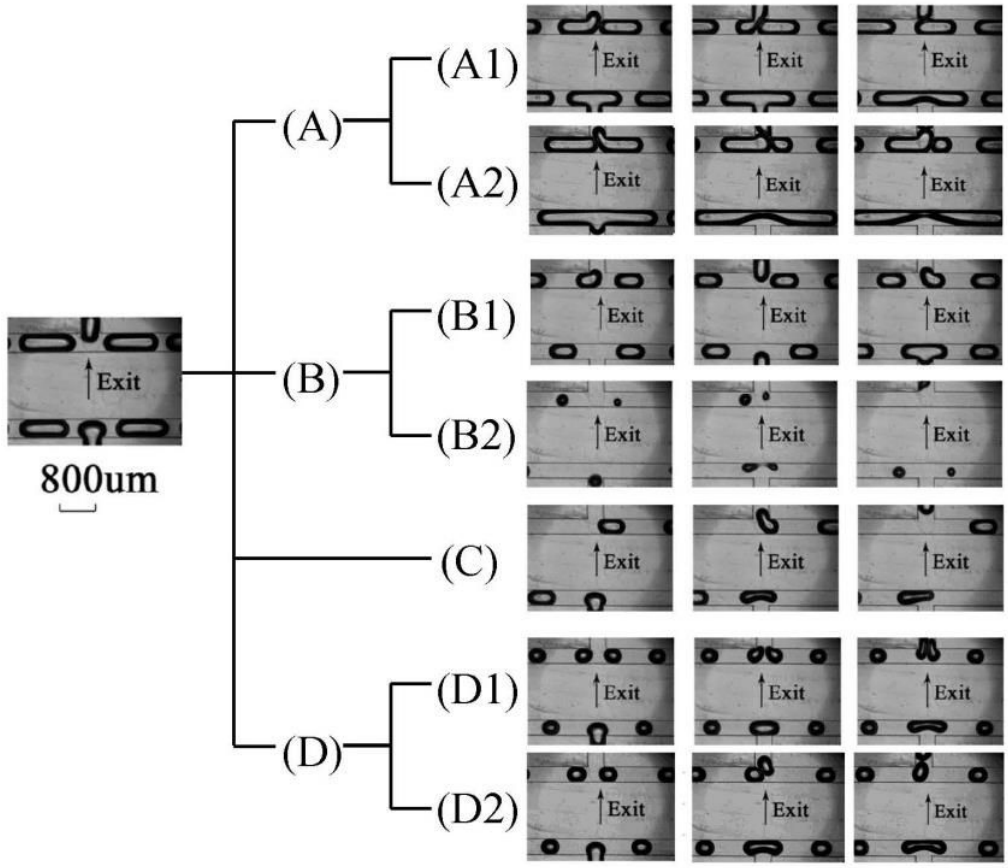

Fig. 4.8 Representative regimes observed for N_2 bubbles move across the T-junction convergence of the loop. (A) bubble pair asymmetrical collision with two sub-regimes (A1) slipping, (A2) splitting; (B) bubble pair staggered flow with two sub-regimes (B1) non-collision of uniform daughter bubbles, (B2) non collision of non-uniform daughter bubbles; (C) single bubble flow; (D) Dynamic transformation flow with two sub-regimes (D1) symmetrical collision of bubble pairs, (D2) asymmetrical collision of bubble pairs.

Fig. 4.9 shows the flow regime diagram for bubbles at the T-junction convergence in SDS solutions (0.24% w/w), where gas flow rate Q_G and liquid flow rate Q_L are chosen as vertical axis and horizontal axis, respectively. In the present experiments the gas flow rate is spanned between 0.44 mL/min and 4.2 mL/min, and the liquid flow rate is between 0.3 mL/min and 10 mL/min. As shown in Fig. 4.9, the bubble behaviors depend dramatically on both the gas flow rate and liquid flow rate. When the gas flow rate and liquid flow rate are less than 1.0 mL/min and 5.0 mL/min, respectively, dynamic transformation flow occurs. Single bubble flow presents in the gas flow rate ranges from 0.44 mL/min to 1 mL/min and the liquid flow rate from1.6

mL/min to 3.6 mL/min. Bubble pair asymmetrical collision exhibits at a relatively low liquid flow rate over the entire range of gas flow rate, whereas the bubble pair staggered flow occurs at higher liquid flow rate. Asymmetrical collision and staggered flow are the most primary two flow regimes for bubbles at the T-junction convergence, and could lead to obviously different feedback effects on the bubble breakup at upstream T-junction divergence of the loop. Therefore, these two behaviors are most concerned in this work.

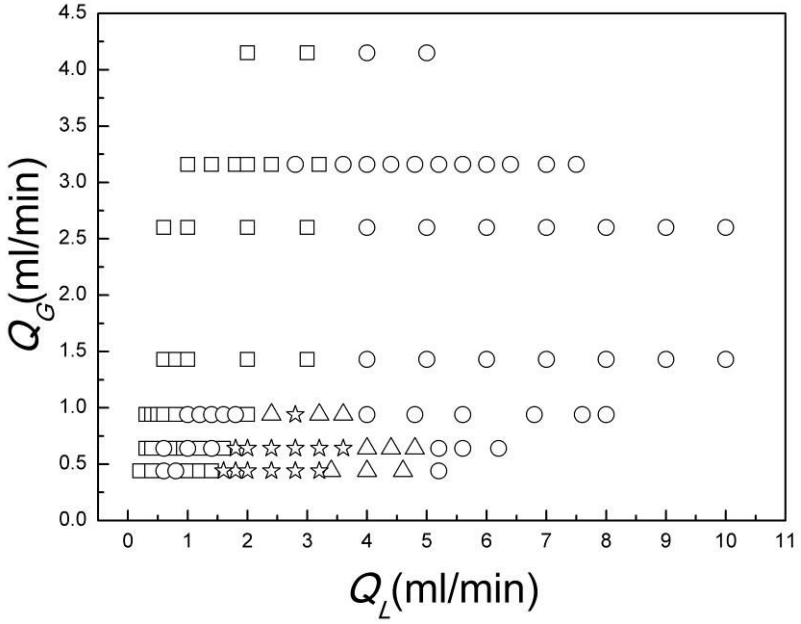

Fig. 4.9 Operating diagram of droplet behaviours by using the gas flow rate Q_G and liquid flow rate Q_L as coordinates. Symbols denote the bubble behaviours at the T-junction convergence: (□) bubble pair asymmetrical collision, (○) bubble pair staggered flow, (△) Dynamic transformation flow, (☆) single bubble flow.

4.2.2.2 Degree of asymmetrical breakup of mother bubbles at the T-junction divergence

To quantify the feedback effect of bubble pair behaviours at the T-junction convergence on the T-junction divergence of the loop, we use the absolute value of the length difference between two daughter bubbles $|L_1 - L_2|$ to express the asymmetry degree of the mother bubble breakup. The dimensionless of the absolute value of length difference between two daughter bubbles $|(L_1 - L_2)/W_c|$ was plotted against

the dimensionless of the summation of two daughter bubbles $(L_1 + L_2)/W_c$, here W_c is the channel width. It is manifested from Fig. 4.10 that the non-collision region will transform to collision region as the value of $(L_1 + L_2)/W_c$ increases. This results accords with the operating diagram (Fig. 4.9) because the value of $(L_1 + L_2)/W_c$ is dependent apparently on the flow rate of gas/liquid flow rate.

Two distinct domains in non-collision regime were demonstrated in Fig. 4.10: the asymmetry degree $|(L_1 - L_2)/W_c|$ decreased remarkably with the increase of $(L_1 + L_2)/W_c$ at first, and then leveled off at a low degree as the size of bubble increased until bubble collision happened. In the collision region, the variation trend of the asymmetry degree is different. The asymmetry degree varied from rising at first to latterly moderate decreasing with fluctuation. These results arouse our curiosity and research interests to seek the mechanism of the feedback effects of the two bubble behaviors at the T-junction convergence on the bubble breakup at the T-junction divergence of the loop.

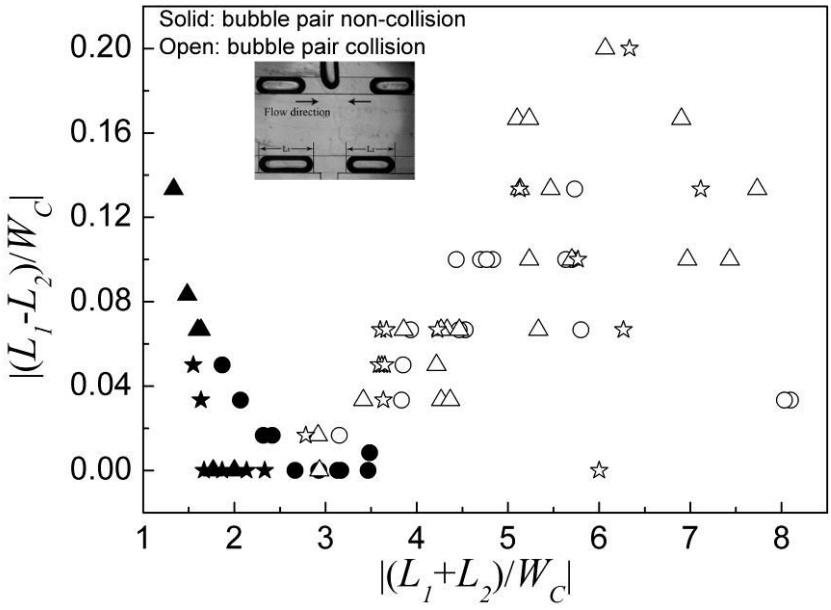

Fig. 4.10 Dependence of the asymmetry degree of the bubble breakup at the T-junction divergence on the bubble length. (○,●) Q_G = 3.16 ml/min, (△ ,▲) Q_G = 2.6 ml/min, (☆,★) Q_G = 1.43 ml/min, open symbol: bubble pair asymmetrical collision; solid symbol: bubble pair staggered flow. The inset shows the length L_1, L_2 of the two daughter bubbles.

4.2.2.3 Feedback of asymmetrical collision of bubble pair at the T-junction divergence

Fig. 4.11 illustrates an example of the temporal evolution of the asymmetric breakup of the mother bubble at the T-junction divergence under the influence of bubble pair asymmetrical collision at the T-junction convergence. The origin of time is taken when the mother bubble reaches the entrance of the loop. When take bubble behaviors at exit into consideration, the whole process of bubbles asymmetric breakup can be described as follows: (1) the first section is from t = 0ms to t = 6ms, a mother bubble penetrates into the loop from the inlet channel and the front cap begins to expand in both radial and axial, until the cap reaches the upper wall; (2) the second section is from t = 6 ms to t = 12 ms, the bubble come through one-dimensional axial symmetric expansion to two downstream branch; (3) the third section is from t = 12 ms to t = 30 ms. The daughter bubble in the left branch reaches the exit first and then slips through the another one in the right branch which is almost motionless during this time. Afterward the one-dimensional axial expansion of the mother bubble at the entrance becomes asymmetric, it is obvious that the part in the left branch is bigger than that in the right part; (4) the fourth section is from t = 30 ms to t = 45 ms. The daughter bubble in the right branch passes the exit and during this time the mother bubble breaks up into two new daughter bubbles.

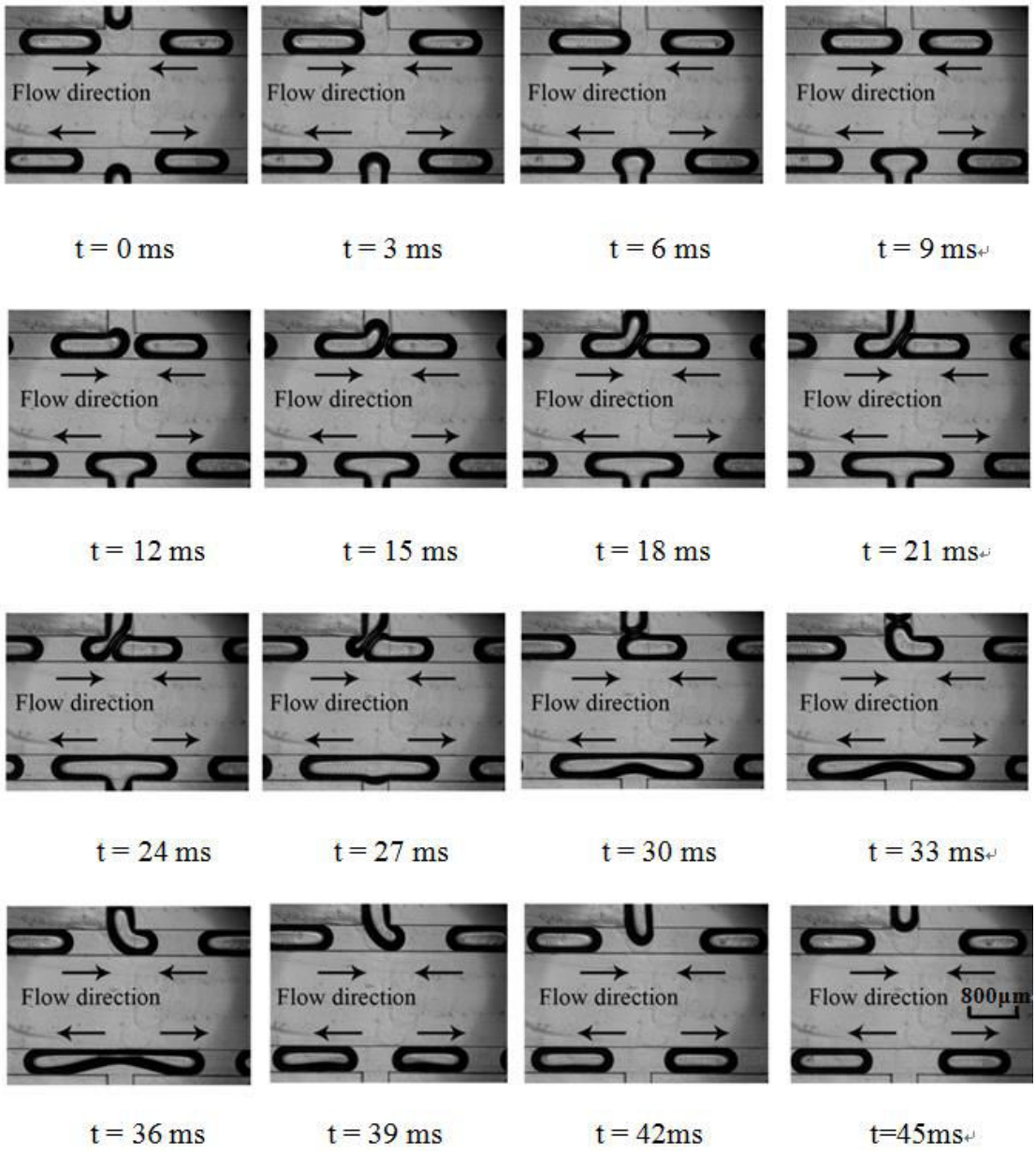

Fig. 4.11 Temporal evolution of asymmetric breakup of bubbles at the T-junction divergence. Q_G = 0.4 ml/min.

The dynamical evolution processes of bubble breakup are quantified by measuring several parameters as sketched in Fig. 4.12(a) and (b). Fig. 4.12(a) and (b) show the penetration and breakup process of a mother bubble, respectively. These two processes determine the length difference between two daughter bubbles. The increased lengths of the breaking bubble in downstream branches are denoted as ΔX_1 and ΔX_2, the subscript 1, 2 represent left branch and right branch respectively. The increased length of the breaking bubble is normalized by the microchannel width W_c. The time is normalized by the characteristic residence time within the T-junction

divergence, $t_c = W_c/U$, where $U = (Q_G + Q_L)/W_c^2$ is the average two phase flow speed in the main channel. As shown in Fig. 4.12c, at first, the dimensionless increased length $\Delta X_1/W_c$, $\Delta X_2/W_c$ increased linearly with the dimensionless time Ut/W_c and the value of $\Delta X_1/W_c$ and $\Delta X_2/W_c$ almost equaled to each other. Correspond to Fig. 4.11 (t = 0 ms to t = 9 ms) during this time, the radial and axial expanding process of the front cap evolved into axial expanding and there is no bubble blocked. Then the dimensionless increased length approach to a constant value for a period of time and $\Delta X_1/W_c$ almost equaled to $\Delta X_2/W_c$. After then, $\Delta X_1/W_c$ exceeded $\Delta X_2/W_c$, the difference between $\Delta X_1/W_c$ and $\Delta X_2/W_c$ appeared. During this time referring to Fig. 4.11 (t = 12 ms to t = 30 ms) we found the exit was occupied by the daughter bubble coming from the left branch and the daughter bubble in the right-hand was blocked by the left one. This process went on until the left daughter bubble drove away from the exit. Finally, the penetration section ended. Then the value of $\Delta X_2/W_c$ exceeded $\Delta X_1/W_c$ as the daughter bubble in the right side flowing away from the exit. When there was no bubble at the T-junction convergence, $\Delta X_1/W_c$ and $\Delta X_2/W_c$ reached the same level again (t = 33 ms to t = 45 ms in Fig. 4.11). Compared to the penetration period, the breakup section is short. Accordingly the breakup process of the mother bubble is asymmetric. The above-mentioned results indicated that the different states (moving or being blocked) of daughter bubbles at the T-junction exit have different effects on flow fields in the branches and on the breakup of the mother bubble.

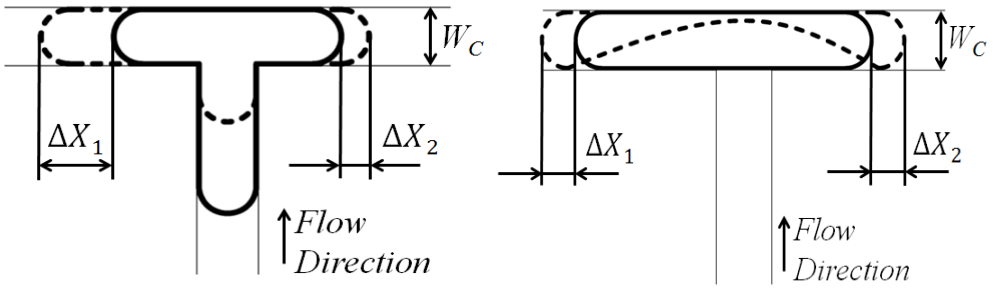

(a) (b)

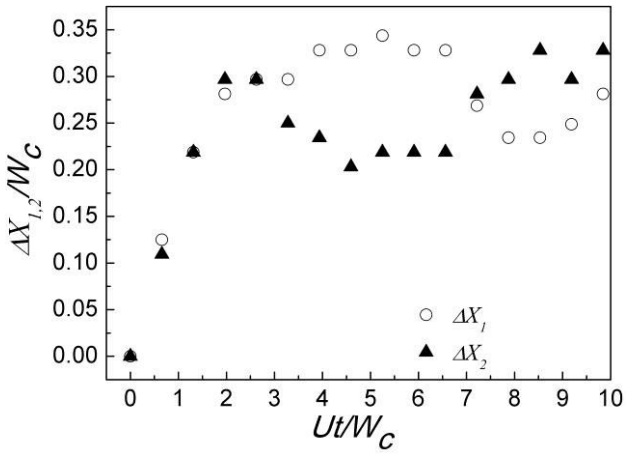

(c)

Fig. 4.12 (a)-(b) Sketch of the asymmetric breakup of bubbles at the T-junction divergence and definition of the two parameters used to characterize the evolution of asymmetric breakup of bubble: (a) the penetration process; (b) the breakup process. (c) The increased length of breaking bubble $\Delta X_{1,2}$ in downstream as a function of Ut/W_c (the subscript 1, 2 represent left and right branches respectively).

To illustrate the mechanism leading to the difference between $\Delta X_1/W_c$ and $\Delta X_2/W_c$, it is needful to understand the Taylor flow behaviour in square cross-section microchannel. In the experiment, a straight microchannel is used for obtaining necessary dynamical information.The Taylor flow is quantified by measuring the length of the bubble and the bubble speed. The bubble length is normalized by the channel width W_c and the bubble speed is normalized by the average two phase flow speed U, as shown in Fig. 4.13. As can be seen from Fig. 4.13a, in low average two phase flow U, the speed of the bubble in SDS solution with critical colloid concentration is less somewhat than U, and then the bubble speed approaches gradually the superficial speed U with its increase. Fuerstman *et al*. also reported similar phenomena [53]. As shown in Fig. 4.13b, when the dimensionless bubble length is relatively small, the dimensionless bubble speed dramatically decreases with the increase of dimensionless bubble length. Subsequently, the dimensionless speed U_b/U decreases slightly.

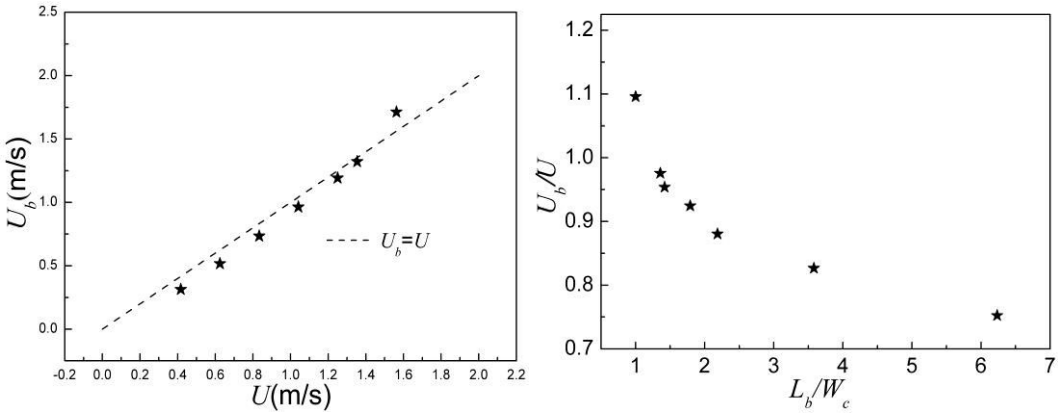

(a) (b)

Fig. 4.13 (a) Plot of the velocity of the bubbles versus the superficial velocity in the straight channel. (b) The dimensionless bubble velocity as a function of the dimensionless bubble length. Liquid phase: SDS 0.24%.

When the dimensionless bubble length is less than one, the value of dimensionless bubble speed is larger than one. The other way round, the dimensionless bubble speed is less than one, and under this circumstance, the liquid phase flows more rapidly than the bubble, thus a portion of liquid flows through the four gutters (the areas bounded by the curved body of the bubble and the corners of the channel as shown in Fig. 4.14b). When the bubbles are small enough and are not confined by walls of the channel, the liquid phase flows much slower than the bubble. This phenomenon has also been reported by Luo *et al.* [171], and can be understood by taking the velocity profile of Poiseuille flow into consideration. When the bubbles are small, they flow downstream in the center of the channel, where the speed approaches twice the average two phase flow speed [88]. While the bubble is confined by the channel, the dynamic resistance of the bubble is larger than the liquid phase in the same length.

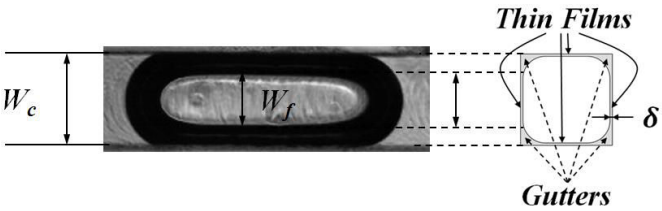

(a) (b)

Fig. 4.14 (a) Scheme for the determination of W_f in square microchannel, W_c = 400 μm. (b) Liquid film shape in square microchannel at low capillary number *Ca* with non-circle bubble.

Obviously the difference of ΔX reflects the difference of total two phase flow rates between two branches in downstream channels. Eq. (4-1) correlates the volumetric rate of flow Q between two given points in a channel, the difference in pressure between those two points ΔP and the fluidic resistance R.

$$\Delta P=QR \tag{4-1}$$

The pressure drop in the two branches is the same at all time, because the two branches start from the same entrance and recombine at the same exit.

In each channel, the law of conservation of mass leads to the following relation:

$$Q_G+Q_L=UA_c=U_bA_b+U_gA_g \tag{4-2}$$

$$Q_g=U_gA_g \tag{4-3}$$

Where Q_G and Q_L are the volumetric flow rates of the gas and the liquid phase respectively and Q_g is the volumetric flow rates in gutters. A_c, A_b, A_g are the cross-sectional area of the microchannel, the bubble and the gutter respectively. U_b and U_g are the velocities of the bubble and the liquid in gutter. We assume the liquid flowing through a thin film is negligible in the presence of gutters (Ransohoff and Radke 1988).

In our experiment, capillary number $Ca=\mu_l U_b/\sigma$ is less than 0.01 under bubble pair collision circumstance. Here μ_l is the viscosity of the liquid phase, σ is the surface tension. As shown in Fig.4.14b the cross-section of the bubble geometry is non-circle. The bubble surface is curved in the corner and becomes flat far away from the corner at low $Ca < 0.04$ [172] and the value of δ/W_c is about 0.02, here δ is the thickness of liquid film between bubble surface and microchannel wall. In the bubble collision scope, the width of liquid film (Fig.4.14a) $W_f \approx 0.48\, W_c$ is nearly unchanged. According to these, we calculated that the value of A_b/A_c is about 0.9. Fig. 4.13b distinctly shows that the value of U_b/U is between 0.825 and 0.950. By substituting these two values into Eq. (4-2), it could be found Q_g does not exceed 0.2575 (Q_G+Q_L). The value of 0.2575 is close to 0.24 measured during the formation

of long bubbles by micro-Particle Image Velocimetry (μ-PIV) system [54], in consideration of that the value could range from 0 (when the speed of bubble equal to the speed of average two phase flow) to 1 (when the bubble was totally blocked, the speed of bubble equal to 0). And the difference between 0.2575 and 0.24 is probably caused by different cross-sections of microchannels employed (square *vs*. rectangular) [54, 172]. It means that the bulk of liquid phase follows with the bubble synchronously, and only a small portion of liquid flows through the gutters. At critical micelle concentration (0.24% w/w) of the SDS solution, the liquid preferentially flows through the four gutters rather than the thin films (Fig. 4.14b), and the pressure drop in channel is dominated by the total bubble length. A straightforward derivation demonstrates that the pressure drop across gutter ΔP_g is the main part of the pressure drop across bubble ΔP_b.

According to Eq. (1) it is easy to show that

$$\Delta P_g = Q_g R_g \tag{4-4}$$

Here R_g denotes hydrodynamic resistance of gutter.

The pressure drop ΔP_g is relative large, compared to that in liquid slugs of the same length at the critical micelle concentration [169] and Q_g is small compared to (Q_G+Q_L), so R_g is larger compared to the resistance of liquid flow in the microchannel. Once a daughter bubble is hold up by the other at the exit, the liquid phase has no other choice but flowing through the gutters, thus, Q_g increases remarkably. As a result, ΔP_g also increases significantly. To balance the pressure drop, the flow rate of the branch in which bubble is hold up has to decrease, finally, leading to a remarkable difference of the dimensionless increased length between $\Delta X_1/W_c$ and $\Delta X_2/W_c$.

It is worth noting that the fluctuation of $|(L_1 - L_2)/W_c|$ in Fig. 4.10, stems probably from the small fluctuation of timing difference between two daughter bubbles flowing

away from the exit and the mother bubble penetrating to the loop. Under some circumstances, the daughter bubbles reached the exit before the mother bubble's penetration. So when one of the daughter bubbles named 'A' passing the exit first, the mother bubble's penetration process tilted towards the branch with bubble 'A'. The other daughter bubble named 'B' from the opposite side passing the exit next will affect the rest of penetration part. And during this time, the mother bubble's penetration process tilted towards the branch with bubble 'B'. Both of the two daughter bubbles affected the breakup of the mother bubble at the T-junction divergence, so the influences of the two bubbles offset each other. As a result, the sizes of new daughter bubbles are approximate. Conversely, the mother bubble penetrated into the loop before the daughter bubbles reaching the exit. Under this circumstance (Fig. 4.11), the daughter bubble reaching the exit first would affect the penetration of the mother bubble at the T-junction divergence while the other bubble of the bubble pair hardly affected the penetration. As a result, the sizes of new daughter bubbles are difference.

4.2.2.4 Feedback of staggered flow of bubble pair at T-junction divergence

As can be seen from Fig. 4.10, the staggered flow region could be divided into two distinct parts: (1) $\varphi \leq 1.5\%$, where $\varphi = |(L_1 - L_2)/(L_1+L_2)| \times 100\%$, (2) $\varphi > 1.5\%$. It is obvious that when $\varphi \leq 1.5\%$, the exit feedback effect of bubbles in the T-junction convergence on divergence is negligible.

Fig. 4.15 shows the evolution sequence of the periodic mother bubble breakup under no occurrence of collision. The process of mother bubble breakup can be divided into three sections: (1) from t = 0 ms to t = 6 ms the expanding of the mother bubble in the radial and axial direction; (2) from t = 6 ms to t = 10 ms the symmetric expanding of mother in the axial direction and the daughter bubble in the right branch driving away from the exit; (3) from t = 10 ms to t = 22 ms the mother bubble broken up into two new daughter bubbles, and during this time the daughter bubble in the left branch passed the exit . During the entire process, the daughter bubbles passed the exit one by one without collision.

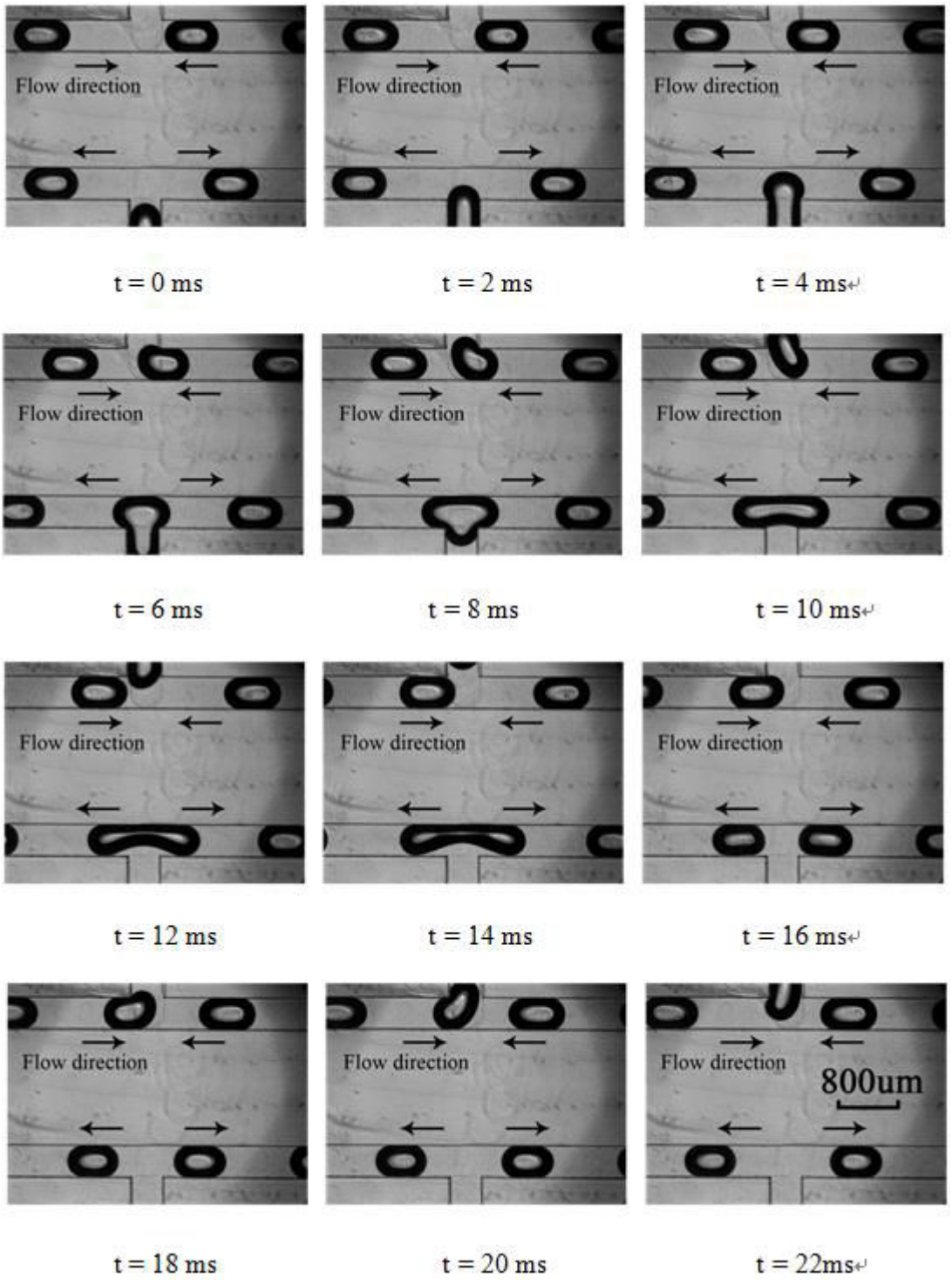

Fig. 4.15 Temporal evolution of symmetric breakup of bubbles at the T-junction divergence. Q_G = 0.94 ml/min, Q_L = 1.4 ml/min.

The quantitative evolution of the breakup of the mother bubble is presented in Fig. 4.16. The parameters are the same as defined in Fig. 4.12b. The increased length of the breaking bubble ΔX and time t are normalized by the W_c, $t_c = W_c / U$ respectively.

As shown in Fig. 4.16, the dimensionless increased length $\Delta X_1/W_c$, $\Delta X_2/W_c$ increased linearly with dimensionless time and their increment is approximate. Referring to Fig. 4.15 (t = 0 ms to t = 6 ms), the radial and axial expanding process of the front cap evolved into axial expanding and there was no bubble passing the exit. Subsequently, both $\Delta X_1/W_c$ and $\Delta X_2/W_c$ decreased moderately, but $\Delta X_2/W_c$ exceeded $\Delta X_1/W_c$ slightly. Corresponding to Fig. 4.15 (t = 6 ms to t = 14 ms), in this period, the right daughter bubble passed away from the exit and no collision occurred. Latter on $\Delta X_1/W_c$ exceeded $\Delta X_2/W_c$ at first, and then, $\Delta X_1/W_c$ and $\Delta X_2/W_c$ reached the same level. In contrast to t = 14 ms to t = 22 ms (Fig. 4.15), the daughter bubble in the left branch drove away from the exit. Because there was no collision between the daughter bubbles during the entire process, the difference between $\Delta X_1/W_c$ and $\Delta X_2/W_c$ was small, As a result, the breakup of the mother bubble was symmetric.

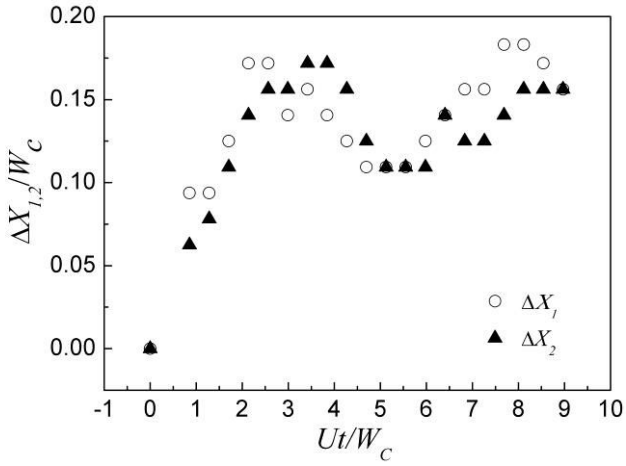

Fig. 4.16 The increased length of breaking bubble in downstream ΔX_1 and ΔX_2, the subscript 1, 2 represent left branch, right branch, respectively, as a function of Ut/W_c.

In this study，the lengths of two daughter bubbles were measured, it could be found that the difference between them is negligible as $\varphi < 1.5\%$. As expected, as long as no collision, bubbles would not be hold up and occupy the entire exit for a long time, thus the resistance and flow rates in two branches would also not be changed markedly. As to why there exists timing difference between the arrivals of the two bubbles at the exit, this is owing to the accumulation effect of slight speed difference (the bubble speed in the left branch is always moderately faster than that in the right branch) between two branches caused by small structured imperfection of

microchannel [166, 173, 174].

As shown in Fig.4.10, there is a critical flow rate Q_c, when the flow rate exceeds the Q_c the structured blemish effects could be strongly amplified [173], which leads to the occurrence of asymmetric breakup as shown in Fig. 4.8(B2). The small bubble flowing through the right branch arrives at the exit earlier than that in the left one, but this does not mean that the continuous phase flow rate in the right branch is larger than that in the left branch，this is because the small bubbles in the right branch usually centralized in the channel center region, as be well known where the flow speed of continuous phase approaches to about twice the average flow speed.

4.3 Conclusions

In this chapter, both uniform and non-uniform magnetic fields were utilized to realize an active control of the droplet breakup of ferrofluid in T-junction. Under the uniform magnetic fields, the area of BTO region is enlarged towards BPO region with a longer time required for the breakup process. The frequency of the breakup processes can be easily adjusted by the applied magnetics force. When the breakup process occurs under the non-uniform magnetic fields, two daughter droplets with different sizes can be formed. The non-uniform magnetic field facilitates the non-breakup of droplets. These results throw new insight into the breakup mechanism and the size control of ferrofluid droplets under an additional and well-controlled external force and could provide a new avenue to explore complex interfacial phenomena at microscale. In the second part, the behaviors of bubbles in the symmetrical loop in a microfluidic device were experimentally investigated by using a high-speed digital camera. Four categories of behaviors such as bubble pair asymmetrical collision, bubble pair staggered flow; single bubble flow and dynamic transformation flow at the T-junction convergence were observed. The feedback effect of bubble collision at the T-junction convergence on the asymmetric breakup of bubbles at the T-junction divergence in the loop was investigated.

Chapter 5 The formation of satellite droplet （bubble）in different micro-device

In chapters 3 and 4, the thinning necks of droplets were always attended by the formation of satellite droplets. This phenomenon is prevalent in the previous works. The generation of satellite droplets leads to the augmentation of system polydispersity, which runs contrary to the original intention of microfluidics. Thus much attention is needed to shed light on the formation mechanism of satellites; whereby researcher could alleviate this phenomenon. Therefore, in this chapter, we studied the satellites formation processes in different microfluidics channels. The first part focuses on the formation of satellite droplet during the thinning of neck filament in microfluidic flow-focusing junction and T-junction. The evolution of the neck thinning process was captured by high-speed camera. Using self-written programs, the evolution of the minimal width, the volume of and the length of neck filament etc. were analyzed to understand the satellite formation process. The second part investigated the morphological developments of the droplets (bubbles) flowing in the downstream straight micro-channel by a high-speed camera. The study is mainly focused on the influences of both the discrete droplet (bubble) size and two-phase average flow velocity on the formation of tip stream which generates substantial number of satellite droplets in the rear of a droplet (bubble).

5.1 Introduction

Emulsion by the dispersion of a liquid into another immiscible one is usually a basic and necessary operation in many industrial applications such as skin care products like shampoo, foods like mayonnaise, drug and chemical analyzing, etc. [2, 91]. Generally, the high shear processes are used to produce emulsions, for instance, highly efficient mixing and agitation. Unfortunately, these traditional processes are often temporarily discontinuous and could lead to a wide droplet size distribution over even three orders of magnitude. The polydispersity of the droplet size will sacrifice the quality of the product and debase the value.

Compared with traditional production equipment, the microfluidic devices with the advantages of the controllability, small size and excellent monodispersity for bubbles and droplets attract much attention [37, 83]. Several basic microfluidic configurations such as T- and Y-junctions, flow-focusing and co-flowing junctions have been applied to produce emulsions [105, 175]. Although microfluidic devices have attained significant improvements, the formation of undesirable satellite droplets could still be frequently observed due to the interface breakup in T-junctions and flow-focusing junctions [91, 170]. Because of the tiny size of these satellite droplets compared to the primary droplet, the polydispersity index of the system would certainly become increased remarkably. These satellites play generally a negative role as they speed up the ageing (Ostwald ripening in particular) and increase the instability of emulsions [91]. It would also pose a threat to the control of release of pharmaceuticals. Moreover, tip stream was also reported in microfluidic systems [91, 94, 95]. The daughter droplets ejecting from the sharp tip usually are three orders of magnitude smaller than the mother droplets, which will also inevitably increase the polydispersity index. Therefore, several studies have been devoted to the formation mechanism of the satellite droplets or the tip stream. Zhao *et al* studied the influence of the interfacial elasticity on the formation of the satellite droplets [176]. They utilized peptide as surfactants to form network in the interface for increasing the elasticity in order to suppress the formation of the satellite droplets. Carrier *et al* studied the formation mechanism and the sizes of satellite droplets in the flow-focusing device [91]. They found that the formation of satellite droplets greatly depends on the flow of continuous phase. There is a critical capillary number Ca= 0.01, below which the size of the satellite droplet remains unchanged, while above that the size would increase until entering the tip stream region. Anna and Mayer also reported the tip stream in flow-focusing device similar to the observations of Carrier *et al*'s. In their experiments, the tip stream could occur only when the bulk surfactant concentration exceeds 0.5 time of the critical micelle concentration and the capillary number locates in a special range. Besides the droplet formation stage, the tip stream was also found in a contracting microchannel [94]. The influence of the wall confinement was comprehensively studied, and the results indicated that the confinement was mainly responsible for the formation of tip stream.

To avoid the polydispersity in microfluidic devices, it is essential to fully understand the tiny droplets' formation mechanism. In this work, we present the experimental

observation of the formation of the satellite droplet during the pinch-off of the neck filament in T-junction and flow-focusing geometry and the experimental observation of the tip stream in the rear part of the droplet flowing in the straight channel and try to gain insight into the formation mechanism in the channel.

5.2 Results and discussion

5.2.1 Formation of satellite droplet due to neck pinch-off

5.2.1.1 Formation of satellite droplet in flow focusing geometry

The evolution of the neck

The droplets are generated in flow-focusing geometry (Fig.2.1a). The whole formation processes are shown in Fig.5.1a. The dispersed phase first expands in the intersection region of the main inlet channel and two side channels (Fig. 5.1a(1)); then the dispersed phase enters the outlet channel and continues to move downstream with the outlet channel partially blocked. During this time the continuous phase thins the dispersed thread in the radial direction and elongates it in the axial direction until the presence of the neck. Subsequently, the neck forms and thins progressively. Finally, the neck pinches off forming a new primary droplet and following closely satellite droplets (Fig. 5.1a(6)).

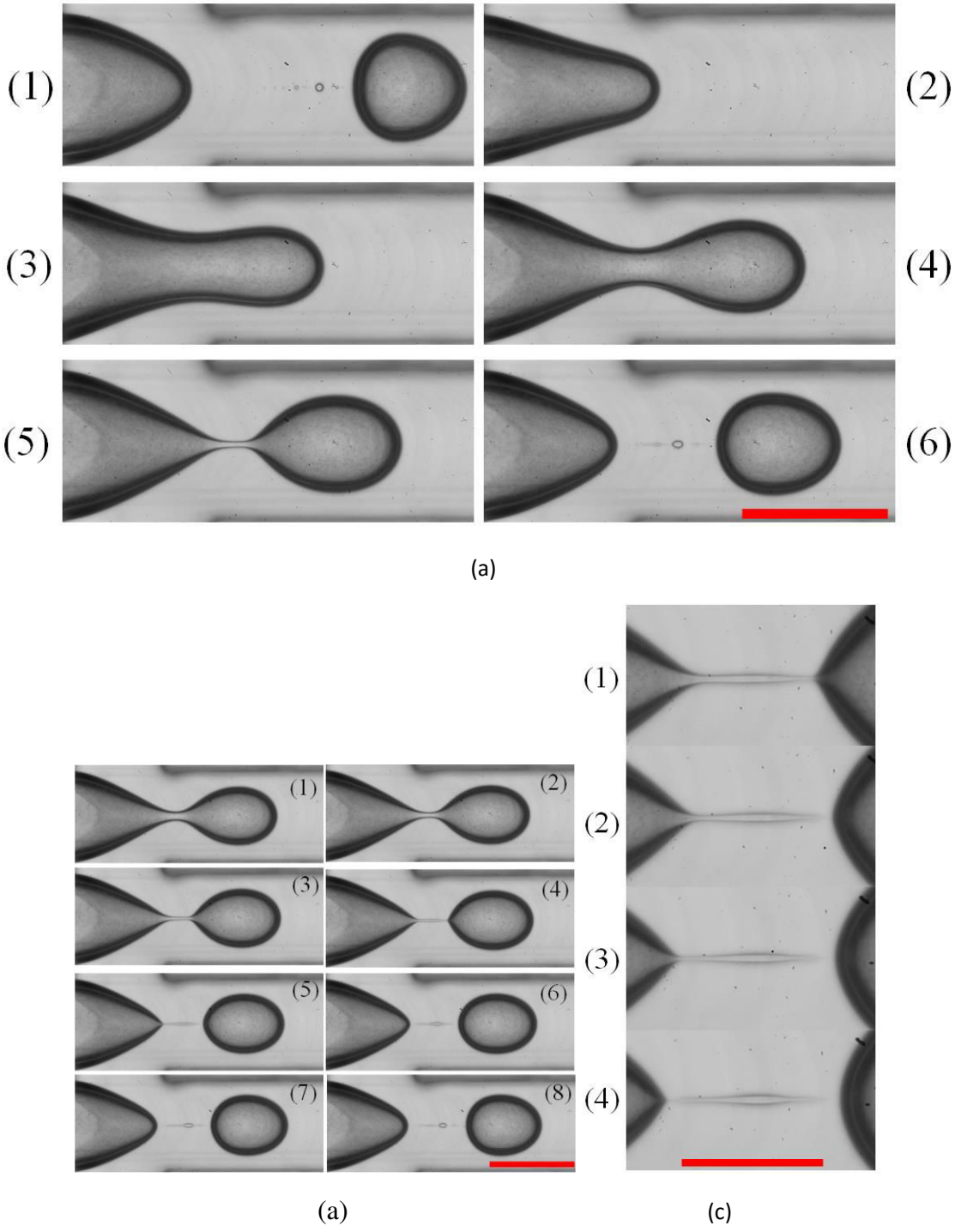

Fig. 5.1. (a) Formation sequence of droplets in flow-focusing geometry (scale bar 400μm) (b) Evolution of the neck in the final pinch-off stage (scale bar 400 μm) (c) the details of the neck filament with time interval 0.1ms (scale bar 160 μm).

Researches concentrate on the thinning dynamics of the neck which determines the formation of satellite droplet. As shown in Fig. 5.1a, before final pinch-off the neck is always reminiscent of a horse saddle and has only one minimal value close to its

middle point. In the next moment, the dispersed phase upstream contract towards the intersection region simultaneously, the new formed droplet moves downstream. Consequently, the neck stretches parallel to the outlet channel forming a quasi-cylindrical thread (Fig. 5.1b(3)). Subsequently, the neck elongates further and its geometry transforms to a spindle shape (Fig. 5.1b(4)). The middle region of the neck is thicker than other part of the neck. Furthermore, the neck will transforms from symmetrical shape (Fig. 5.2d) to asymmetrical one (Fig. 5.1a); namely, the downstream end of the neck is narrower than the upstream end (Fig. 5.1c(1)) and the difference between them increases with the increase of the capillary number in the continuous phase Ca ($Ca = \mu_c U_c/\sigma$), where μ_c, U_c and σ denote the continuous phase superficial velocity the viscosity of the mineral oil and the interfacial tension, respectively. This phenomenon is similar to the observations of Carrier *et al* [91]. Owning to this difference, the first breakup of the neck is invariably close to the new formed droplet (Fig. 5.1c(2), (3)). Finally, the upstream end of the neck detaches from the dispersed phase tongue (Fig. 5.1c(4)) meanwhile the neck transforms into several satellite droplets(Fig. 5.1(7), (8)).

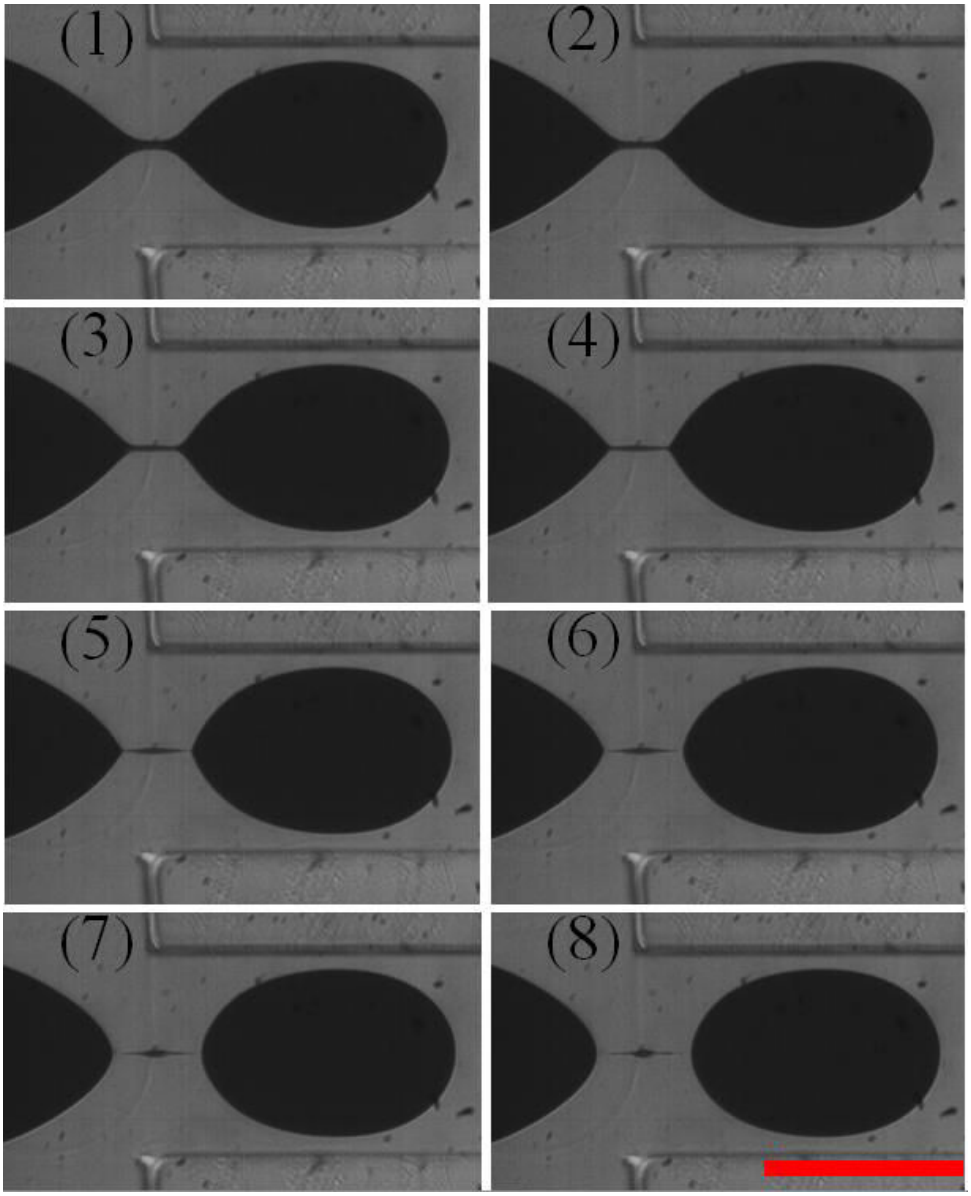

Fig. 5.2. Formation sequence of the ferrofluidic droplet accompanied by satellite droplets in flow-focusing geometry. (scale bar 400μm)

The neck dynamics in flow-focusing geometry

To understand the thinning dynamics that we observe, we demonstrate the temporal evolution of the minimum width of the thinning neck W_n (Fig.5.3a). The thinning process of the neck can be divided into three steps. In the first step, the minimum width of the neck W_n is relatively large. The thinning process is control by the continuous phase and the neck thins slowly [32]. When the minimum width of the neck approaches one hundred micrometer, the capillary pressure P_c due to the interface curvature that scales as σ/W_n determines the thinning process [36, 73, 177]. As a

consequence, W_n decreases rapidly and enters the second stage namely, rapid thinning. Subsequently, the thinning velocity decelerates until the rupture. This result is probably due to the viscous force which is proportional to μ_c/W_n^2 becoming increasingly important as the neck filament thinning and finally balancing the capillary force as W_n decreases continuously. As shown in Fig.3a, the turning point between the second and the last stage locates roughly at 11 micrometer. This value is according with the viscous length scale L_μ ($\mu_c\mu_d/\sigma\rho_d$ = 11.5 micrometer) proposed by Lister and Stone [178]. When the neck is smaller than viscous length, the viscous force becomes dominant. This result also means the capillary pressure is not the predominant driven force in final pinch-off stage. Once entering the third stage, the neck stretches obviously forming a filament thus the narrowest point is no longer in the center of the neck. From Fig.5.1c, we observe that the two ends of the neck evacuate liquid from them growing into two breakup points, while the center of the neck inflates gradually then forms a bead. Thus there are solid symbol and open symbol to denote the upstream (left side) breakup point and downstream (right side) breakup point, respectively. To figure out the reason why the breakup point moves to the two ends of the neck, we track the volume of the neck shown in Fig.5.3b. It is evident that the volume of the neck filament decreases moderately at the start of the third stage, subsequently, remains roughly constant during the time left over. This confirms the viscous force prevent the rapid burst driven by the capillary force. And at the same time the neck filament resists the stretching stress due to the elongation of the filament caused by the detaching droplet downstream and the contracting dispersed phase tongue. Furthermore, the thinning of the neck region is the fastest in the second stage, thus the interface expansion is also the largest there. Consequently, the liquid flowing from the neck and the interface dilatation will work synergistically to reduce the concentration of the surfactants in the neck [179]. Therefore the interface tension at the two ends of the neck which connects respectively the dispersed phase tongue and the new droplet reach the bottom compared with the other part of the neck. As a result, the breakups occur at the two ends of the neck producing satellite droplet.

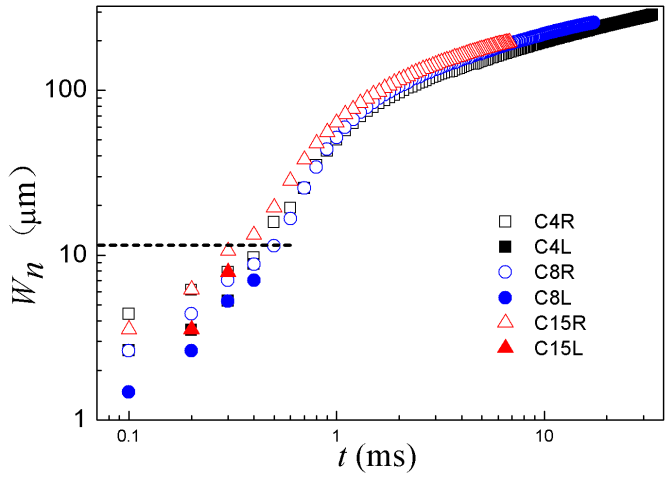

(a)

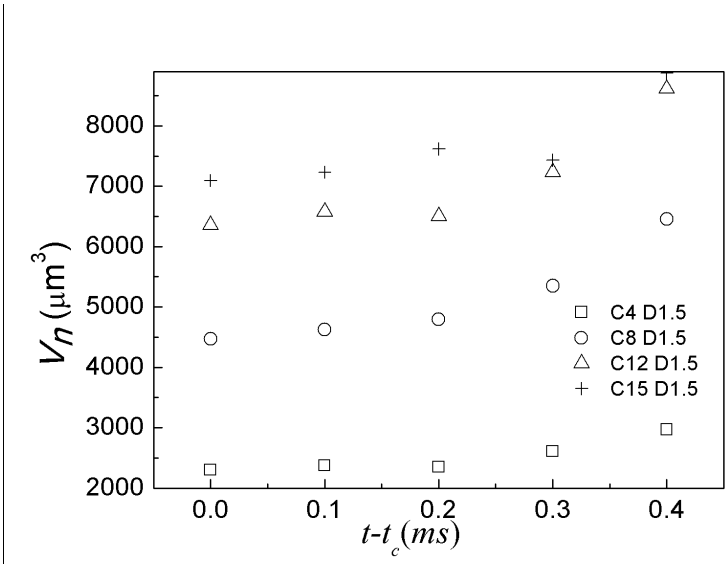

(b)

Fig. 5.3 (a) Evolution of the diameter of the neck of de-ionized water droplets in mineral oil forming flow-focusing junction as the function of the remaining time (b) Evolution of the volume of the neck filament as the function of the remaining time

5.2.2 Formation of satellite droplet in T-junction

The evolution of the neck

As a droplet enters the T-junction whether it will break up or not depends on its size and velocity [77]. Here, our emphasis is on the breakup process in the T-junction of a symmetric loop (Fig.2.1b). The whole breakup is shown in Fig.5.4a. Firstly, a droplet

penetrates into the T-junction (Fig. 5.4a (1)), then it elongates along the wall opposite to the feed channel (Fig. 5.4a (2)). The droplet then stretches gradually with a neck forming in the vicinity of the stagnation point. During this time the two dumbbell-like parts are formed (Fig. 5.4a (3), (4)). At the final stage, a nearly cylindrical filament is formed in between the two droplets segments (Fig. 5.4a (5)), and then give birth to a satellite droplet due to double breakup at the two ends (Fig. 5.4a (6)). In addition we observe the resemble breakup phenomena of a ferrofluidic droplet as shown in Fig.5.5.

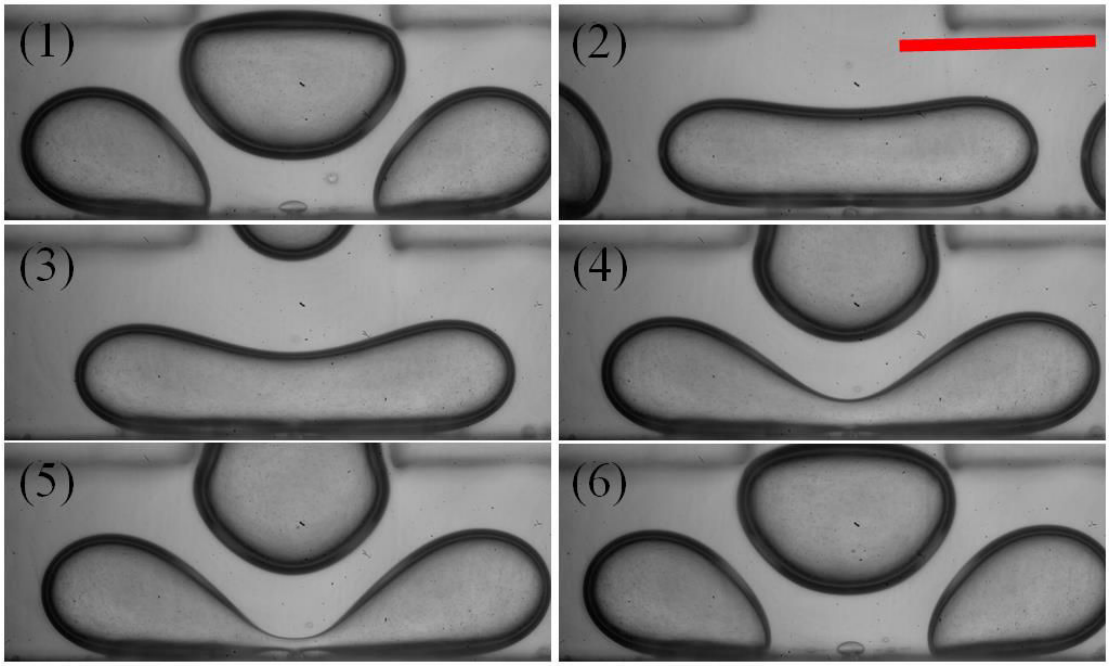

(a)

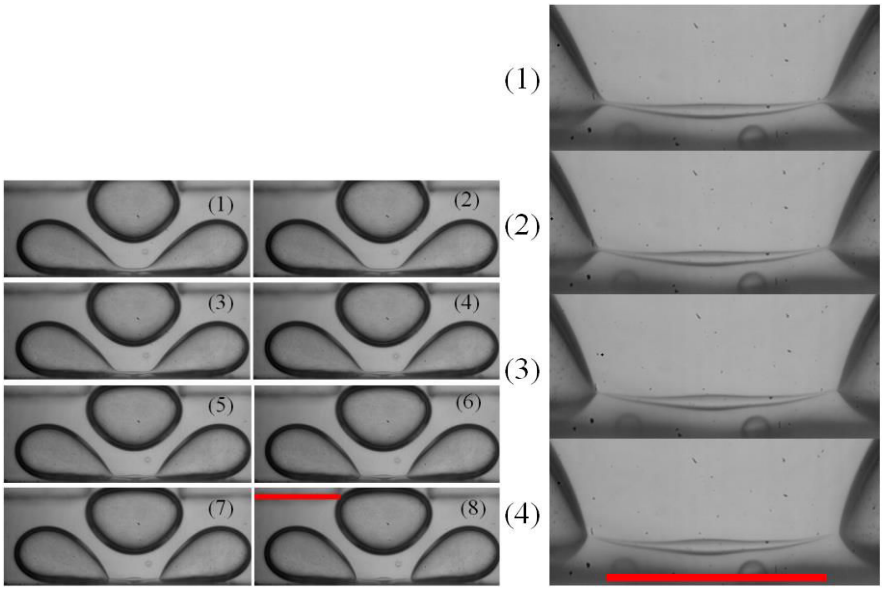

(b) (c)

Fig.5.4. (a) Formation sequence of droplets in T-junction (scale bar 400μm) (b) Evolution of the neck in the final pinch-off stage (scale bar 400μm) (c) the details of the neck filament with time interval 0.1ms (scale bar 200μm).

Similar to the above-mentioned breakup occurring in flow focusing geometry, we still concentrate on the thinning dynamics of the neck which determines the formation of satellite droplet. The thinning process of the neck in T-junction is similar to the thinning process in flow focusing geometry. The neck changes from a horse saddle shape to a quasi-cylindrical shape (Fig. 5.4b(1)). Then the filament stretches along with the wall opposite the feeding channel and still maintains the uniform shape (Fig. 5.4b(2), (3)). In the next moment, the two ends of the neck which attach to the droplet segments start to shrink and a bead begins to form at the filament center (Fig. 5.4b(4), (5)) and (Fig. 5.4c3). The two ends of the neck filament continue to thin until the eventual breakup and the bead detaches (Fig. 5.4b(6), (7), (8)).

Compared with the final pinch-off process in the flow focusing geometry, we find the final pinch-off process in T-junction is symmetric about the axial of the feeding channel (Fig. 5.4c). The breakups occurred simultaneously at the two breakup points. This difference owns to the symmetric shear effect from continuous phase. Furthermore, the size of the neck filament in T-junction is much larger than its counterpart in flow focusing geometry. Here the support from the wall opposite the feeding channel plays a pivotal role in preventing the breakup of the neck. And the neck filament formed close to the stagnation region where the impact from the continuous phase is relatively small. Thus under the same flow rates the size of the satellite droplet is larger in T-junction than that in flow focusing geometry.

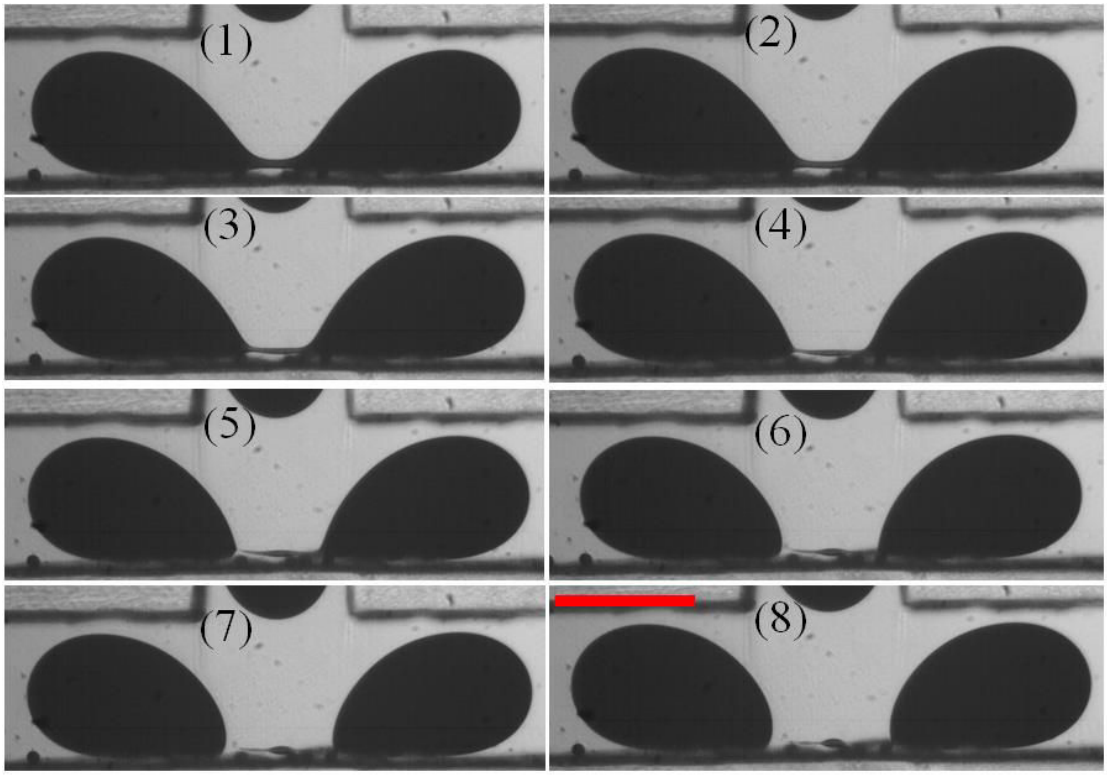

Fig. 5.5. Breakup sequence of the ferrofluidic droplet accompanied by satellite droplets in T-junction (scale bar 400μm).

The neck dynamics in T-junction

Fig.5.6a presents the evolution of the minimum width of the thinning neck W_n as the function of the time before the final rupture. The result is similar to the breakup in flow focusing geometry. The thinning process of the neck undergoes a transition from rapid shrinking to slow contracting. The turning point is about 30 micrometer which is larger than the value in flow focusing geometry. This difference is caused by the geometry difference of the neck in the two junctions. As above mentioned, the neck in the T-junction is more stable. Hence the neck filament is longer in T-junction than that in flow focusing geometry when they own the same width, while the viscosity force is proportional to the filament length. Thus the turning point is larger in T-junction. In the final pinch-off controlled by viscous force, the evolution of the neck volume was recorded as shown in Fig. 5.6b. It is obvious that the volume decreases slightly then stabilizes at a constant value. These results imply that the neck filament pinch-off in T-junction is similar to the breakup in flow focusing geometry.

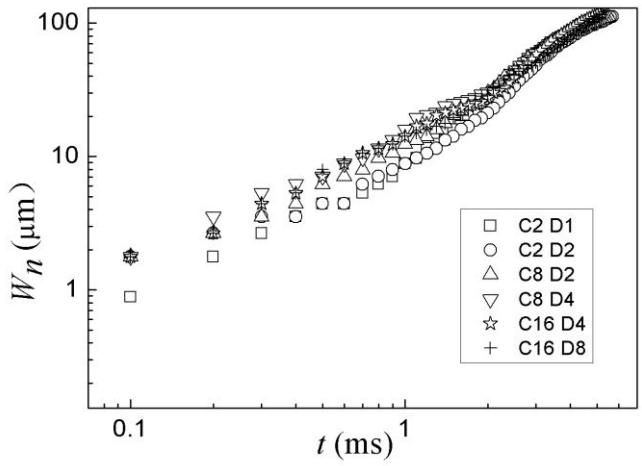

(a)

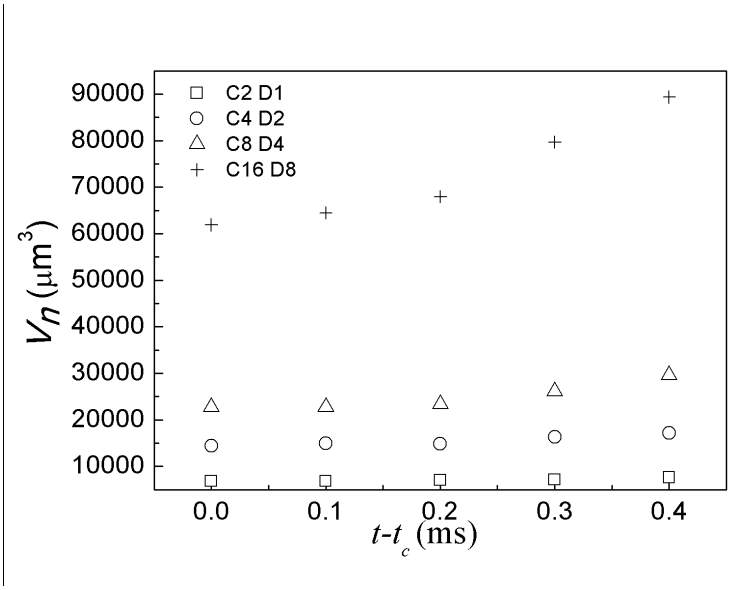

(b)

Fig.5.6 (a) Evolution of the diameter of the neck of deionized water forming in mineral oil in T-junction as the function of the remaining time (b) Evolution of the volume of the neck filament as the function of the remaining time

5.2.3 The total volume of the satellite droplets

In our experiments, the capillary number in the continuous phase Ca ($Ca = \mu_c U_c/\sigma$) (0.039-0.32) has a prominent influence on the total volume of the satellite droplets that is namely the volume of the neck filament when it just detaches. As shown in Fig.5.7, the total volume of the satellite droplets increases almost linearly with the capillary number V_s = K* Ca, here K is a constant. This tendency is relevant to the results reported by Carrier et al.[91]. In addition, the total volume of the satellite

droplet in T-junction is more sensitive to capillary number. This difference probably caused by the different channel structure which affects the pinch-off process.

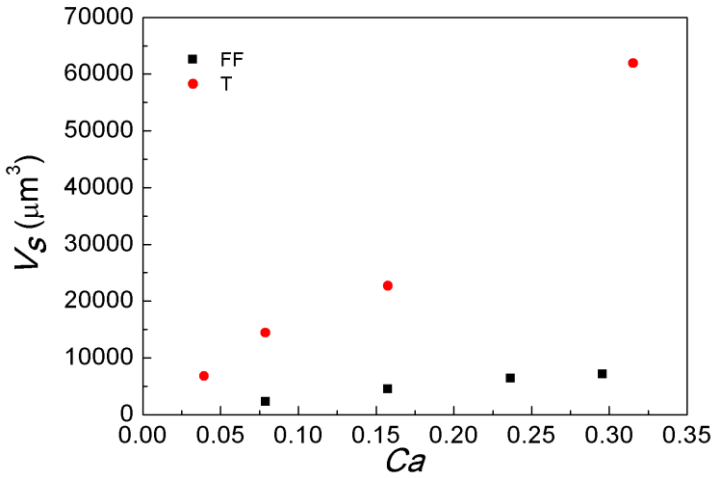

Fig.5.7 Evolution of total volume of satellite droplets of deionized water forming in mineral oil as the function of the capillary number in the continuous phase("FF", "T" denote the flow focusing geometry and T-junction, respectively)

5.2.4 The formation of satellite droplet (bubble) due to tip stream

5.2.4.1 Morphological shape and evolution of the droplet shape

The morphological shape of the droplet flowing in a straight microchannel (Fig.2.1d) was systematically studied under different capillary numbers Ca ($Ca = \mu_l U/\sigma_l$) and droplet sizes L_d, here μ_l denotes the viscosity of the mineral oil. In the experiments, the capillary number Ca was adjusted by altering the two-phase superficial velocity U ($U = (Q_d+Q_c)/W_c^2$). The droplet length L_d was controlled by varying the water/oil flow rates ratio φ ($\varphi = Q_d/Q_c$) and U. Four typical kinds of shape were observed by adjusting the flow rates ratio from φ 0.27 to 1.15 for a given capillary number Ca = 0.55 as shown in Fig. 5.8a: (1) droplet with low arched butt (Fig. 5.8a1), (2)droplet with unapparent dimpling butt (Fig. 5.8a2), (3) droplet with an apparent cupped butt and a tip stream ejecting tiny daughter droplets from one of the two threads (Fig. 5.8a3), (4) droplet with an apparent cupped butt and the tip streams ejecting stably tiny daughter droplets in both of the threads (Fig. 5.8a4). The close-up image of

satellite droplets ejected from mother droplet is shown in Fig. 5.8b. The generated daughter droplets (Fig. 5.8a3, Fig. 5.8a4 and Fig. 5.8b) from the liquid thread due to tip stream with a diameter from 1.6 μm to 24 μm are three orders of magnitude smaller than the primary droplets. These droplet rears with tip stream as shown in Fig. 5.8a3 and Fig. 5.8a4 are similar to that Mulligan and Rothstein have found in liquid drops which are caused by the shear effect stemming from the channel walls [94]. Mietus *et al.* also observed the similar tip stream in the rear part of a drop in unbounded flow, when applying an orthogonal shear force [180]. Previous studies show that a low viscosity ratio between disperse phase and continuous phase and the presence of surfactants are the prerequisites for forming the tip stream [76, 181-183]. Our previous studies and this work have verified these conclusions. In addition, the experimental results indicate that the tip stream formation is a time-dependent process. As shown in Fig. 5.8c, at the initial stage, the droplet detaches from the liquid thread upstream with two convex caps in the head and rear. As the droplet flows downstream, the rear would become blunt due to the shear force stemming from the channel walls. In addition, this shear force will sweep the surfactant to the drop rear when the internal viscosity of the drop is weaker than the viscosity of continuous phase according to previous work by Eggleton et al. As a result, the surfactant concentration in the rear will exceed the equilibrium one with the bulk continuous phase which leads to a great deformation of the drop rear [181]. In this work, the experiment condition was similar to that by Eggleton et al., the surfactant was added and the viscosity of the dispersed droplet is less than that of continuous phase, therefore, the shear force will sweep the surfactant to the droplet rear and the surface tension along the droplet interface would accordingly become non-uniform due to the uneven distribution of the surfactants on the droplet surface. At the annular corner of the droplet rear, the surface tension will reach the lowest value, which could lead to a great deformation and the formation of a crater with a small angle θ (Fig. 5.8c). The interface of the annular corner near the walls would be subjected to much stronger shear force; consequently, the thread was usually torn out from the point near the wall. Finally, tip streams take place in the tips of the threads and eject tiny satellite droplets. Some of these small droplets entering the liquid film between the wall and droplet could be taken as tracing particles to show the velocity distribution in the film as shown in Fig. 5.8d.This simultaneously demonstrates well the shear effect from the walls. Moreover, we found the time required to create a tip stream decreases with the

increase of the capillary number *Ca* and droplet size L_d.

Previous studies have reported that there is a special capillary number range under constant surfactant concentration and viscosity ratio, among which the tip stream could be generated [94, 95, 182]. In the present work, it is obvious that the formation of the tip stream is closely related to the droplet length under constant *Ca* as shown in Fig. 5.8a.

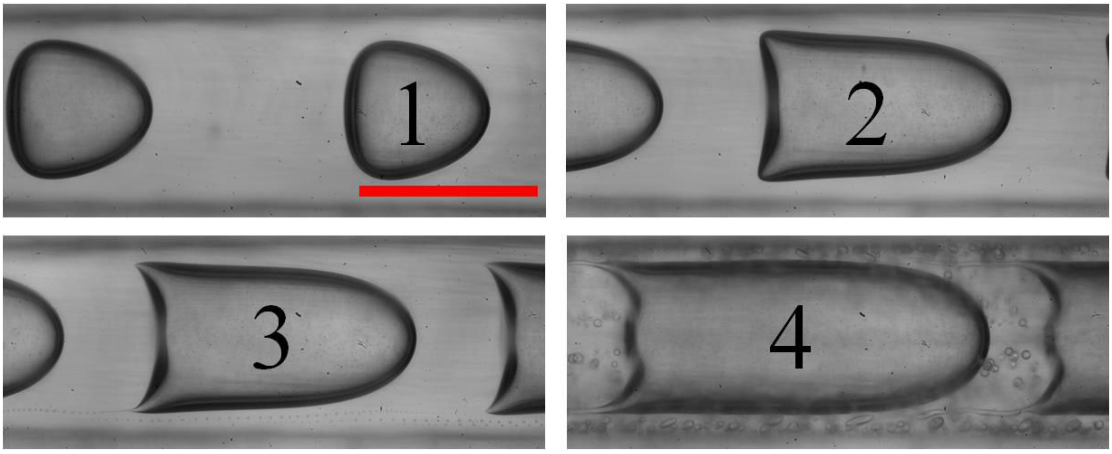

(a)

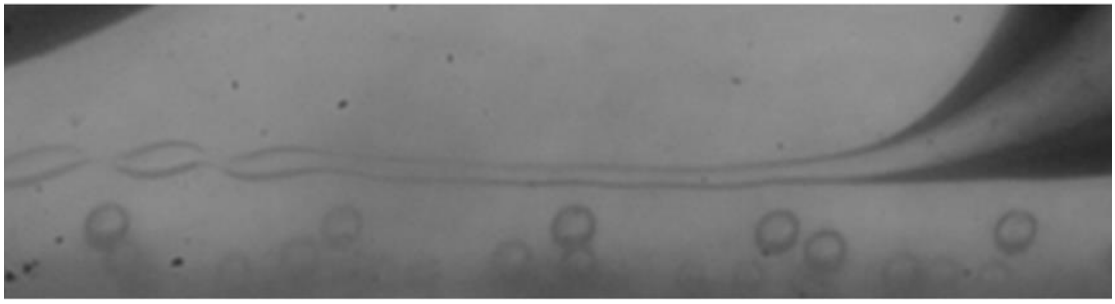

(b)

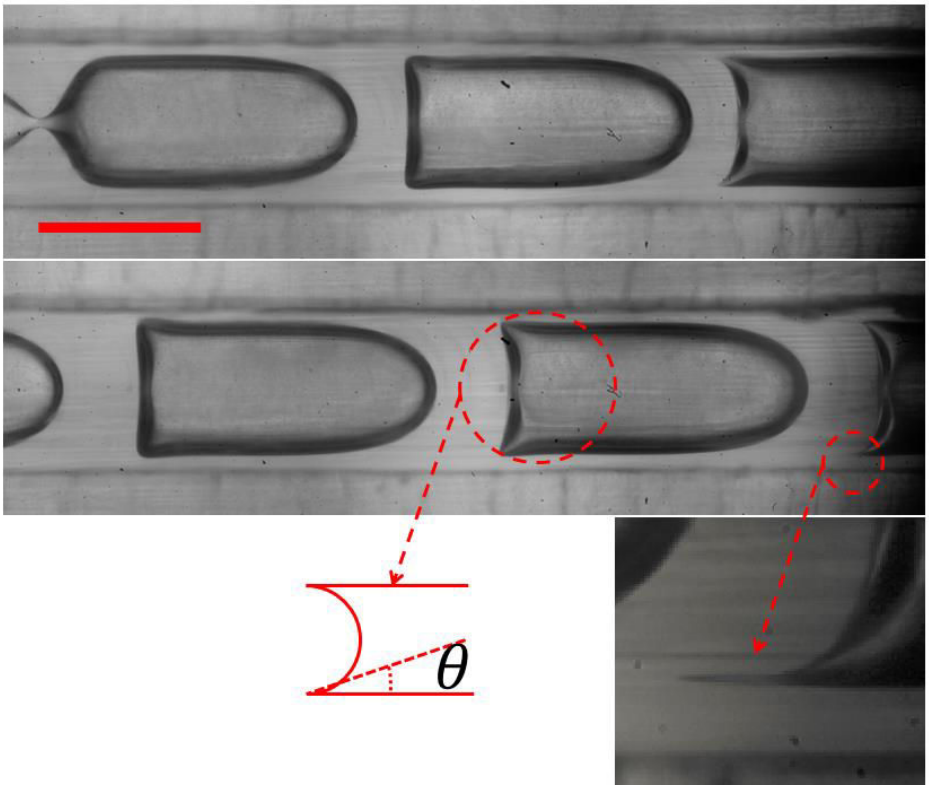

(c)

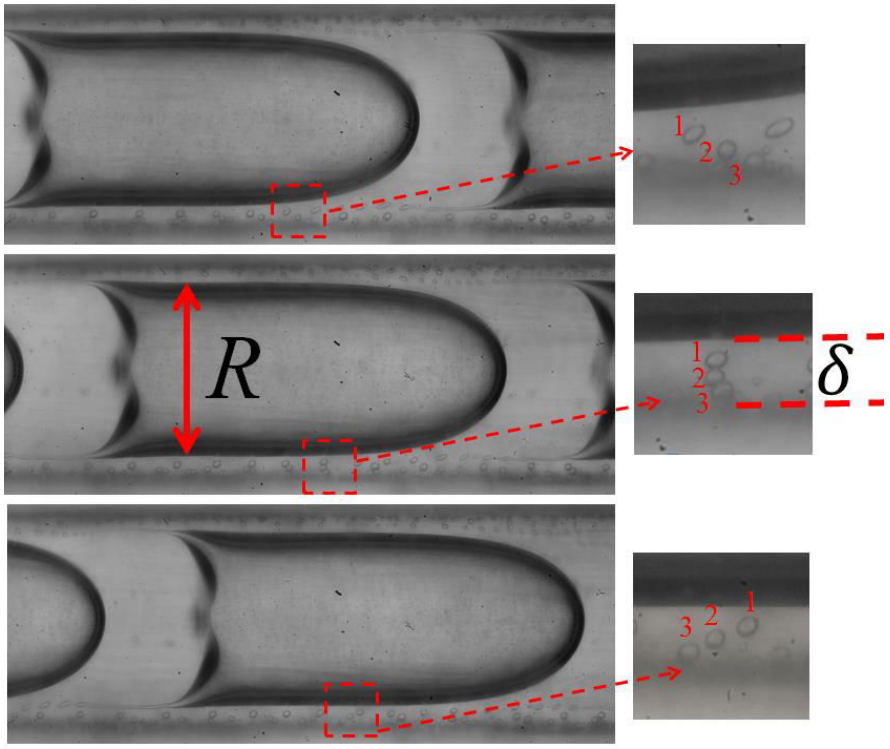

(d)

Fig .5.8 (a)Four kinds of shape were observed by changing the flow rates ratio from φ=0.27 to 1.15 with constant Ca = 0.55: (1) droplet with blunt butt, (2) droplet with concave butt, (3) droplet with a tail stream which ejects transiently small daughter droplets, (4)droplet with two tail streams which eject stably small daughter droplets.

(b) the close-up image of the satellite droplets ejected from mother droplet. (c) Temporal evolution of the droplet shape at Ca = 0.43 φ=1.1 (d) the velocity of the tiny droplets in different positions. The scale bar is of 400μm.

5.2.4.2 Critical dimensionless droplet length

Obviously, the appearance of two threads is a prerequisite for the formation of the tip stream. Therefore, there exists a lowest value for shear force acting on the droplet interface comparable to the surface tension force to deform the droplet and tear out the threads. By balancing the shear force ($\sim L_d R\mu_l U/\delta$) and the surface tension force ($\sim\sigma R$) for a surfactant-free interface, a critical droplet length L_c could be obtained, here R denotes the width of the droplet body，δ represents the liquid film thickness (Fig.5.8d). According to Schwartz *et al.*, δ is proportional to $Ca^{0.5}$ [183]. We could therefore conclude that L_c should scales as $Ca^{-0.5}$. The negative exponent -0.5 means that the critical droplet length decreases with the increase of the Ca, in other words, the larger droplet is more vulnerable to the interface instability.

To stabilize the flow pattern in our cases, appropriate surfactants were added in continuous phase. The stability of the surfactant-laden droplet interface was analyzed. The experimental results of the transition from tip stream region (BR) or unstable regime to non-tip stream (NR) or stable regime in liquid-liquid system are shown in Fig. 5.9a. The dimensionless droplet length L (L=L_d/W_c) is plotted as a function of Ca. The presence of tip stream as shown in Fig. 5.8a3 and Fig. 5.8a4 situates in the region with larger capillary numbers and droplet sizes. While the droplet without tip stream as shown in Fig. 5.8a2 and Fig. 5.8a1 occurs with lower capillary numbers and smaller droplet sizes. As shown in Fig.5.9a, the critical dimensionless droplet length L_c for the generation of tip stream decreases with the increase of the capillary number Ca and obeys the following relationship:

$$L_c = 0.85Ca^{-0.75} \qquad (5\text{-}1)$$

The exponent of this scaling law is less than -0.5. This implies that the occurrence of tip stream in the experimental system need higher shear force superior to surface tension. The reasons of the negative exponent obtained from experimental results and that the increase of L_d in favor of tip stream could be also attributed to following two aspects. Firstly, the droplet length has a remarkable impact on the pressure drop (P_1-

P_3 as shown in Fig.5.10) spanning over the droplet from the rear to head (from left to right in Fig.5.10). According to the studies of Kreutzer *et al*., the pressure drop spanning over the droplets flowing in the straight microchannel is proportional to its length [185]. Therefore, larger droplet length will induce higher pressure drop between the head and rear of the droplet. Provided that the pressure drop inside the droplet caused by internal flow is negligible and the droplet is axisymmetric, the pressure drop between point 1 and point 2 as shown in Fig.4 ($P_1 - P_2$) could be expressed by Laplace' law as ($P_1 - P_2$)= $-\frac{2\sigma}{R_r}$. Here, point 2 is inside of the droplet, R_r denotes the curvature radius of the droplet rear. For a cupped interface as shown in Fig.4 R_r would be negative. Similarly, the pressure drop between point 2 and point 3 ($P_2 - P_3$) could be expressed as ($P_2 - P_3$) = $\frac{2\sigma}{R_h}$, here R_h denotes the curvature radius of droplet head. With the increase of the droplet length, the total pressure drop (P_1- P_3) = $(\frac{2\sigma}{R_h} - \frac{2\sigma}{R_r})$ will increase correspondingly. This increase of pressure drop would be reflected in the curvature difference between the head and the rear of droplet according to the above-mentioned equation. With the increase of the pressure drop ($\frac{2\sigma}{R_h}$ increases but $\frac{2\sigma}{R_r}$ decreases), the curvature of droplet rear decrease gradually. Consequently, the rear of the droplet will become flatter even cupped ($R_r < 0$, as shown in Fig.4), which facilitates the formation of the annular corner and then promotes the generation of the threads as shown in Fig. 2c. Secondly, the size of the droplet also determines the total amount of surfactants on the interface. For a longer droplet, there would be much more surfactant molecules to be adsorbed in the interface due to the larger interfacial area, thus it is easier to bring sufficient surfactant molecules into the turning corner to diminish the surface tension. Therefore, taking these factors into account integrative, the larger droplet size is in favor of tip stream and the negative exponent could be easily understood.

Similarly, a scaling law was also observed the gas-liquid system. As shown in Fig.5.9b, the critical dimensionless bubble length L_c decreases with the increase of the

capillary number *Ca* and conforms to a similar function as in liquid-liquid system:

$$L_c = 0.62Ca^{-0.63} \qquad (5\text{-}2)$$

By comparing these two master curves, it could be found that the generation of the tip stream requires much higher L_c and *Ca* in the liquid-liquid system. The difference between these two master curves might be attributed to the remarkable difference of the viscosity ratio, the density ratio and the surfactants between Liquid-liquid system and gas-liquid system. Previous study has demonstrated that the surface tension gradient is a key factor to generate tip stream [95]. In liquid-liquid system, the concentration of the surfactant is much higher than gas-liquid system; consequently, the surfactants take shorter time to migrate and adsorb to the interface in liquid-liquid system. Therefore, the formation of the surface tension gradient is difficult in such a system. Meanwhile, the surfactant molecule size used in liquid-liquid system is higher than in the gas-liquid system, thus the migration speed of the surfactants along the interface is lower as compared to the gas-liquid system [94], in this case, much higher shear force is needed to produce a surface tension gradient. These factors jointly lead to the difference between the two master curves.

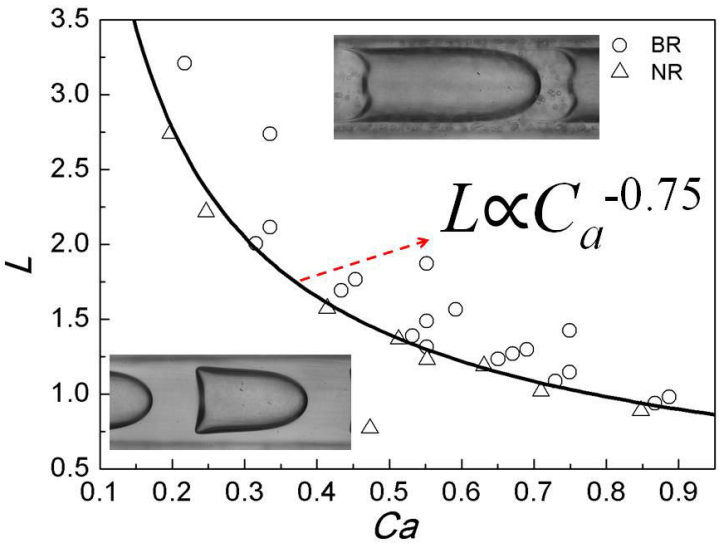

(a)

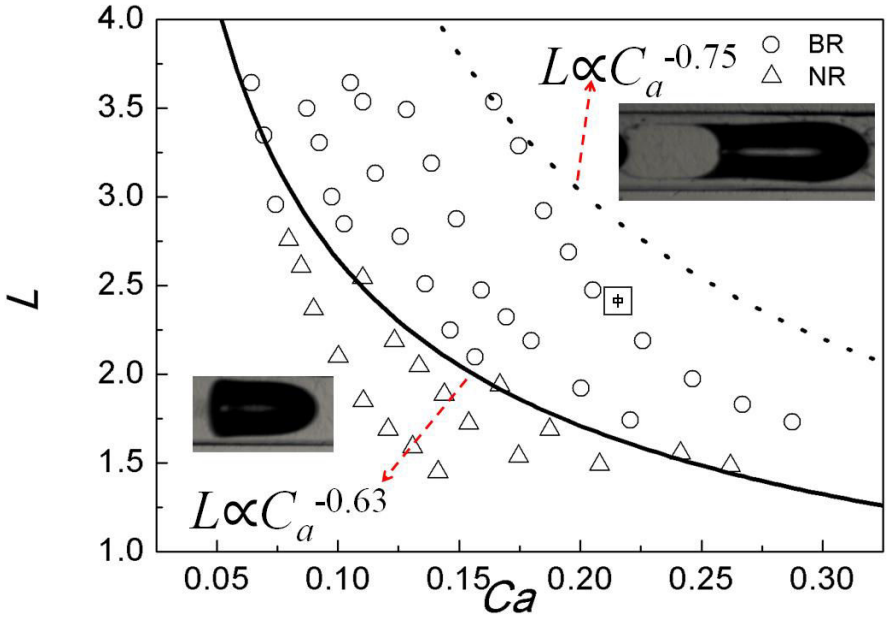

(b)

Fig.5.9 (a) Operating diagram organizing droplet behavior as a function of the capillary number *Ca* and the dimensionless droplet length *L*. The solid line represents the critical dimensionless droplet length for the formation of tip stream in liquid-liquid system. (b) Operating diagram organizing droplet behavior as a function of the capillary number *Ca* and the dimensionless bubble length *L*. The solid line represents the critical dimensionless bubble length for the formation of tip stream in gas-liquid system. The dotted line represents the critical dimensionless droplet length for the formation of tip stream in liquid-liquid system.

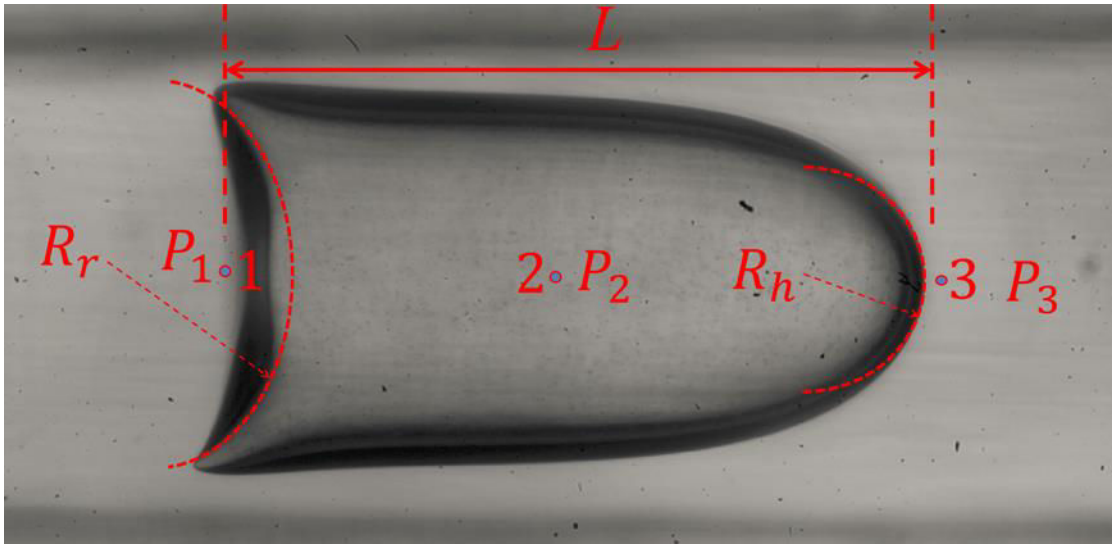

Fig.10 The sketch map of pressure drop spanning over a droplet

5.2.4.3 Maximum length of the tip stream

As shown in Fig.5.8b, the right part of stretched thread near the mother droplet had an almostly constant radius of curvature. Along the thread to the upstream (left side), the thread was perturbed leading to an alternative pinched section and bulging section. This sinusoid-like disturbance was propagated to the left side with increasing amplitude. There exists a maximum dimensionless length of the thread $L_m=L_t/L_d$, beyond which it will decompose into tiny satellite droplets. The breakup of the thread is similar to the decomposition of falling jet caused by Rayleigh-Plateau instability. With the increase of the capillary number *Ca*, the maximum dimensionless length of the tail $L_m=L_t/L_d$ increases sharply at lower capillary region then almost levels off at $Ca = 0.5$ as shown in Fig.5.11. In present experiment, the shear effect brings much more molecules to the thread, decreasing the surface tension. Based on the Rayleigh-Plateau instability, the length of falling jet is proportional to $\sigma^{-0.5}$. This means the decrease of surface tension is in favor of the elongation of the jet. Thus the interfacial tension driving fragmentation could be suppressed and the tail could maintain a longer developing time to increase the length. As the shear force increases, the thread interface becomes saturated with the surfactants; the length of thread accordingly levels off. This relationship is similar to the results obtained by Anna and Mayer (2006). However, the thread diameter would not decrease with the increase of the maximum extent; this is different from their results. The difference is maybe caused by the flow rates of the disperse phase in Anna and Mayer's system. In this work, the tip threads were torn out merely by shear effect. In addition, the type and concentration of surfactants employed in these two diphase systems were different.

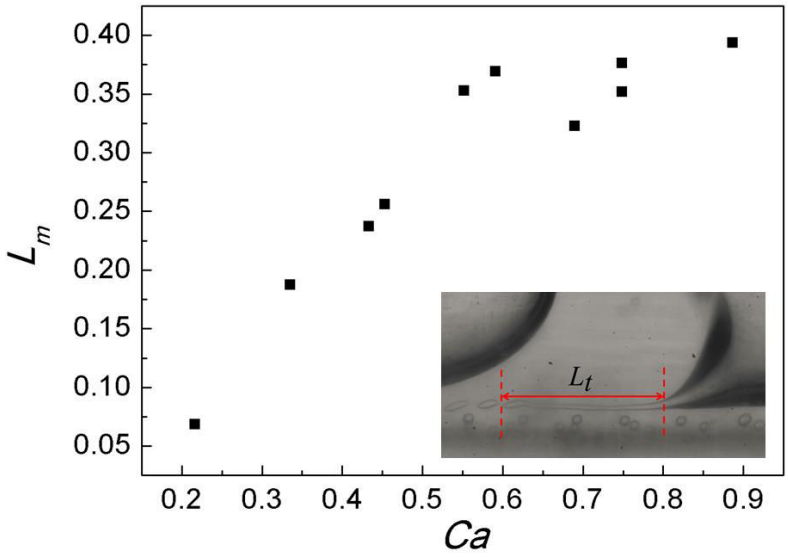

Fig. 5.11 Dimensionless maximum thread length *Lm* as a function of capillary number *Ca* in tip stream region in liquid-liquid system

5.3 Conclusions

In this chapter, the formations of satellite droplet at a microfluidic flow-focusing geometry, T-junction and straight channel were studied, respectively. The satellite droplet generated in first two geometries stems from thinning neck filament; while in the third geometry it derives from the instable tail of droplet (bubble). The first part of this chapter studied the dynamics of stretching and breakup of neck filament at a microfluidic flow-focusing geometry and T-junction. Due to the non-ignorable viscosity of dispersed phase, the thinning of the neck will experience a final low speed stage. The presence of surfactants results in the gradient of surface tension and Marangoni effect. These phenomena coupled together leads to the double breakup of neck filament. Moreover the shape of the neck before rupture is linked to capillary number: symmetric for low capillary numbers and asymmetric otherwise in flow-focusing geometry. In contrast, the shape of the neck before rupture is more symmetric in T-junction. In our experiments, the size of satellite droplets increases with capillary number. The second part studied the tip stream formation in the droplet butt under low viscosity ratio β (0.0018-0.0287) in the presence of surfactants. The experimental observations of two main regions were reported: BR and NR in the power-law function $L \sim Ca^x$ by varying the total flow rates and the flow rate ratio. The generation mechanisms of the tip stream in the liquid-liquid system and gas-liquid system were found to be similar. The length of the tip stream increases with the two

phase superficial velocity and exhibits a maximum at a given capillary number of *Ca* = 0.5. The observations here are vitally important to avoid the occurrence of polydispersity. This study would be also promising for the eventual generation of micrometer-scale droplets in the microfluidic device which could offer new potential applications in biomolecule detection, drug analyzing and functional material synthesis in a near future.

Chapter 6 Droplet (Bubble) coalescence

The coalescence is a ubiquitous phenomenon in nature on a vast range of scales, from cell fusing to the coalescence of gas clouds during star formation. In industry, coalescence occurs in a multitude of processes and still need to be studied. In this chapter we firstly studied the coalescence of bubbles at a microfluidic T-junction convergence by using a high-speed digital camera and the VOF simulation. The microfluidic channels have uniform square cross-section with 400μm wide and 400μm deep. The responses of bubble collisions at the T-junction convergence have been investigated within a wide range of dimensionless bubble size and capillary number *Ca*. Colliding coalescence, squeezing coalescence and non-coalescence were observed at the junction. In the second part, the coalescence of ferrodroplets was investigated under various magnetic fields applied. The emphasis was given to the coalescence between two conic edges of ferrofluid and a consecutive breakup of the newly formed neck. By a high-speed digital camera, it was found that a small amount of ferrofluid pierces the tip surfaces of the approaching cones and forms a liquid bridge or neck with a visible gap in the order of tens of micrometers between the leading edges. The inertia of the ferrofluid originating in magnetic attraction fields becomes the driving force at the initial stage of coalescence instead of capillary force. After the coalescence, a ferrofluid column forms; here a critical magnetic flux density was reported above which the column will collapse and different pinch-off patterns are observed by varying the intensity of magnetic flux density.

6.1 Introduction

6.1.1 Bubble coalescence in microfluidic geometry

Up to now, numerous investigations have been devoted to bubble coalescence inside

or outside the realm of microfludics [100, 186-193]. And the film drainage theory is one of the most widely accepted theories for bubble coalescence. According to this theory, the coalescence process could be divided into three stages: (Ⅰ) the colliding of bubbles, besieging a small amount of continuous phase between two bubbles; (Ⅱ) the thinning of film, continuous phase drains out to a critical value; (Ⅲ) the rupture of film, the film ruptures resulting in coalescence [104]. The contact of bubbles is very important for coalescence. In unbounded flow, the contact of bubbles is induced by the relative motion between bubbles and surrounding fluids, realized by a variety of mechanisms, such as turbulent fluctuations in the continuous phase, the mean-velocity gradients of the flow field, different bubble rise velocities induced by body-forces, bubble contact in an eddy, and wake interactions [104]. The relative motion induced by these mechanisms is lack of active control, so it is hard to guarantee the contact time and the efficiency of coalescence. Recently, Chen et al. studied the effect of confinement on the coalescence of droplets between two parallel plates and found that the confinement facilitates coalescence [194]. As bubbles are usually confined in microchannels, many researchers have utilized microfluidic devices to study coalescence behavior and several active and passive methods have been applied to induce coalescence between bubbles and droplets in such devices. There are three main approaches explored for actively fusing: electric field fusion, magnetic field fusion and local laser heating [109, 110, 195-197]. Although these approaches have been successfully used, these active approaches add additional strict requirements to the devices such as the composition of the fluid, the material of channel walls. Furthermore, the extra electric field, magnetic field and local laser heating may bring interference of reaction, mixing and the physical property of fluids in microchannels. However, those disadvantages could be effectively avoided by using passively control methods.

So far, flow-induced droplet coalescence has been carried out mainly in the expanding and convergence structures [106, 107, 151, 152, 198]. Bremond et al. studied the droplet behaviors in an expanding-constricting chamber and found that droplets could fuse when they were being pulled apart near the contracting outlet [106]. This phenomenon could be attributed to the presence of pointy structures on the gradually remote droplet surfaces. The role of the nipple is similar to the surface waves observed by Zagnoni et al. [196], bringing the interfaces close together and facilitating the formation of liquid

bridge. Consequently, the presence of nipple is expected to facilitate coalescence. Lai et al. theoretically demonstrated the presence of nipple [199]. The coalescence behaviors for bubbles and droplets in convergence junctions have also been investigated recently [100, 152]. Christopher et al. examined the responses of droplet collision at a microfluidic T-junction convergence and demonstrated that the coalescence was enhanced by decreasing the capillary number. Yang et al. experimentally studied the coalescence of bubbles in a T-junction convergence and showed that the coalescence efficiency reduced with the increase of the liquid viscosity and two-phase superficial velocity [100].

Although some efforts have been devoted to the coalescence of bubbles and droplets in microfluidic devices, however, the coalescence mechanism of bubbles has not been fully understood. This work mainly focused on the transition of coalescence patterns and coalescence mechanism of bubbles at a T-junction convergence, and the effects of the gas and liquid velocities, liquid viscosity and bubble length on bubble coalescences.

6.1.2 The dynamics of droplet coalescence

During two liquid drops approaching each other in the ambient air, the van der Waals forces show a super-linear growth. When the gap between two leading edges becomes infinitesimal the van der Waals forces form the initial liquid bridge or neck [200] (for salt water droplets of diameters D = 4mm, the gap was reported to be in the order of hundreds of nanometers [201]). Usually, the neck will rapidly expand due to its lower pressure compared with the center of the droplets. However, the applied fields can adjust the expanding process. The presence of applied electrical field will change the shapes of the approaching oppositely charged droplets and then control the behaviors of the new forming neck [202]. The electrical stresses deform the leading edges into cones and determine their slop [202]. This makes it possible to change the capillary pressure in the new forming neck and then determine whether the droplets merge or not. Like the applied electrical fields, the applied magnetic fields cause ferrofluid droplet to stretch oriented in the direction of the field [73, 203]. The final shapes of ferrofluid droplets result from the balance of magnetic force and surface tension [204]. We use the magnetic Bond number to represent the ratio between magnetic force and surface tension $Bo = \mu_0 \chi l_c H^2 / \sigma$ [204]. Here $\mu_0 = 4\pi \times 10^{-7}$ N/A^2 is the permeability of

the free space, H the magnetic field strength, l_c the characteristic length and χ the initial susceptibility. The results demonstrate that the cones will form in the two extremities at higher magnetic field [203]. The similar cusps were reported in paranematic droplets under a non-uniform magnetic field [205]. Previous numerical simulation studied the coalescence of ferrofluid droplets in uniform magnetic field and reported a critical separation of the two droplets beyond which the coalescence is inhibited [206]. The coalescence of two ferrofluid droplets attaching to solid supports will form a liquid column. Previous works have studied the stability of the column not generated by coalescence magnetic field [207]. The slenderness of the column and the magnetic force co-determine the behaviors of the columns [207].

6.2 Results and discussion

6.2.1 Bubble coalescence in microchannel

6.2.1.1The bubble behaviors and trajectories at the T-junction convergence

In our experiments, the capillary number Ca ($Ca = \mu U / \sigma$) was adjusted by altering the two phase superficial velocity U ($U = \left(Q_G + Q_L\right)/W_c^2$) and the viscosity of the continuous phase μ. The microbubble size L_b was controlled by varying the gas/liquid flow rate ratio k ($k = Q_G/Q_L$), the two phase superficial velocity U and the viscosity of the continuous phase μ. We systematically studied the responses of bubble collisions at the T-junction convergence of the symmetric loop (Fig.2.1c) under different capillary number Ca and bubble size L_b. Three primary responses were observed: (1) colliding coalescence (Fig. 6.1A), (2) squeezing coalescence (Fig. 6.1B), and (3) non-coalescence (Fig. 6.1C1, 2C2). Colliding coalescence occurs when there is no time difference between the arrivals of the two daughter bubbles at the T-junction convergence as shown in Fig. 6.1A. During the process of colliding coalescence, the two daughter bubbles maintain their trajectories and almost without any deformation. When the fusion occurs, the main parts of the two daughter bubbles are still in the branches. When the capillary number Ca is relatively large, the squeezing coalescence occurs. The two daughter bubbles are stretched with large deformation at the

T-junction convergence and the front caps of daughter bubbles bend towards the outlet channel. Then the two daughter bubbles squeeze with each other side by side, flowing through the outlet channel. The relative velocity is negligible before the merging of the two bubbles, and the duration time for the coalescence process is much shorter (within 1.5 ms) than that in the unbounded space (usually longer than 10ms). For the non-coalescence of bubbles, two sub-regimes could be found: slipping non-coalescence (Fig. 6.1C1) and late non-coalescence (Fig. 6.1C2). For slipping non-coalescence, the two daughter bubbles collide and then dislocation occurs at the T-junction convergence. And under this circumstance, one of the two daughter bubbles can slip through the other, and then the two bubbles flow downstream in a pair end-to-end. Before the late non-coalescence occurs, the two daughter bubbles collide, and subsequently keep squeezing with each other side by side to reach the strongest deformation. At the end of the squeezing process, the release of the interfacial energy causes bubbles to separate quickly. At last, the non-coalesced bubbles travel downstream one after another.

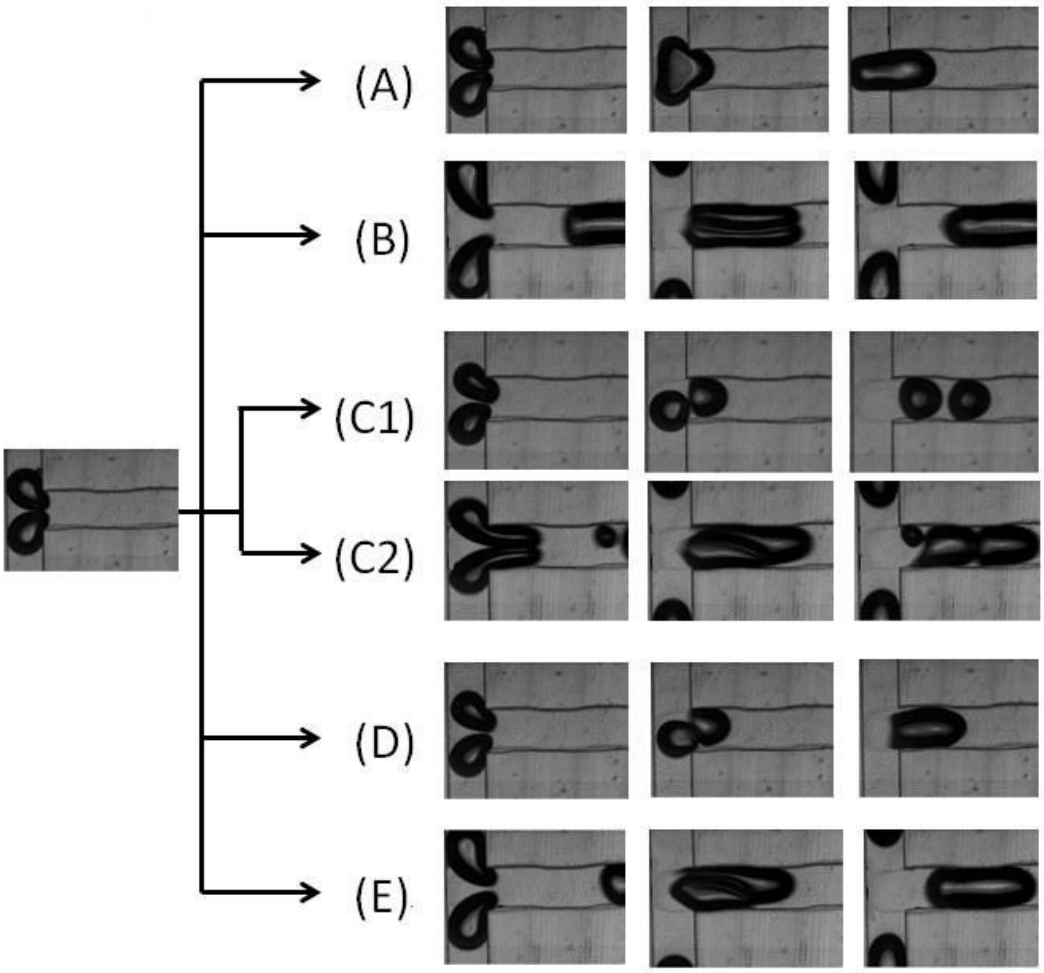

Fig. 6.1 Representative images of observed responses of bubble collisions at the microfluidic T-junction convergence. Primary responses: (A) colliding coalescence, (B) squeezing coalescence, (C1) slipping non-coalescence and (C2) late non-coalescence. Secondary responses: (D) slipping coalescence, and (E) late coalescence.

Besides the above-mentioned three main responses of bubble collisions, there are several secondary behaviors which are rare events: slipping coalescence (Fig. 6.1D), and late coalescence (Fig. 6.1E). The initial stage of slipping coalescence is similar to that of slipping non-coalescence. The two bubbles keep contacting with each other during the slipping process. Before the front bubble completely drives into the outlet channel, the coalescence occurs. The initial stage of late coalescence resembles that of late non-coalescence. But when the squeezing process comes to the end, the relative motion between the two bubbles appear due to the release of interfacial energy, and the merging of bubble pairs occurs.

The trajectories (centroid distances) of the approaching bubbles were used to characterize the responses of bubble collision, including colliding coalescence, squeezing coalescence, slipping non-coalescence and late non-coalescence (Fig. 6.2). The distance between the gravity centers of approaching bubbles was obtained by using a home-made Matlab program. The distance between the gravity centers of the approaching bubbles D was normalized by the width of the channel W_c and the time t was normalized by the ratio between the width of the channel W_c and the superficial velocity in each of the branches U_b ($U_b = 0.5(Q_G + Q_L)/W_c^2$). The dimensionless distance between the gravity centers of approaching bubbles was plotted as a function of the dimensionless time for the primary collision responses as shown in Fig. 6.2. In all cases, the initial bubble trajectories are linear with time, owing to the constant speed of bubbles determined by the constant flow rates of both phases driven by the syringe pumps [152] and the weak interactions between bubbles with relatively large distance. At later time, the daughter bubbles contact with each other, and then differences emerge. Specifically, for colliding coalescence, the fusion occurs when the bubbles contact with each other. The main parts of bubbles still remain in the branches, thus the interaction between the bubbles is weak. In this case, the distance between the gravity centers of bubbles is still linear with time. In contrast to colliding

coalescence, the bubbles are deformed significantly and are strongly interacted with each other for the squeezing coalescence process. Thus the dimensionless distance of the gravity centers of bubbles approximately decreases to 0.5, and the tendency terminates after the fusion as shown in Fig. 6.2. For slipping non-coalescence and late non-coalescence, the dimensionless distance of the gravity centers of bubbles decreases linearly with time firstly, and then increases slightly up to a constant value. This phenomenon demonstrates that the contact time t_c is not sufficient for bubbles to coalesce in these two cases. Fig. 6.2 indicates that the duration of the squeezing coalescence of bubbles is much longer compared with the colliding coalescence of bubbles. Therefore, the squeezing coalescence of bubbles needs much longer contact time t_c for the coalescence, compared with the colliding coalescence of bubbles.

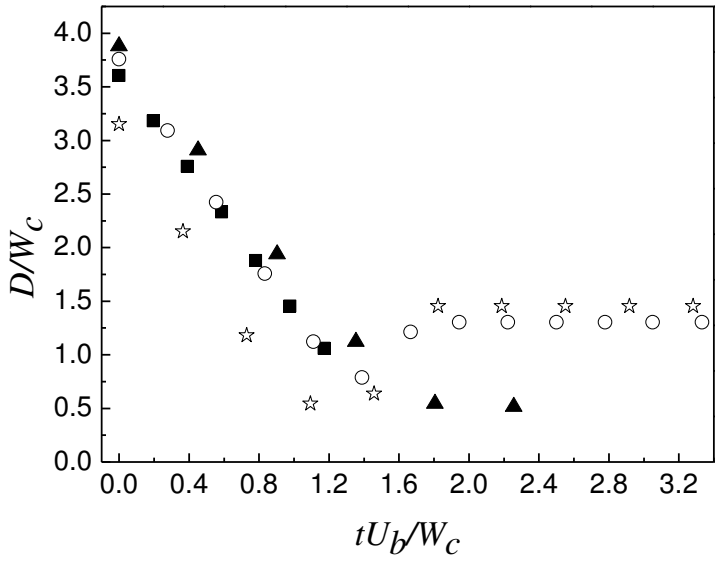

Fig. 6.2 Representative trajectories for bubble pairs approaching the T-junction convergence. The plot shows the distance between the gravity centers of the approaching bubbles D as a function of the dimensionless time tU_b/W_c: (■) colliding coalescence, (▲) squeezing coalescence, (○) slipping non-coalescence and (☆) late non-coalescence.

6.2.1.2 Operating diagram for the responses of bubble collisions at the T-junction convergence

The responses of bubble collision (sample size is larger than 125) at the T-junction

convergence depend on bubble size L_b and the capillary number Ca [152], as illustrated in Fig. 6.3. Colliding coalescence occurs at low capillary number. Non-coalescence is situated at the region with large capillary numbers and small bubble sizes. The squeezing coalescence region locates at moderate capillary numbers. The dimensionless bubble size is defined as $\varepsilon = L_b/\pi W_c$.

In our experiments, the critical capillary number Ca_C for coalescence decreases sharply with the decrease of the dimensionless bubble size and conforms to the following expression (Fig. 6.3):

$$Ca_C = 0.675\varepsilon^3 \quad (0.30 < \varepsilon < 0.45) \tag{6-1}$$

This law is different from that reported by Christopher et al. [152]. The difference may be caused by the significant difference of physical properties of the dispersed phase. Compared to the droplets used as the dispersed phase in the work of Christopher et al.[152], the bubble studied in our experiment with lower density and smaller inertia is more sensitive to the collision and disturbance caused by the flow field. This makes the bubble pair becomes easy to dislocate with each other, reducing the contact time between bubbles and thereby the probability of bubble coalescence. Furthermore, with the decrease of the bubble size L_B, the time for the two daughter bubbles flowing through the outlet of the loop t_L ($t_L = L_B/U_A$) decreases, here U_A denotes the average velocity of the two daughter bubbles passing through the outlet. So, the smaller the bubble size is, the more sensitivity is the bubble to the collision and disturbance. Therefore, with the decrease of the dimensionless bubble size ε, bubbles become more difficult to coalesce, thus the capillary number Ca_C decreases sharply.

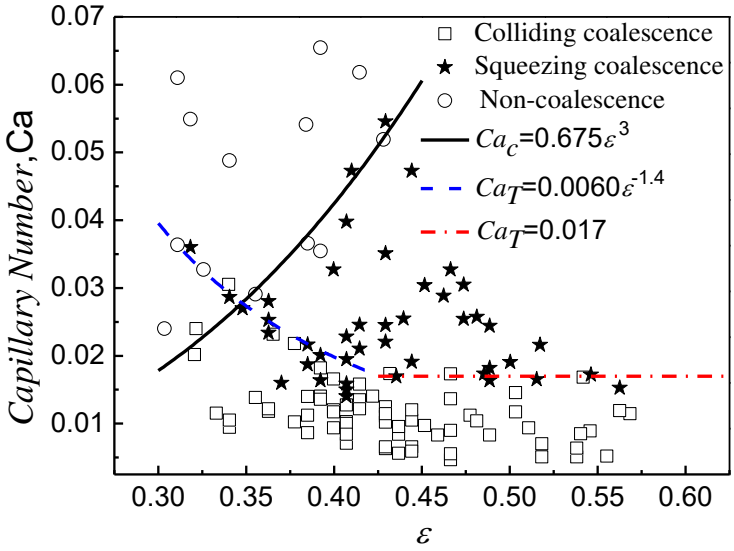

Fig. 6.3 Operating diagram organizing droplet behavior as a function of the capillary number *Ca* and the dimensionless bubble size ε. The dotted line represents the critical capillary number for bubble pairs transformed from colliding coalescence to squeezing coalescence. The solid line represents the critical capillary number for bubble pairs from coalescence to non-coalescence.

Fig. 6.3 also indicates that the critical capillary number Ca_T for the transition from colliding coalescence to squeezing coalescence satisfies the following equations:

$$Ca_T = 0.0060\varepsilon^{-1.4} \qquad (0.30 < \varepsilon < 0.43) \qquad (6\text{-}2)$$

$$Ca_T = 0.017 \qquad (0.43 < \varepsilon < 0.63) \qquad (6\text{-}3)$$

It could be seen from Eqs. (6-2) & (6-3) that when ε is small ($0.30 < \varepsilon < 0.43$), the critical capillary number for transition Ca_T decreases with the increase of ε, then Ca_T remains at 0.017 when ε is above 0.43. There are several reasons for this trend. When the bubble is small, it is sensitive to the collision. If the fusion of bubbles does not happen after collision, the dislocation will occur and the daughter bubbles flow into the outlet channel one by one. When the bubble size is large enough, the bubble behaviors are not sensitive to the collision, so the critical capillary number for the colliding-to-squeezing transition for bubble coalescence Ca_T remains stable.

A typical colliding coalescence sequence was shown in Fig. 6.4a, and could be described as follows: firstly, the two daughter bubbles approach each other gradually (t_1 - t_{10}). Due to relatively small *Ca,* bubbles are deformed slightly [152], and the two daughter bubbles contact with each other almost head-on-head in the entrance of the

outlet channel. No flat film is observed between the two bubbles; secondly, from t_{10} to t_{11} the neck is formed connecting the two daughter bubbles, and the structure of the neck is illustrated in Fig. 6.4b; thirdly, the two bubbles merge as a whole quickly, driven by the surface tension [41], then the coalesced bubble flows into the outlet channel. For the squeezing coalescence as shown in Fig. 6.4c, the daughter bubbles are elongated and the contacting point where they first touch each other moves into the outlet channel (t_1 - t_6). The similar process was reported by Christopher et al.[152]. Then, the two daughter bubbles squeeze with each other flowing downstream until coalescence occurs in the outlet channel (t_7 - t_9). At last, the coalesced bubble flows downstream.

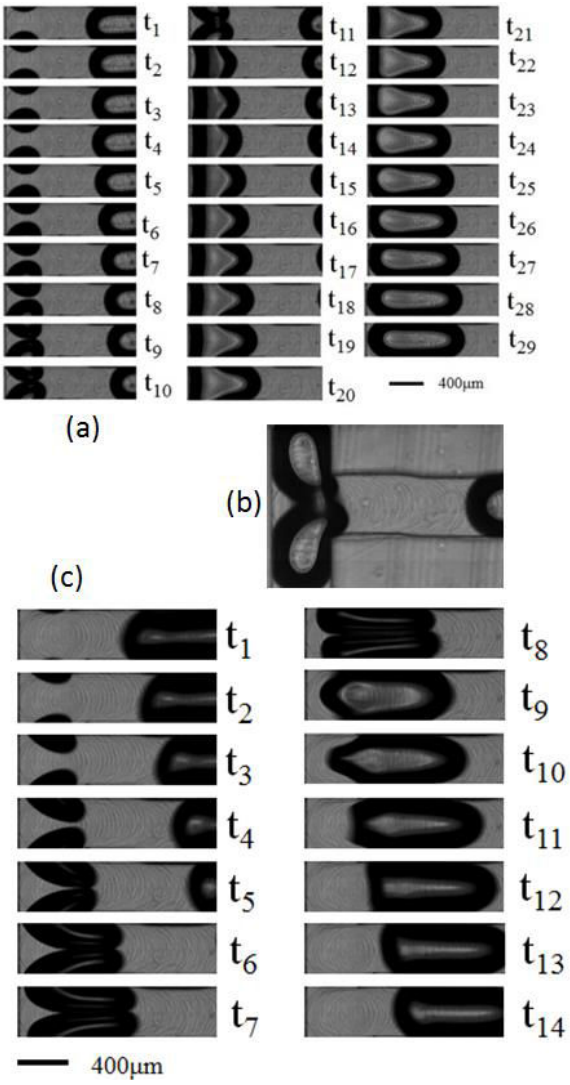

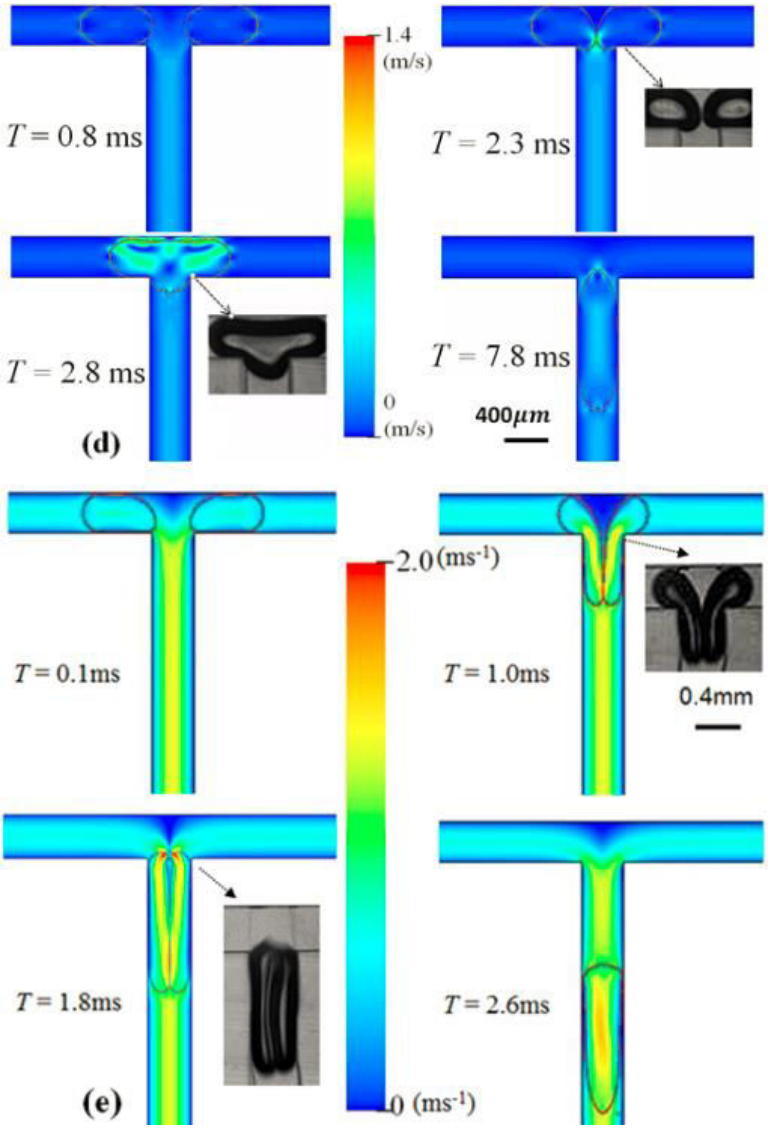

Fig. 6.4 (a) Temporal evolution of colliding coalescence process of bubbles. Q_G = Q_L = 80 mL/h. Liquid phase: μ = 1.41 mPa s. (b) Formation of the neck connecting the two bubbles. (c) Temporal evolution of squeezing coalescence process of bubbles. Q_G = Q_L = 210 mL/h. Liquid phase: μ = 2.51 mPa s. The time interval between two successive frames is fixed at 1/7000 s in (a) and (c). (d) - (e) Simulation of bubble coalescence and the contours of velocities in the continuous phase at the T-junction convergence. (d) colliding coalescence. Ca = 0.0036, ε = 0.51. (e) squeezing coalescence. Ca = 0.047, ε = 0.51. The zero time is defined as the moment for the front caps of bubble pairs reaching the outlet channel. The insets in (d) and (e) are pictures captured by a high speed-camera, validating the numerical simulation used.

The flow fields in the continuous phase around the colliding bubbles at the T-junction

convergence were numerically simulated for the two kinds of coalescence processes, to explain the reasons for the deformation of bubbles and the location where coalescence occurs for the two different types of bubble coalescence. The simulated bubble behaviors were validated by experiments as shown in Figs. 6.4d & 6.4e. For the colliding coalescence, the stagnant zone and the velocity gradient near the outlet are relatively small and the bubbles maintain their trajectories with slight deformation before the collision as shown in Fig. 6.4d also see in Fig.6.5a. While for the squeezing coalescence, the stagnant zone and the velocity gradient near the outlet are relatively large and the bubbles are stretched heavily as shown in Fig. 6.4e also see in Fig.6.5b. The front caps of the bubbles bend to the outlet channel, and then they squeeze with each other side by side. Yan et al. numerically studied the coalescence of droplets in pressure-driven flow through a constricted capillary tube. They reported that the locations where the coalescence occurs move downstream with the increase of the capillary number, and the squeezing coalescence occurs when Ca ranges from 0.05 to 0.064. The difference of the critical capillary number for the colliding-to-squeezing transition Ca_T may be caused by the different properties of fluids and the channel structures employed.

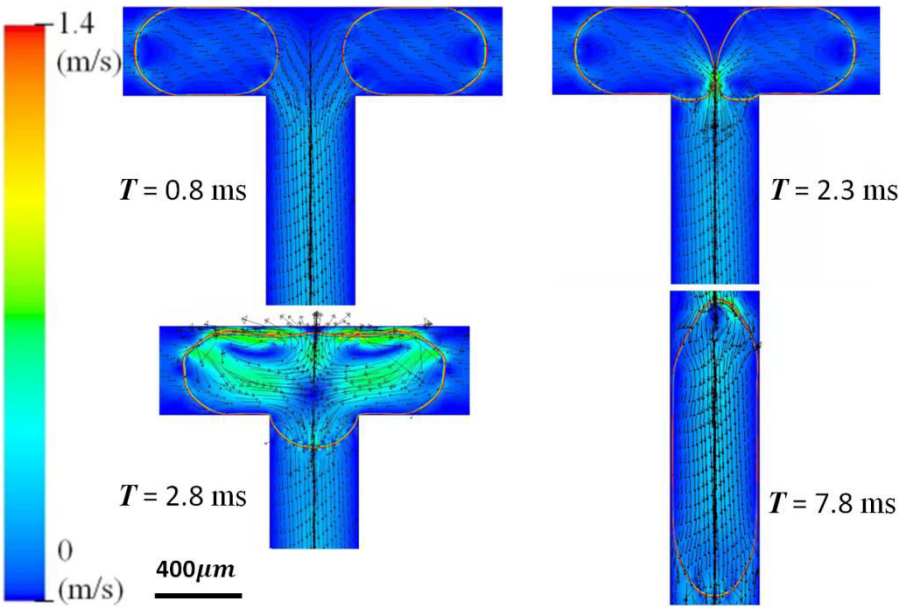

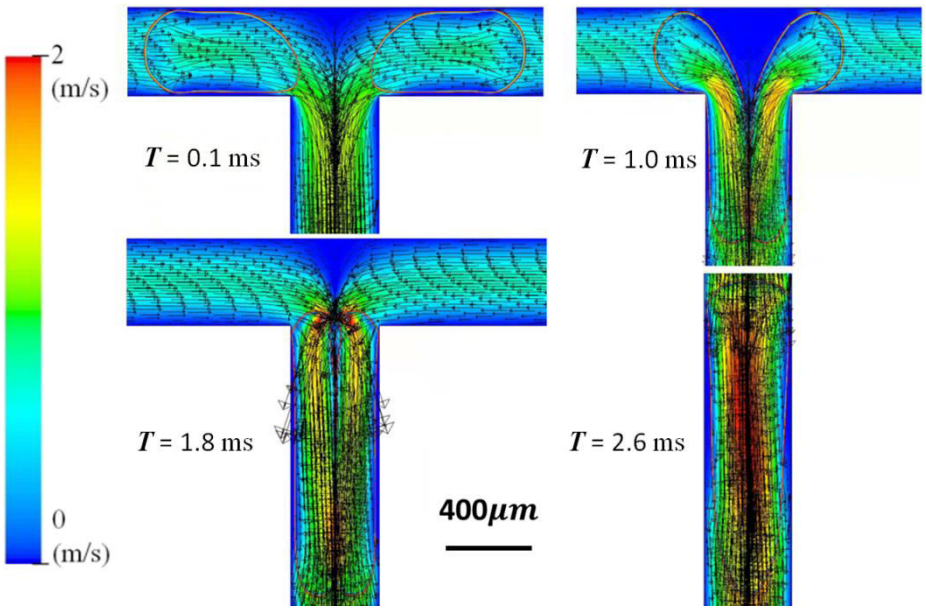

(b)

Fig.6.5 (a) - (b) Simulation of bubble coalescence and the velocity fields in the continuous phase at the T-junction convergence. (a) colliding coalescence. *Ca* = 0.0036, ε = 0.51. (b) squeezing coalescence. *Ca* = 0.047, ε = 0.51. The zero time is defined as the moment for the front caps of bubble pairs reaching the outlet channel.

6.2.1.3 The temporal evolution of the neck of coalesced bubbles for the colliding and squeezing coalescence processes

In order to shed insight into the coalescence mechanism, we measured the neck width *r* of the coalescing bubbles to characterize the coalescence process as shown in Figs. 6.6a and 6.6b. The temporal evolution of the bubble neck for the colliding and squeezing coalescence processes is shown in Fig. 6.6c. The time zero was set as the moment of the two bubbles contact with each other. Fig. 6.6c demonstrates that the colliding and squeezing coalescence undergo different evolution processes. At first, the squeezing coalescence experiences longer contact time t_c before the formation of the neck. Secondly, the velocity U_n ($U_n = \Delta r / \Delta t$) for the squeezing coalescence is higher than that for the colliding coalescence, and is also higher than the velocity during the coalescence process of two droplets reported by Yokota and Okumura (2010). This could be explained from that the viscous dissipation in the region near the neck and in the thin film between the coalescing bubbles could be ignored [208]. In our experiments, the surface energy σr^2 per unit time $d(\sigma r^2)/dt$ is balanced by the kinetic energy *Mar* per unit time *d(Mar)/dt*. Here σ is the interfacial tension, *M* the

mass of the thin film and a the acceleration speed. For the squeezing coalescence process, the bubbles closely contact with each other (t_8 in Fig.6.4c), the film between the two bubbles is invisible. Thereby M is relatively small, which leads to a great acceleration speed. Therefore, a jump of r is observed for the squeezing coalescence as illustrated in Fig. 6.6c. Thirdly, r undergoes a decreasing and then stabilizing process at later time for the squeezing coalescence. This phenomenon is caused by the inertia force, induced by the large velocity U_n. Therefore, the interface is stretched as shown at t_9 in Fig.6.4c. However, r increases slowly at the later time for the colliding coalescence. This is because the interface of the tail of the coalescing bubbles is bounded by the walls as shown at t_{13} in Fig.6.4a. However, the contact time for both the squeezing and colliding coalescence is much shorter than that reported by Yokota and Okumura (2010). This may be caused by the large interfacial tension and low density and viscosity of gas bubbles used in our experiments.

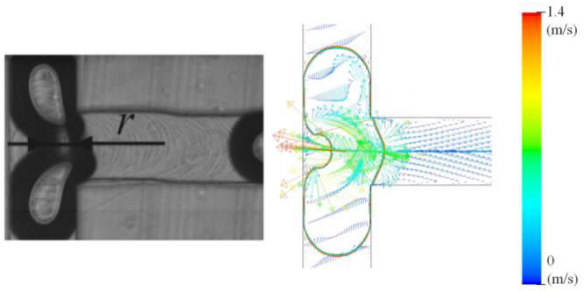

(a)

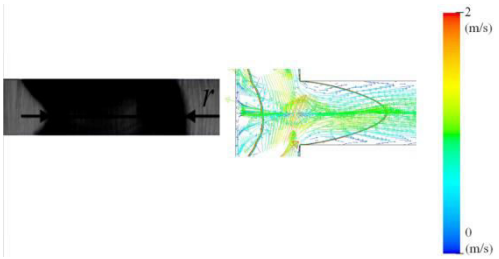

(b)

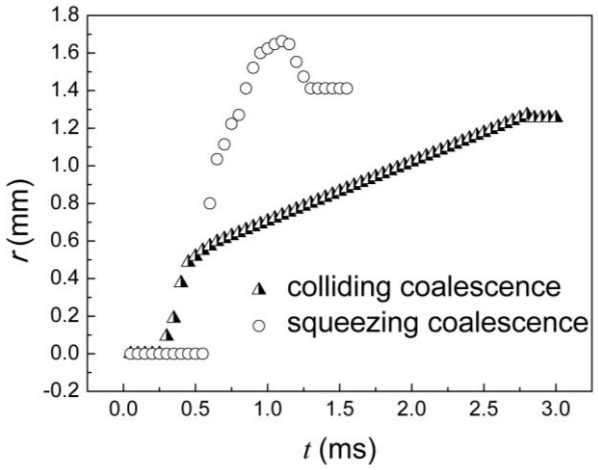

(c)

Fig. 6.6 (a) - (b) The characteristic width of the neck for the coalescing bubbles: (a) the colliding coalescence, (b) the squeezing coalescence. (c) The temporal evolution of the width of the neck for the colliding and squeezing coalescence.

6.2.1.4 Studies of influences on the efficiency of bubble coalescence

The coalescence could be regarded as a probability event [100]. And the efficiency for bubble coalescence could be predicted by the film drainage model, when the interface of bubble is deformable and mobile. According to this model, the efficiency for bubble coalescence depends on two characteristic time scales: the bubbles contact time t_c and the film drainage time t_d, which is the time required for the film between bubbles to thin down to a critical thickness. Coulaloglou (1975) proposed a model for the efficiency of bubble coalescence λ:

$$\lambda = exp(-\frac{t_d}{t_c}) \tag{6-4}$$

For the viscosity-controlled bubble coalescence, the film drainage time t_d is proportional to the viscosity μ and interfacial tension σ of the continuous phase, curvature radius r of the bubble and the variation of film thickness between bubble surfaces:

$$t_d \sim \frac{\mu r}{\sigma} \ln\left(\frac{h_i}{h_f}\right) \tag{6-5}$$

where h_i is the initial film thickness and h_f is the final film thickness before fusion.

For the inertia-controlled bubble coalescence [104]:

$$t_d \sim \frac{\rho_c u_t r^2}{\sigma} \tag{6-6}$$

here u_t is the relative velocity between bubbles, and ρ_c the density of the continuous phase. In our experiments, the Reynolds number Re ($Re = \rho U W_c / \mu$) spans between 8 and 400, the bubble coalescence falls into the transformation region. Therefore, both of the viscous force and the inertia force affect the film drainage time t_d and the above-mentioned Eqs 6-5 & 6-6 could not be employed in our studies. Thus a new function is needed to express the film drainage time. To achieve this end, we extract the film drainage time for both the squeezing and colliding coalescence processes under different two-phase superficial velocities as shown in Fig. 6.7. The period from the moment when bubbles contact each other to the point when coalescence occurs was defined as the film drainage time t_d. The variation trends of t_d are different at low flow rates and high flow rates. The film drainage time seems to rely on U for the colliding coalescence, rather than for the squeezing coalescence. And combining the influence of viscosity, the film drainage time is assumed to be expressed as:

$$t_d \sim U^n \mu^m / \sigma^v = Ca^v U^{n-v} \mu^{m-v} \quad (n, m \text{ and } v > 0)$$

for the colliding coalescence (6-7a)

$$t_d \sim U^z \mu^m / \sigma^v = Ca^v U^{-v} \mu^{m-v} \quad (z \approx 0, m \text{ and } v > 0)$$

for the squeezing coalescence (6-7b)

The bubble contact time t_c is calculated by the following equation:

$$t_c \sim \frac{L_c}{u_a} \tag{6-8}$$

Where L_c and u_a denote the distance traveled by the bubble pair from collision to coalescence and the average velocity of the bubble pair during this process, respectively. When the film drainage time t_d is always larger than the bubble contact time t_c, coalescence will not occurs. When the bubble contact time t_c is equal to the film drainage time t_d, we derive the critical capillary number $Ca_C \sim L_c$, from Eqs. 6-7 and 6-8. And due to $L_c \sim \varepsilon$, so we can derive $Ca_C \sim L_c \sim \varepsilon$. This result accords with Fig. 6.3.

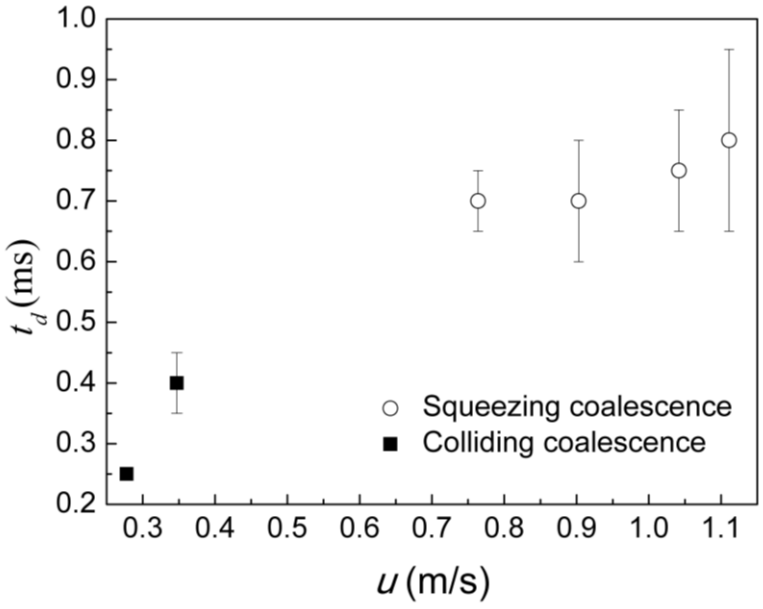

Fig. 6.7 Effects of the two-phase superficial velocity on the film drainage time. μ =1.83 mPa s.

Effect of the velocities of both phases

Previous researches have shown that the two phases superficial velocity U influences the coalescence efficiency λ, and coalescence favors low velocity [104]. The coalescence efficiency is plotted as a function of the two-phase superficial velocity under four different viscosities (from $0.347ms^{-1}$-$0.903ms^{-1}$) as shown in Fig. 6.8. When the liquid viscosity is sufficiently low (μ = 1.01 mPa s) or sufficiently high (μ = 6.14 mPa s), the impact of the velocity on the bubble coalescence is not obvious. According to Eq.6-7, under the above-mentioned two extreme instances, the film drainage time t_d < bubble contact time t_c and the film drainage time t_d > bubble contact time t_c, respectively. Thus within the range of our experiments, the influence of the velocity on bubble coalescence is concealed. When the viscosity is in the middle range (μ = 1.83 mPa s and μ = 2.10 mPa s), the velocity plays a key role in coalescence efficiency, which is quite different from that in large-scale containers [104]. As shown in Fig. 6.8, under moderate viscosity of the liquid phase, the coalescence efficiency does not always decrease with the increase of the two phase superficial velocity. When the velocity reaches a certain value, the coalescence probability begins to grow. But when the velocity increases further, the coalescence efficiency falls again and no longer bounces off. This phenomenon could be explained by the fact that there

is a transition of fusion pattern from collision to squeezing coalescence when the velocity increases to a certain value. During the process of squeezing coalescence, when the bubbles enter the exit, they are stretched significantly and the front caps of bubbles bend to the downstream. With the bubble pairs moving further to the downstream, the medial surfaces contact and squeeze with each other. Compared with Fig. 6.4d, it was found from Fig. 6.4e that the film drainage time t_d just increases slightly with the increase of the two phase superficial velocity U. And the transition from the colliding coalescence to squeezing coalescence leads to an effective decrease of slip after the contact of bubbles. This will lead to an increase of L_c, so t_c increases obviously, according to Eq. 6-8. Therefore, the coalescence efficiency will increase as shown in Eq. 6-4, proposed by Coulaloglou (1975). Besides the relative velocity between gas and liquid phases is small, there is no surfactant in the system. Thus the gas-liquid interface could be regarded as a fully mobile surface [104]. And the stretched bubbles with larger curvature possess much rigidity according to Laplace equation, thus the dimple is difficult to form and the liquid is unlikely to be trapped between the contacted bubbles, which is beneficial for bubble coalescence [209, 210]. In the squeezing coalescence region, the second decrease of the coalescence efficiency with the increase of the two phase superficial velocity is owing to the reduce of the contact time between bubbles, as the highly deformed bubbles are more inclined to slip in downstream with the increase of the velocity after squeezing with each other side by side. In general, the increase of the velocities of both phases' results in the decrease of the coalescence probability, and a small bounce of coalescence probability occurs when the coalescence pattern transforms.

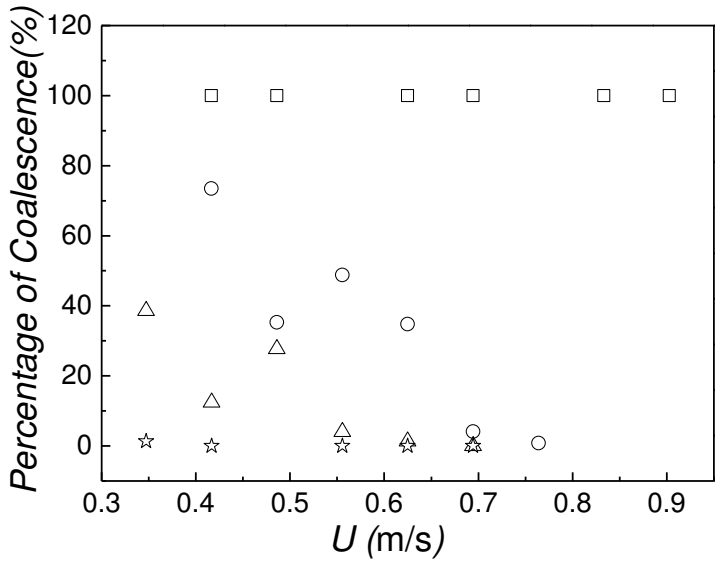

Fig. 6.8 Effects of the two phase superficial velocities on the percentage of coalescence of bubble pairs. (□) μ = 1.01 mPa s, (○) μ = 1.83 mPa s, (△) μ = 2.10 mPa s, (☆) μ = 6.14 mPa s.

Effect of the liquid viscosity

The influence of the liquid viscosity (μ = 1.16 mPa.s ~ 6.14 mPa.s) on the coalescence efficiency was investigated under two different two phase superficial velocities *U* (the gas/liquid flow rate ratio was 3:1) as shown in Fig. 6.9. The efficiency of coalescence decreases with the increase of the liquid viscosity. This trend was similar to bubble coalescence in large-scale containers [104]. The increase of viscosity will lead to the increase of the film drainage time t_d according to Eq. 6-7, thus it is more difficult for bubbles to merge. For low viscosities of the liquid phase (1.0 mPa.s - 2.50 mPa.s), the deviation of the coalescence efficiency for the two different superficial velocities augments as the viscosity increases. However, when the viscosity is higher than 2.5 mPa s, the difference of the coalescence efficiency between the two different velocities decreases abruptly, and then the coalescence efficiency continues to drop. This phenomenon could be explained as following. When the liquid viscosity is relatively low (1.0 mPa.s - 1.50 mPa.s), the film drainage time t_d is small, and the bubble pairs are inclined to fuse after collision for both of the superficial velocities. The coalescence efficiencies are high in both cases and the difference is quite small. The total coalescence efficiency declines with the increase of the liquid viscosity (1.50 mPa.s - 2.50 mPa.s). For the viscosity higher than 2.50

mPa.s, the collision coalescence with relatively high superficial velocity is transformed to squeezing coalescence, which facilitates coalescence. Hence the deviation of the coalescence efficiency diminishes suddenly. And when the liquid viscosity gradually increases, the film drainage time t_d increases. At last, bubbles slip past one another without coalescence. Therefore, the efficiency gap almost disappears under high viscosities of the liquid phase.

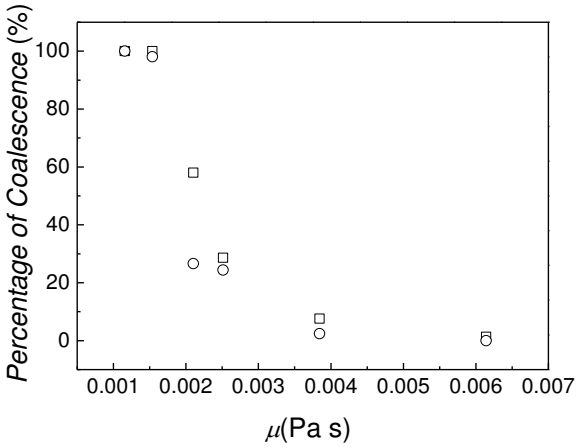

Fig. 6.9 Effects of the liquid viscosities on the percentage of coalescence of bubble pairs. (□) U = 0.3472 m.s^{-1}, (○) U = 0.5556 m.s^{-1}.

Effect of the bubble size

The effect of bubble size ε changing from 0.32 to 0.45 on coalescence efficiency under five different viscosities was studied as shown in Fig.6.10. For low (μ = 1.16 mPa.s) and high (μ = 6.14 mPa.s) viscosities, the effect of the bubble size on coalescence efficiency is insignificant. When the viscosity is in the middle range (from μ = 1.83 mPa.s to μ = 2.51 mPa.s), the coalescence efficiency increases with the increase of the dimensionless bubble size, and the increasing rate depends on the viscosity of the liquid phase. When the dimensionless bubble length ε is relatively small, the coalescence efficiency increases rapidly with the increase of ε; when the dimensionless bubble length ε is relatively large, the coalescence efficiency increases slightly with the increase of ε as shown in Fig. 6.10. For long bubbles confined in microchannels (ε > 0.32), the increase of the bubble size only lead to the increase of bubble length, but the curvature radius r is almost unchanged. Thus the film drainage time t_d is almost unchanged with the increase of the bubble size according to Eqs. 6-5

& 6-6. When the bubble is relatively small, with the increase of the bubble length, the bubble pairs are unlikely to slip after collision, resulting in the increase of the distance traveled by the bubble pair L_c, and thereby the augment of the bubble contact time t_c. And in this region, the coalescence of bubbles is sensitive to the bubble size, leading to a significant increase of the coalescence efficiency with the increase of the dimensionless bubble size. When the bubble is relatively large, the coalescence of bubbles becomes less sensitive to the dimensionless bubble size. Hence the coalescence efficiency increases slowly with the increase of the bubble size. This phenomenon coincides with the previous results. It could be concluded that the coalescence of bubbles is enhanced by increasing the dimensionless bubble length under moderate viscosities of the liquid phase.

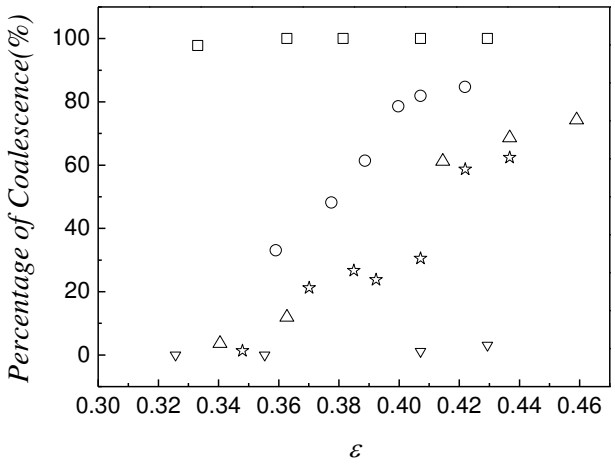

Fig. 6.10 Effects of the dimensionless bubble size on the percentage of coalescence of bubble pairs. (□) μ = 1.16 mPa.s, (○) μ = 1.83 mPa.s, (△) μ = 2.10 mPa.s, (☆) μ = 2.51 mPa.s, (▽) μ = 6.14 mPa.s.

6.2.2 Coalescence of ferrodroplet

6.3.2.1Dynamics of liquid bridge

The images captured just at the initial stage of the coalescence demonstrate that the ferrofluid pierces the surface of the tips as shown in Fig. 6.11a. Then a thin liquid bridge forms with a visible gap D_g in the order of tens of micrometers between the leading edges. While for salt water drops (saline water) in ambient air, the bridge

forms only when the gap between salt drops to be 280^{+370}_{-160} nm then the van der Waals forces play the leading roles [200]. This implies in our experiments that the van der Waals forces are not the driving force for generating the liquid bridge. Fig. 6.11a makes plain that the positive curvature around the thin bridge is much larger than the negative curvature across the neck at the initial stage. Thus the capillary pressure in the neck is larger than the center of the droplet. This will cause the collapse of the neck. Similar to the so-called Taylor cone in previous studies under the electrical fields, there is a critical cone angle as shown in Fig. 6.11a, of 30.8°. If the angle beyond the critical one it means that the capillary pressure in the neck is superior to the ferrodroplets causing a flow from the neck to the droplets. In contrast, the coalescence under magnetic field won't be limited by this angle. These descriptions above imply the dynamics of the coalescence under magnetic fields is distinctive. Fig. 6.11b shows the temporal evolution of the minimum width of the expanding neck W_n. The initial stages of expanding of the neck W_n not always satisfy the power law proportional to time t. And the power-scaling exponents of the t increase with the increased magnetic fields. These phenomena indicate that the capillary force is not the driving force any more to the expanding processes of the neck. The analysis of the high-speed images demonstrates that the approaching tips speed up when they close to each other under magnetic field. And we calculate the Weber number $We = \rho D_c V^2/\sigma$ under different magnetic fields. Here D_c is the curvature diameter of the droplet tip just before the formation of the neck, V the average approaching velocity of the two droplets (in the last 6.65×10^{-5}s before coalescence) of the approaching tips. The Weber number ranges from 0.33 to 1.25 corresponding to the magnetic flux density changing from 0.020T to 0.155T. Thus in our experiments, the inertial force stemming from magnetic attraction is in the same order of the capillary force and control the initial stage of the coalescence. In the initial expanding stage, the increase of the minimum width of the neck W_n with time t follows a power law with a constant exponent but deviates with a decreasing exponent in the later stage. During the initial stage, the position L_N of W_n in y-axis does not change and stays at the point where the liquid bridge forms as shown in Fig. 6.11a. And a moment later L_N grows (moving vertically towards the needle) as shown in Fig. 6.11c. When L_N grows, it depends on the geometric configuration of the top droplets (Fig. 6.11d) which are determined by the magnetic field [203]. The cone angle and the curvature diameter were measured and shown in Fig. 6.12a. It is obvious the droplets develop rounded but increasingly

distorted shape as the increase of the magnetic flux density. It is regular that once W_n closes to the curvature diameter the position of the minimum width starts to move upwards. Fig. 6.12b shows that critical widths increase with the decrease of magnetic flux density while the ratios of the critical width to the curvature diameter decrease slightly closing to 1 (the slight decrease is due to the much higher velocity in the thinner column). This phenomenon could be caused by the inertia of the rapid expanding neck which causes the negative pressure in the initial neck region compared with top droplet. It will inhale much liquid from the top droplet and the quantity of the liquid exceeds the transshipment from the needle. Thus the position moves upwards. After this L_N and W_n reach the maximum almost at the same time to form a liquid column. Due to the shape of the droplet before coalescence the maximum value of W_n increases with the increasing magnetic flux density. In fact, the cone angles and the curvature radii increase with the increased magnetic flux density (Fig. 6.12c).

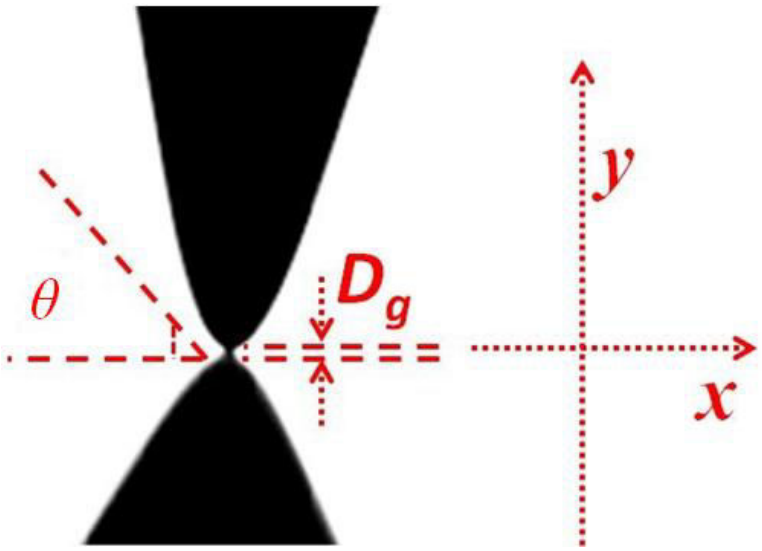

(a)

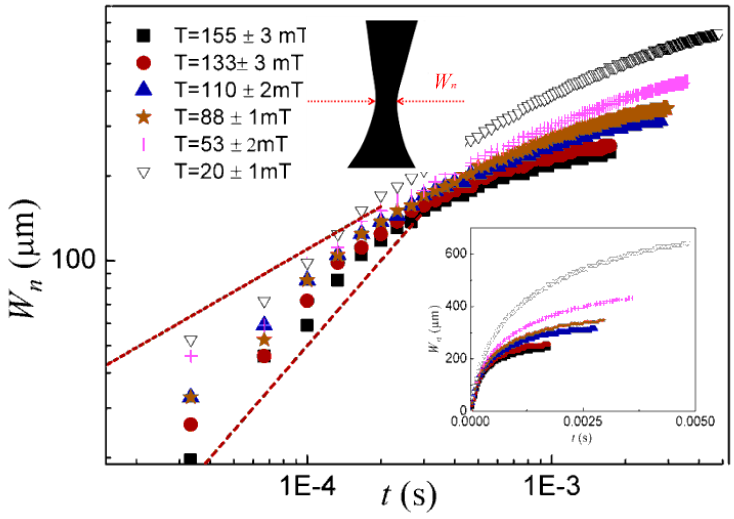

(b)

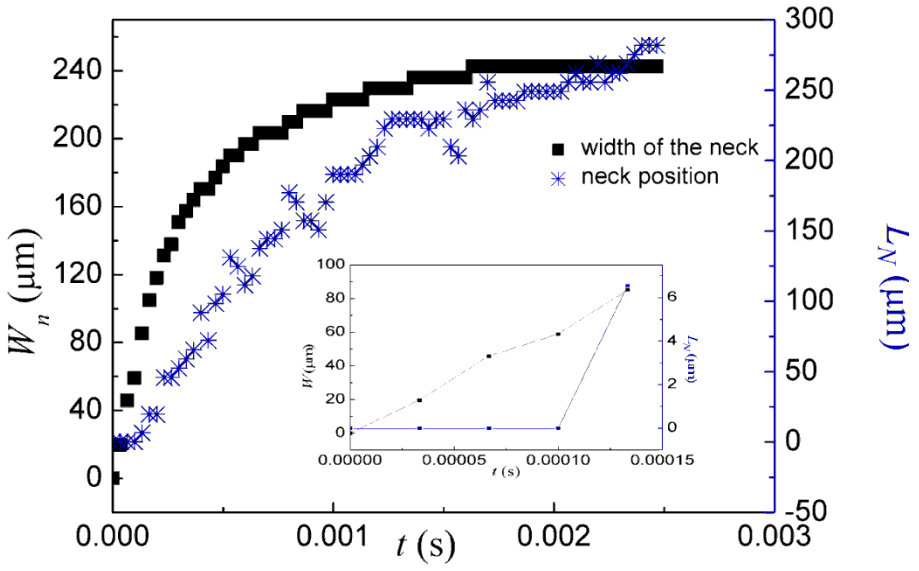

(c)

Fig. 6.11. (a) the initial formation of liquid bridge under magnetic field. (b) temporal evolution of the minimum width of the expanding thread W_n. (c) temporal evolution of the position L_N of the minimum width W_n in y-axis and W_n (B = 155mT).

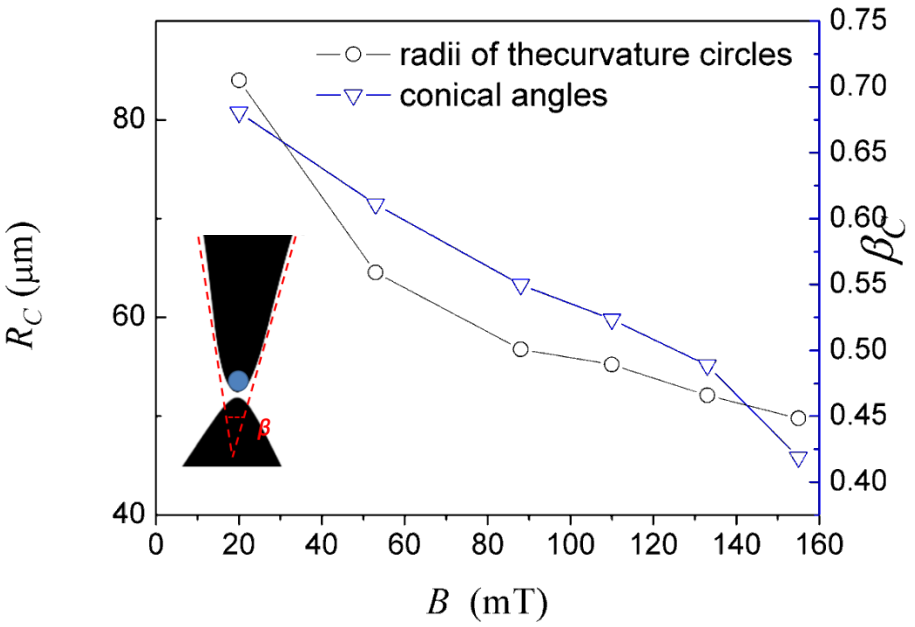
radii of thecurvature circles
conical angles
R_C (μm)
β_C
B (mT)
β

(a)

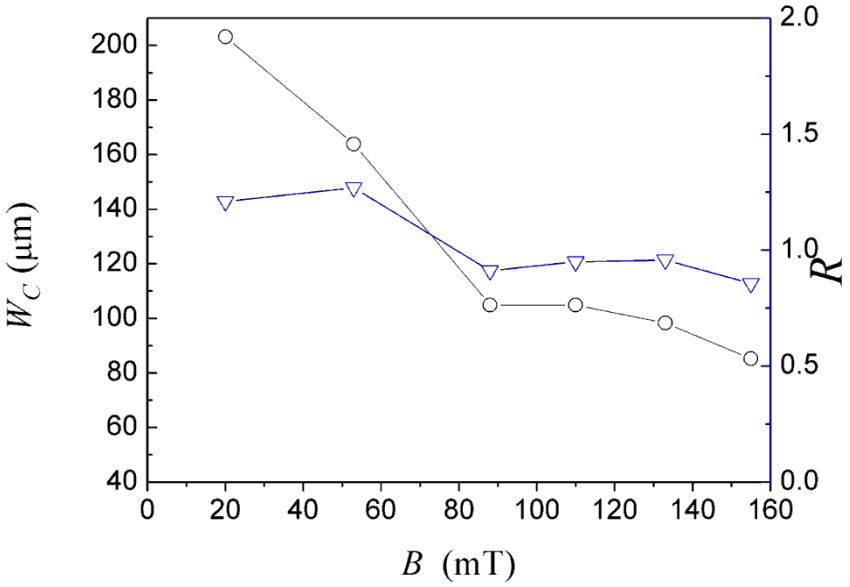
W_C (μm)
R
B (mT)

(b)

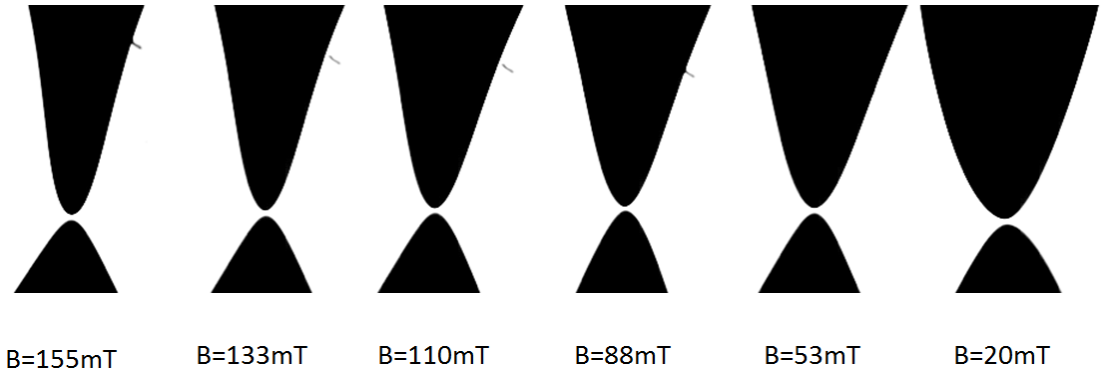

(c)

Fig. 6.12. (a) the evolution of cone angle and the curvature diameter with the increased magnetic flux density. (b) the evolution of critical widths and the ratios of the critical width to the curvature diameter with the increased magnetic flux density. (c) the evolution of the shapes of top droplets with the increased magnetic flux density.

6.3.2 .2 Stability of liquid column

After coalescence, the new forming columns exhibit different behaviors shown in Fig. 6.13a. We observe a critical magnetic flux density $B = 35^{+18}_{-4}$ mT, above this value the column will collapse. The minimum width W_n as a function of the time before pinch-off does not meet the exponential function. The previous studies indicate $W_n \sim (t - t_0)^n$ before pinch-off, where t_0 is the time pinch-off occurs and n is the scaling exponent. For inviscid Newtonian fluids, the power-law exponent is $n \approx 2/3$, and $n \approx 1$ for relatively viscous Newtonian fluids [211, 212]. In our experiments, the exponent is not a constant. The inset of Fig. 6.13a demonstrates the dynamics of pinch-off are different. Under relative high magnetic flux density ($88\text{mT} \leq B \leq 155\text{mT}$) the pinch-off velocities speed up all the time. While under moderate magnetic flux density the pinch-off velocity remains unchanged at the initial stage then speeds up (B = 53mT). This implies that the processes of pinch-off are different. In addition, we find the L_N of the minimum width W_n as shown in Fig. 6.13b decrease with the decrease of W_n under relative high magnetic flux density ($88\text{mT} \leq B \leq 155\text{mT}$). But L_N fluctuates substantially under moderate magnetic flux density. These results indicate the final pinch-off pattern changes from a single-breakage to a double-breakage which always results in the formation of satellite droplet. Fig. 6.14a shows the evolutions of the shapes before and after final pinch-off under different magnetic flux density. This transition of pinch-off patterns is caused by the flow rates

differences in each column. As shown in Fig. 6.13a, the maximum of W_n decreases with the increased magnetic flux density. The average velocity in the column is proportional to W_n^{-2}. Thus the liquid in thinner columns owns much higher axial momentum. Furthermore, the thinner column means a higher pressure drop in it. Taking these two factors into consideration, it makes plain that the cone angles increase with the increased magnetic flux density (Fig. 6.14b). After the final pinch-off, the ratio of capillary force to inertial force decreases gradually along the upwards direction for the thread with a higher cone angle. Thus the surface tension cannot generate another pinch-off point to form a satellite droplet.

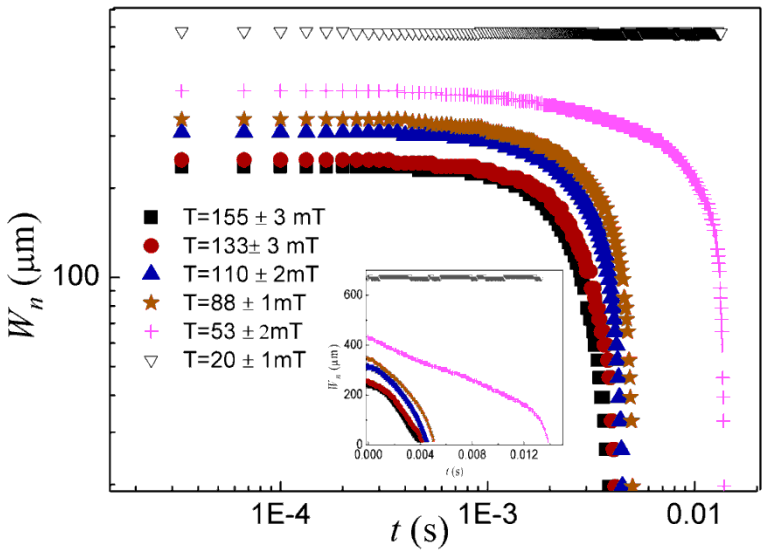

(a)

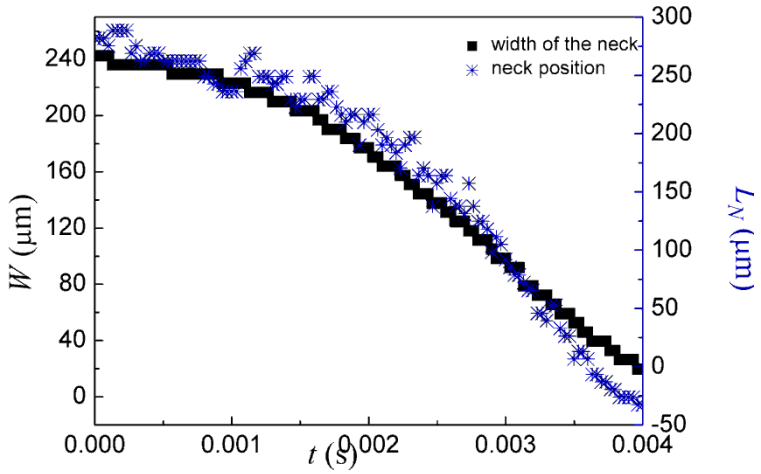

(b)

Fig. 6.13. (a) temporal evolution of the minimum width of the shrinking thread W_n. (c)

temporal evolution of the position L_N of the minimum width W_n in y-axis and W_n (B = 155mT).

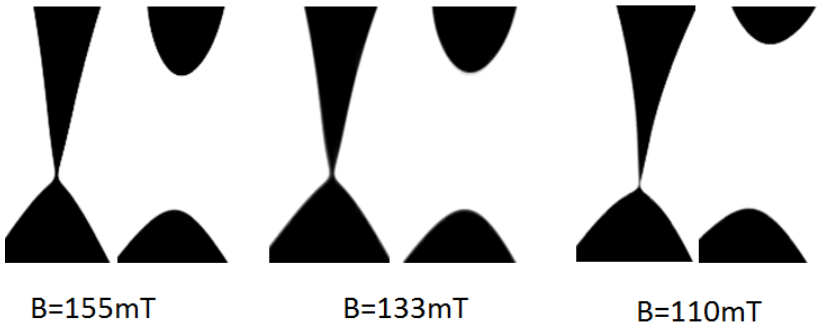

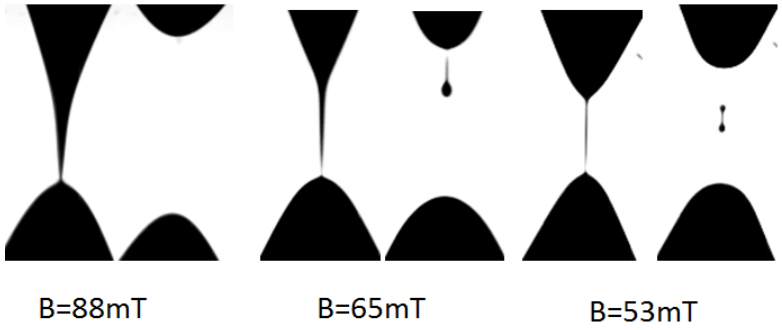

(a)

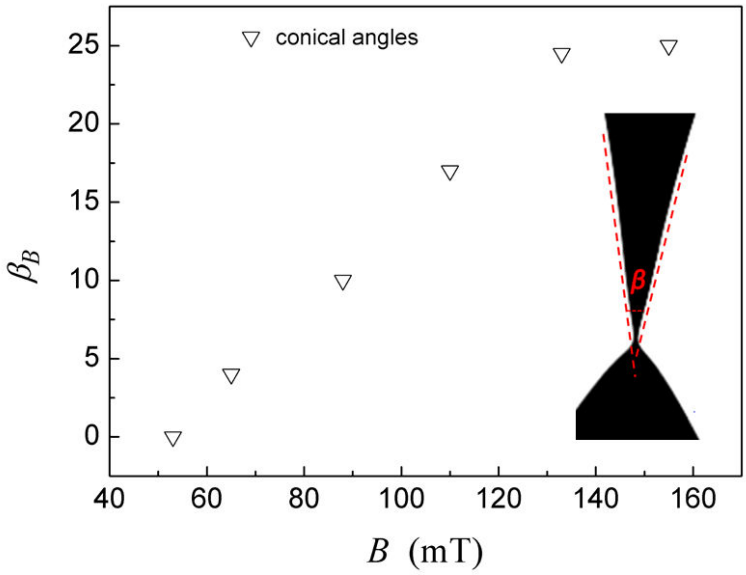

(b)

Fig. 6.14. (a) Evolution of the shapes before and after final pinch-off under different magnetic flux densities. (b) evolution of cone angles under different magnetic flux densities.

In these experiments, the frequency of the whole process increases with the increased

magnetic flux density shown in Fig. 6.15. Under high magnetic flux density (B = 155mT), the period of the whole process decreases by two orders of magnitude compared with the formation of a ferrofluid droplet without magnetic field (243 ± 3s).

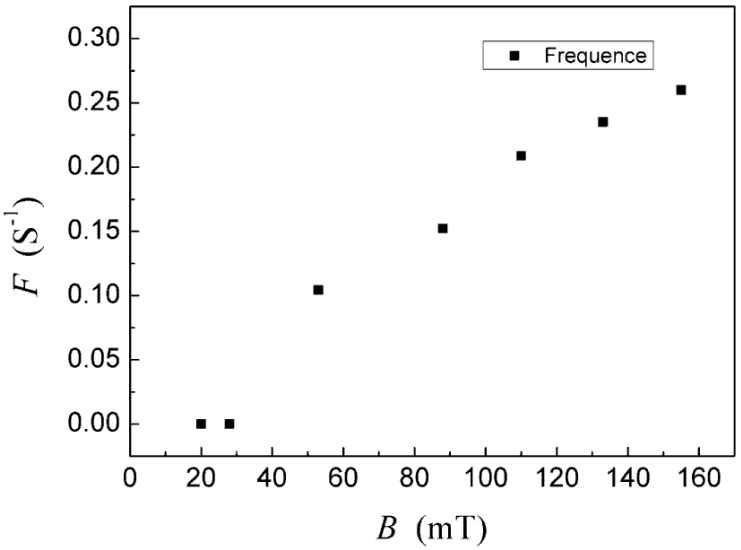

Fig. 6.15. Frequency evolution of the whole process in function of different magnetic flux densities.

6.3 Conclusions

In this chapter, colliding coalescence and squeezing coalescence of bubbles at a microfluidic T-junction convergence were observed and discussed. The results showed that colliding coalescence occurs at low capillary numbers. The squeezing coalescence occurs at moderate capillary numbers. When the capillary number is large and the bubble size is small, coalescence does not happen. The increase of the two-phase superficial velocity and the viscosity of the liquid phase induce the transition from colliding coalescence to squeezing coalescence, and consequently the transition enhances bubble coalescence. When the bubble is relatively small, the coalescence efficiency increases sharply with the increase of the bubble size for moderate liquid viscosities. Quantitative expressions were proposed to predict the film drainage time for bubble coalescence in the colliding coalescence and squeezing coalescence respectively, which could be applied to explain the influences on the efficiency of bubble coalescence. For ferrodroplet, the initial stage of ferrofluid droplet coalescence is controlled by the inertia of the droplets due to the magnetic attraction under high magnetic flux density. Due to the magnetic force, the

approaching tips attract each other, which facilitate the formation of liquid bridge. Different from the coalescence induced by electrical field, once the liquid is formed; the coalescence process will proceed and form a liquid column. By varying the magnetic flux densities, it is possible to change both the stabilities of the new forming columns and the pinch-off patterns to control the generation of satellite droplets.

Chapter 7 General conclusions and prospects

This thesis comprises experimental and computational studies of the breakup and coalescence of interface under micro-scale. The main contribution of the thesis is to reveal the breakup and coalescence mechanisms and enrich the knowledge about external field control. The understandings of the breakup and coalescence mechanisms allowed us to successfully design and characterize a microdevice. We now spend a few words to discuss some of our main findings in a broader perspective.

Both of the formation (chapter3) and breakup (chapter4) of droplets involve the breakup of interface and accompanied by the generation of new droplets. Thus, these two processes are analogical in the late period and they will undergo the thinning of the neck. In this thesis, to realize the active control of the breakup of interface, the uniform and non-uniform magnetic fields were applied. In both of the formation and breakup processes the magnetic force will exert influences on the geometrical morphology of the dispersed phase. The interface experiences elongation oriented to the magnetic field. This geometrical change leads to the variation of the accessible area by the continuous phase, which will bring the new force balance among shear, accumulated pressure, capillary force and magnetic force. Therefore, the breakup mechanisms transform. By varying the magnetic field, the active control of the thinning velocity and the frequency of generating new droplet could be realized. In addition, it was found the effects of magnetic field decrease with the increase of flow rates in both cases. There still exists some difference between the droplet breakup and the droplet formation. For the droplet formation, it will undergo an expanding stage and this stage could also be utilized to active control the formation process. Furthermore, in formation process all the flows will converge and pass through the same outlet after the final pinch-off of the interface, while the breakup process usually involve two or more outlet channels. Thus the hydrodynamic collective feedback needs more attention in breakup process. Duo to the higher surface tension of bubble compared with droplet the feedback effect is more pronounced. The feedback effect of bubble collision downstream on the upstream breakup of bubbles leads a remarkable asymmetry degree of bubble breakup. Moreover, the formation of satellite droplet is

closely linked to the thinning neck in the formation and breakup of the droplet. In both cases, the thinning of the neck will experience a final low speed stage due to the non-ignorable viscosity of dispersed phase. The non-uniform distribution of surfactants on the liquid-liquid interface results in the surface tension gradient and Marangoni effect. These phenomena coupled together lead to the double breakup of neck filament. Moreover in flow-focusing geometry the shape of the neck before rupture is linked to capillary number: symmetric for low capillary numbers and asymmetric otherwise. In contrast, the shape of the neck before rupture is more symmetric in T-junction. The size of satellite droplets increases with capillary number of continuous phase. Similar with above-mentioned satellites formation process, the breakup of the filaments at the droplet' (bubble') butt also leads to satellites. The formation of satellite droplets is caused by the presence of tip stream. There exists a critical capillary number which is a function of droplet length, above the value the tip stream will occur. The length of the tip stream increases with the two phase superficial velocity and exhibits a maximum at a given capillary number of $Ca = 0.5$.

The coalescence bubble and droplet were investigated, respectively. Firstly, colliding coalescence and squeezing coalescence of microbubbles at a microfluidic T-junction convergence were observed. Both the increase of the two-phase superficial velocity and the viscosity of the liquid phase induce the transition from colliding coalescence to squeezing coalescence. The effective contact between two bubbles will facilitate the gas bridge then this bridge expands rapidly. The whole coalescence is finished in about 3ms which is faster than the coalescence of droplets due to the higher surface tension and lower viscosity of bubbles. The velocity of the expanding liquid bridge between two ferrofluid droplets at the presence of magnetic field is lower than the gas liquid. Because the initial stage of ferrofluid droplet coalescence is controlled by the inertia of the droplets not the surface tension. But due to the magnetic force, the approaching tips attract each other, which facilitate the formation of liquid bridge which could enhance the coalescence efficiency.

7.2 Prospects

In this thesis, the micro-scale droplet (bubble) formation, breakup and coalescence processes were studied. The obtained results are helpful to the design of microdevices

and the underlying physical phenomena. To better understand the dynamics of interface phenomena and enrich the knowledge of the active manipulation by magnetic field, some work still need to be improved and summarized.

(1) To better utilize the magnetic field to control the droplet formation or breakup, the influence of the magnetic force on the ferrodroplet. The viscosity of ferrofluid is function of the strength of magnetic field and the viscosity is affected by the volume ratio of magnetic particle and average particle size. These data still missing. Much attention is needed to study the properties of ferrofluid.

(2) Up to now, there already exist many correlations and models to predict the critical droplet length in breakup process, while the lack of general mechanisms demonstrates that much work need to be done to establish intrinsic relationships between those various parameters.

(3) Surfactants are widely used in chemical engineering, but researchers have not comprehensively understood the dynamical behavior of surfactants at an interface undergoing deformation. Thus emphasis should be put on the migration of surfactants.

(4) When two droplets approach each other, the drainage process of continuous phase is complex especially due to the micro-scale phenomena and the presence of surfactants. This process still needs to be studied, thereby developing reasonable model to predict the drainage dynamics.

(5) Currently, piecewise function is used to predict the droplet size in different flow patterns. A unitary function of general form is still needed. The pre-existing transition criteria fail to provide the intrinsic relationships between various parameters and flow patterns. The external magnetic field was applied to control the transition of flow patterns (Fig.7.1) in flow-focusing geometry. The results need to be summarized to gain an insight into the nature of the transition of the flow pattern then to predict precisely the droplet size. Furthermore, this work could enrich the knowledge about active control.

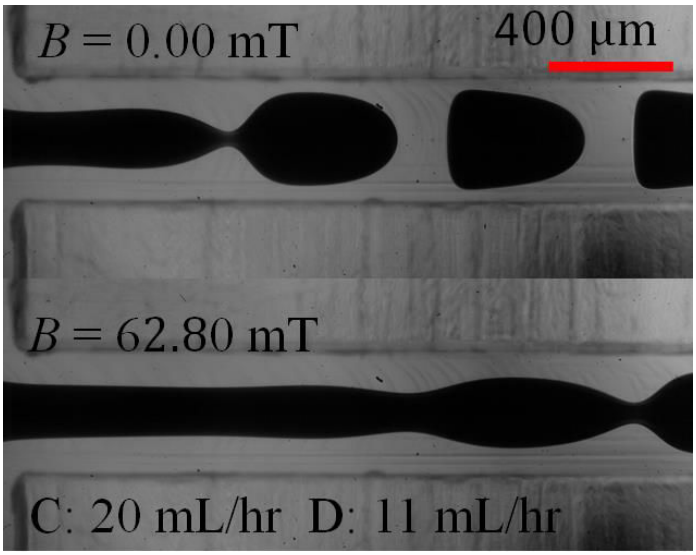

Fig.7.1 Transition of the flow pattern: from dripping (without magnetic field) to jetting (with magnetic field oriented in axial direction).

(6) The formation of the oil-based ferrofluid droplets at the end of a blunt needle (Fig.7.2) under different intensities of magnetic field has been performed. The experimental results need to be summarized and find the intrinsic relationship among the droplet size, the formation frequency, the length of the neck filament, the thinning velocity of the neck and the intensity of the magnetic field. The comparison between the results in confined space (microdevice) and unconfined space could provide valuable information about the influences of scale effect and magnetic force on the instability of interface.

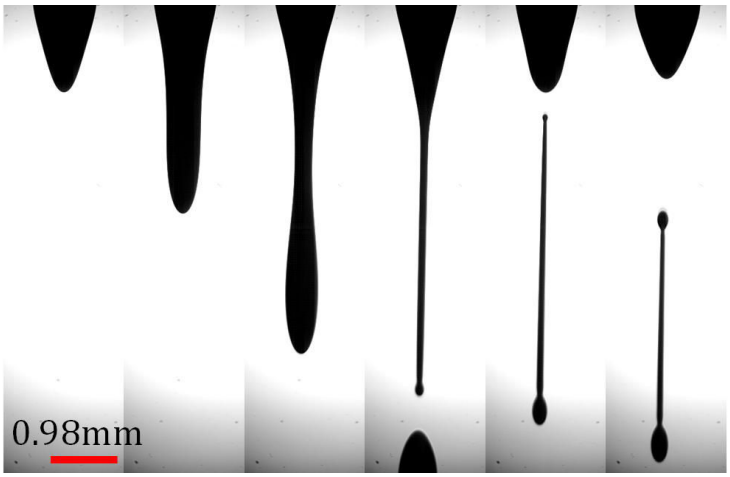

Fig.7.2 The formation of the oil-based ferrofluid droplets at the end of a blunt needle (B = 55.65 mT).

(7) The division of the oil-based ferrofluid droplet in 2% (wt)SDS/water solution (Fig.7.3) under different magnetic fields were conducted. The critical intensity of the magnetic field of the division is linked to the droplet size and the gradient of the magnetic field. The precise function is still missing. The results need further summarization to study the cause of the instability to better utilization of active magnetic manipulation.

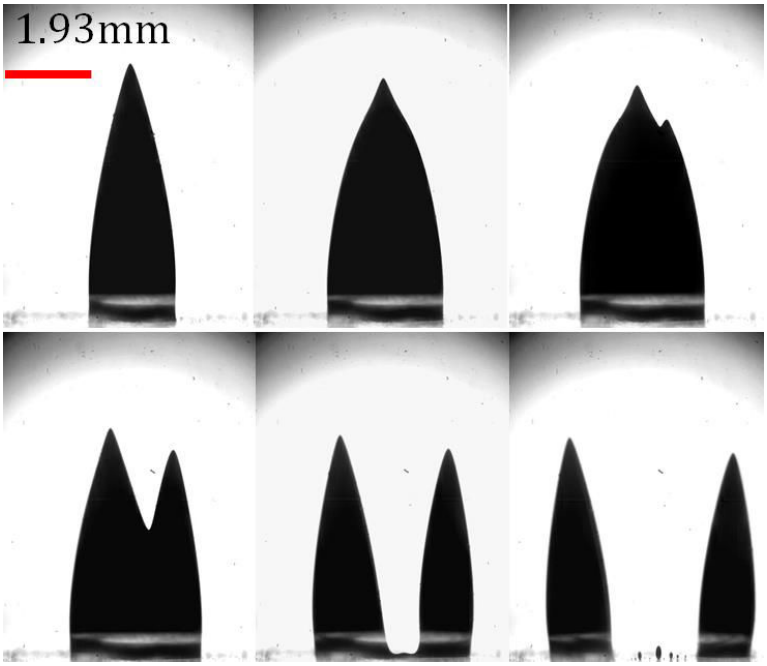

Fig.7.3 Photographs of the division of an oil-based ferrofluid droplet in 2% (wt)SDS/water solution under magnetic field.

(8) The spreading of droplets on a thin film or solid surface has important practical significance [215]. The impacts of water-based ferrofluid drop on different solid surfaces (Fig.7.4) were conducted. The results need to be analyzed to obtain the relationship among surface properties, spreading velocity and maximal spreading diameter. The influences of magnetic field on the contact angle, spreading velocity, maximal spreading diameter and the stability of the spreading precursor will be summarized. The influence of the magnetic field will on the transition between spreading and splash is deficient. The results will shed light on this problem and provide new method to active control the spreading process.

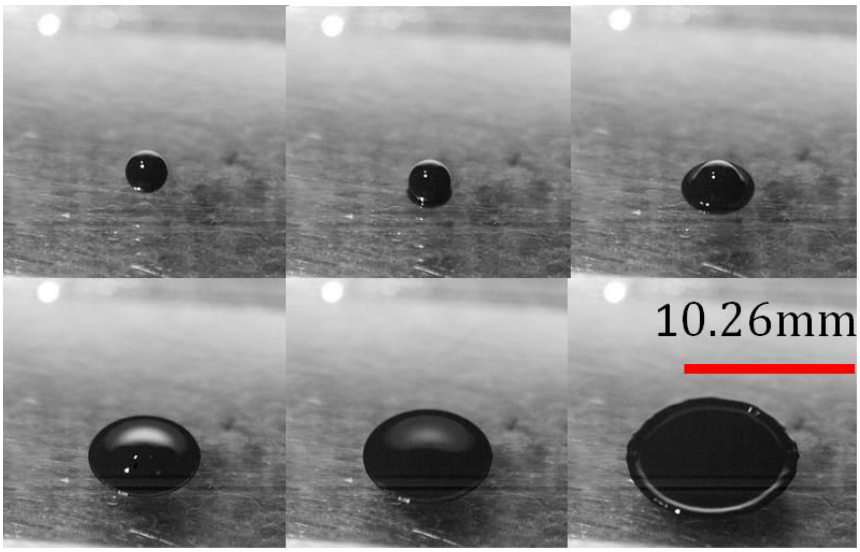

(a)

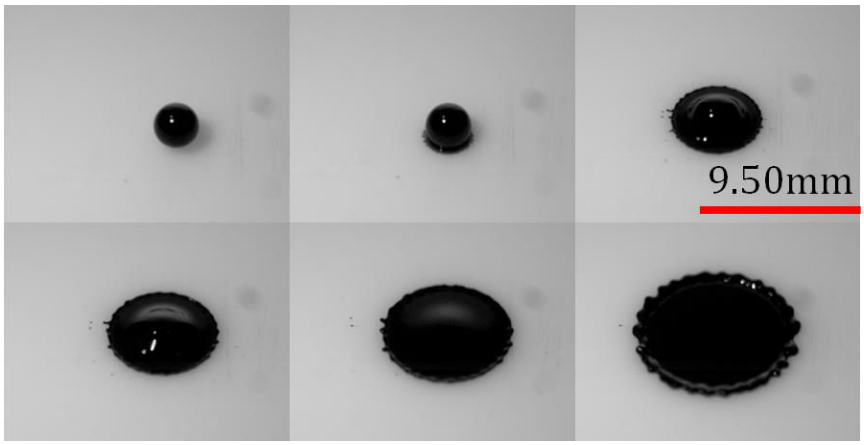

(b)

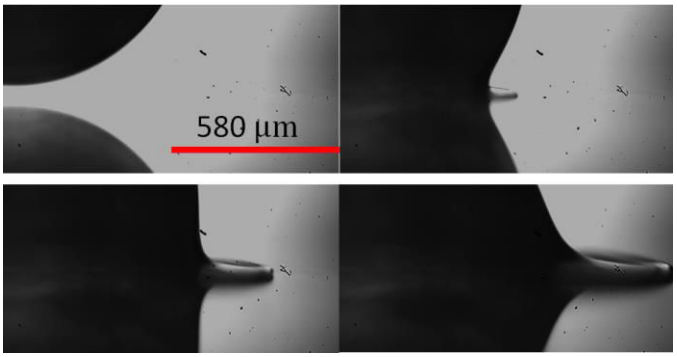

(c)

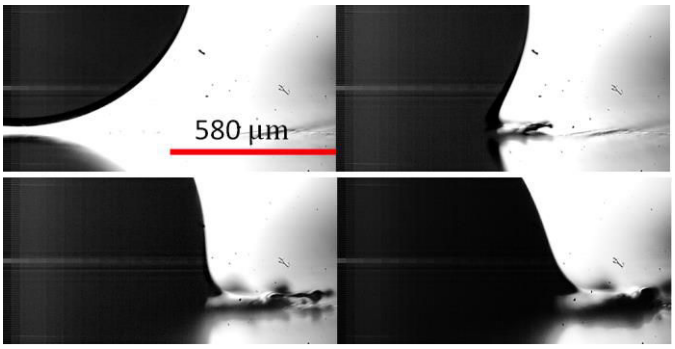

(d)

Fig.7.4 Impact of a water-based ferrofluid drops on (a), (c) glass and (b), (d) Teflon substrate. (c)-(d) The magnification of the precursor of the spreading liquid on glass and Teflon surface, respectively.

(9) A water-based ferrofluid drop spreads very rapidly just after it is gently deposited on a solid surface (Fig.7.5). The early stages of spreading are influenced by different types of surface properties (Glass (Fig.7.5a) and Teflon (Fig.7.5b)). The radius of the wetted area grows as a function of time which reflects the force balance during the spreading. The influences of the intensity of magnetic field and the contact angle on the velocity of the triple-phase contact line will be summarized. These results are useful in control the flow patterns in microdevice.

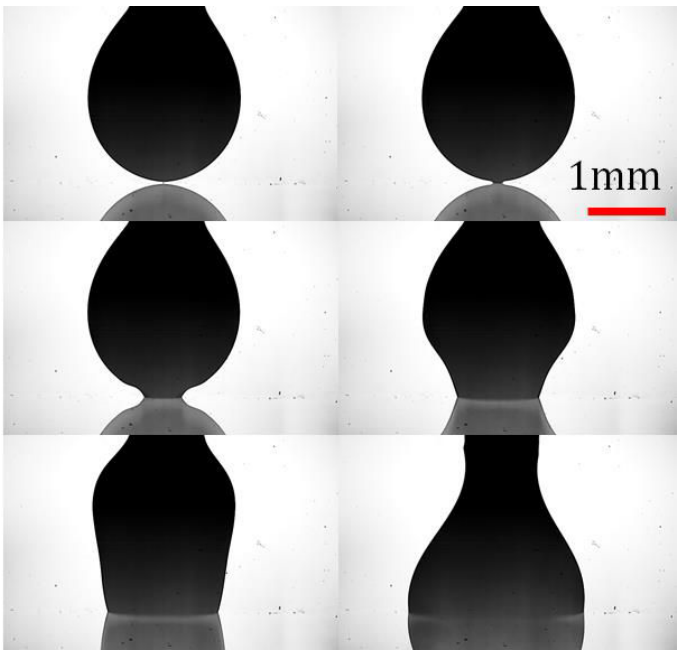

(a)

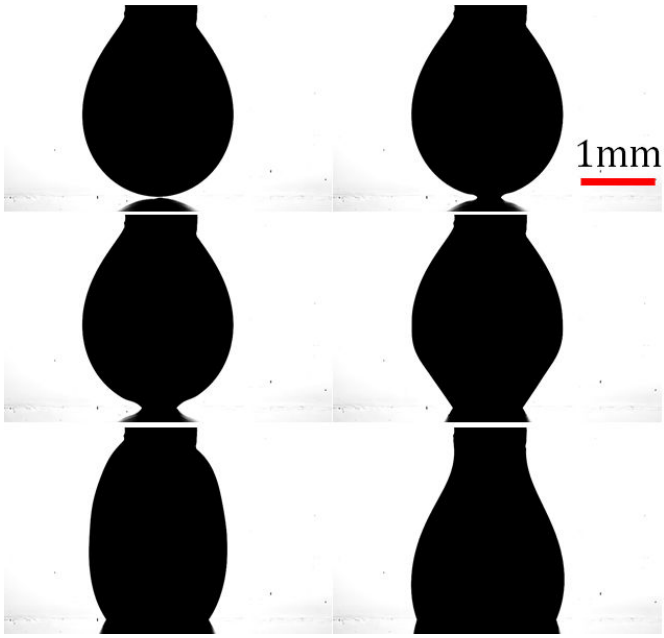

(b)

Fig.7.5 Series of snapshots of the side view of ferrofluid drop spreading on a (a) glass and (b) Teflon substrate.

.

Nomenclature

Acronyms

Chapter 3

NM	No magnetic field
RM	radial magnetic field
AM	axial magnetic field
NdFeB	neodymium iron boron

Chapter 4

SDS	sodium dodecyl sulfate
UM	uniform magnetic field
NM	no magnetic field
BPO	breakup with permanent obstruction
BTO	breakup with temporary obstruction
BNO	breakup without obstruct
NB	non-breakup
NS	unstable breakup
μ-PIV	micro-Particle Image Velocimetry

Chapter 5

BR	tip stream region
NR	non-tip stream

Chapter 6

VOF	volume of fluid
PLIC-VOF	piecewise linear interface representation
PISO	pressure-implicit with splitting of operators
PRESTO!	pressure staggering options
CSF	continuum surface force

Mathematical Symbols

Chapter 3

V_m	droplet volume with magnetic field
V_n	droplet volume without magnetic field
B	magnetic flux density (Mt)
Q_c	flow rate of continuous phase (μL/min)
Q_d	flow rate of the water-based ferrofluid (μL/min)
W_l	maximum width of the expanding tip (μm)
W_s	minimum width of the thinning neck (μm)
W_c	channel width (μm)
L_d	length of the dispersed thread in the outlet channel (μm)
$[-(t-t_c)]$	remaining time (ms)

S_d	area occupied by droplet
S_c	accessible area by the continuous phase in the channel
V_d	instantaneous velocity (mm/s)
T_S	time zero
T_E	terminal point
V_t	total superficial velocity (mm/s)
Chapter 4	
b	major axis of droplet
a	minor axis of droplet
H	magnetic field strength
W_n	minimum width of the thinning neck (μm)
W_c	width of the channel (μm)
d / W_c	minimum dimensionless width of the tunnel
V_R	droplet volume in the right branch
V_L	droplet volume in the right branch
Q_t	total flow rate of both phases (μL/min)
U_R	flow rate in the right branch (μL/min)
U_L	flow rate in the right branch (μL/min)
t_L	time for the first one of the two daughter bubbles flowing through the outlet of the loop (ms)
t_d	time difference of the two daughter bubbles arriving at the T-junction convergence (ms)
L_B	length of the first one of the two daughter bubbles passing through the outlet
U_A	average velocity of the first one of the two daughter bubbles passing through the outlet (m/s)
L	branch length of the loop
V_1	velocity of the bubble in the left branch (m/s)
V_2	velocity of the bubble in the right branch (m/s)
Q_G	gas flow rate (mL/min)
Q_L	liquid flow rate (mL/min)
L_1, L_2	length of the two daughter bubbles
t	time after the mother bubble reaches the entrance of the loop (ms)
ΔX_1	increased lengths of the breaking bubble in left branch
ΔX_2	increased lengths of the breaking bubble in right branch
U	average two phase flow speed in the main channel
t_c	time (ms)
ΔP	difference in pressure
R	fluidic resistance
Q	volumetric rate of flow
U_b	velocity of the bubble in gutter (m/s)
U_g	velocity of the liquid in gutter (m/s)
W_f	width of liquid film (μm)
Q_g	volumetric flow rates in gutters (μL/min)

A_c	cross-sectional area of the microchannel
A_b	cross-sectional area of the bubble
A_g	cross-sectional area of the gutter
ΔP_g	pressure drop across gutter
ΔP_b	pressure drop across bubble
R_g	hydrodynamic resistance of gutter
Q_c	critical flow rate (μL/min)
Chapter 5	
Q_c	flow rate of continuous phase (μL/min)
W_c	channel width (μm)
L	particle length (μm)
U_c	continuous phase superficial velocity (ms^{-1})
P_c	capillary pressure
L_μ	viscous length scale
t	remaining time (ms)
V_n	volume of the neck filament (μm^3)
V_s	total volume of the satellite droplets (μm^3)
L_d	droplet size (μm)
U	two-phase superficial velocity (ms^{-1})
R	width of the droplet body (μm)
L	dimensionless droplet length
L_c	critical dimensionless droplet length
L_m	maximum dimensionless extent of the tail
L_t	dimensionless extent of the tip stream (μm)
Chapter 6	
l_c	characteristic length
n	unit normal vector on the interface
D	distance between needle tip and ferrofluid cusp (mm)
L_b	microbubble size (μm)
k	gas/liquid flow rate ratio
Q_G	flow rate of gas (mL/h)
Q_L	flow rate of liquid (mL/h)
U_b	superficial velocity in each of the branches (m/s)
t_L	time for the two daughter bubbles flowing through the outlet of the loop (ms)
U_A	average velocity of the two daughter bubbles passing through the outlet (m/s)
L_B	decrease of the bubble size (μm)
r	neck width (mm)
U_n	velocity for the squeezing coalescence (m/s)
m	mass of the thin film
a	acceleration speed
t_c	bubbles contact time (ms)
t_d	film drainage time (ms)

h_i	initial film thickness (µm)
h_f	final film thickness before fusion (µm)
u_t	relative velocity between bubbles
L_c	distance traveled by the bubble pair from collision to coalescence
u_a	average velocity of the bubble pair during the process (m/s)
W_n	minimum width of the expanding neck (µm)
D_c	curvature diameter of the droplet tip just before the formation of the neck
V	average approaching velocity of the two droplets (m/s)
L_N	position (µm)
t_0	the time pinch-off occurs
R_r	radius of curvature of droplet rear
R_h	radius of curvature of droplet head
P	pressure

Greek letters

Chapter 3

χ	initial susceptibility of the ferrofluid
ρ_d	density of the ferrofluid (kg.m^{-3})
μ_d	viscosity of the ferrofluid (mPa.s)
ρ_c	density of the continuous phase (kg.m^{-3})
μ_c	viscosity of the continuous phase (mPa.s)
σ	interfacial tension between the ferrofluid and mineral oil (mN.m^{-1})
μ_0	permeability of the free space (N/A^2)

Chapter 4

λ	spacing between droplets (µm)
Λ	ratio of two branches length
μ_l	viscosity of the liquid phase (mPa.s)
ε	dimensionless bubble size
δ	thickness of liquid film between bubble surface and microchannel wall (µm)
φ	difference in length of two daughter bubbles

Chapter 5

ρ	density of the liquid (kg m^{-3})
μ	viscosity of the liquid (mPa s)
μ_c	continuous phase viscosity (mPa s)
μ_d	disperse phase viscosity (mPa s)
ρ_d	density of the disperse phase (kg m^{-3})
φ	ratio of the two phases flow rates
μ_l	viscosity of the mineral oil (mPa s)
σ_g	surface tension of bubble (mN m^{-1})
σ_l	surface tension of droplet (mN m^{-1})

Chapter 6

μ_0	permeability of the free space (N/A^2)

Ωq	corresponding variable volume fraction
Ω_G	volume fraction of gas
Ω_L	volume fraction of liquid
κ	radius of curvature
$\delta(r)$	Dirac delta function
θ	contact angle (°)
ρ_d	density of the ferrofluid (kg.m^{-3})
μ_d	viscosity of the ferrofluid (mPa.s)
λ	efficiency of bubble coalescence
ρ_c	density of the continuous phase (kg m^{-3})

Dimensionless groups

Chapter 3

Re_c	Reynolds number of the continuous phase
Bo	Bond number

Chapter 4

Ca	capillary number

Chapter 6

Ca_c	critical capillary number
We	Weber number

References

[1]Jensen K F. Microreaction engineering -- is small better? Chemical Engineering Science, 2001, 56(2): 293-303.

[2]Whitesides G M. The origins and the future of microfluidics. Nature, 2006, 442(7101): 368-373.

[3]Haeberle S, Zengerle R. Microfluidic platforms for lab-on-a-chip applications. Lab on a Chip, 2007, 7(9): 1094-1110.

[4]Schulte T H, Bardell R L, Weigl B H. Microfluidic technologies in clinical diagnostics. Clinica Chimica Acta, 2002, 321(1-2): 1-10.

[5]Dittrich P S, Manz A. Lab-on-a-chip: microfluidics in drug discovery. Nature Reviews Drug Discovery, 2006, 5(3): 210-218.

[6]Günther A, Jensen K F. Multiphase microfluidics: From flow characteristics to chemical and materials synthesis. Lab on a Chip, 2006, 6(12): 1487-1503.

[7]Marre S, Jensen K F. Synthesis of micro and nanostructures in microfluidic systems. Chemical Society Reviews, 2010, 39(3): 1183-1202.

[8]Pregibon D C, Toner M, Doyle P S. Multifunctional encoded particles for high-throughput biomolecule analysis. Science, 2007, 315(5817): 1393-1396.

[9]Mason T G, Bibette J. Emulsification in Viscoelastic Media. Physical Review Letters, 1996, 77(16): 3481.

[10]Utada A S, Lorenceau E, Link D R. Monodisperse double emulsions generated from a microcapillary device. Science, 2005, 308(5721): 537-541.

[11]Nie Z H, Seo M S, Xu S Q. Emulsification in a microfluidic flow-focusing device: effect of the viscosities of the liquids. Microfluidics and Nanofluidics, 2008, 5(5): 585-594.

[12]Steegmans M L J, Schroen K G P H, Boom R M. Microfluidic Y-junctions: A robust emulsification system with regard to junction design. AIChE Journal, 2010, 56(7): 1946-1949.

[13]Adams L L A, Kodger T E, Kim S-H. Single step emulsification for the generation of multi-component double emulsions. Soft Matter, 2012, 8：10719-10724

[14]Dangla R, Fradet E, Lopez Y. The physical mechanisms of step emulsification. Journal of Physics D: Applied Physics, 2013, 46(11): 114003.

[15] Stroock A D, Dertinger S K W, Ajdari A. Chaotic mixer for microchannels. Science, 2002, 295(5555): 647-651.

[16] Bothe D, Stemich C, Warnecke H-J. Fluid mixing in a T-shaped micro-mixer. Chemical Engineering Science, 2006, 61(9): 2950-2958.

[17] Verma M K S, Ganneboyina S R, Vinayak R R. Three-dimensional multihelical microfluidic mixers for rapid mixing of liquids. Langmuir, 2008, 24(5): 2248-2251.

[18] Günther A, Jhunjhunwala M, Thalmann M. Micromixing of miscible liquids in segmented gas-liquid flow. Langmuir, 2005, 21(4): 1547-1555.

[19] Che Z, Wong T N, Nguyen N-T. Heat transfer in plug flow in cylindrical microcapillaries with constant surface heat flux. International Journal of Thermal Sciences, 2013, 64: 204-212.

[20] Che Z, Wong T N, Nguyen N-T. Heat transfer enhancement by recirculating flow within liquid plugs in microchannels. International Journal of Heat and Mass Transfer, 2012, 55(7–8): 1947-1956.

[21] Wang K, Lu Y, Shao H. Heat-transfer performance of a Liquid−Liquid microdispersed system. Industrial and Engineering Chemistry Research, 2008, 47(23): 9754-9758.

[22] Wang K, Lu Y C, Xia Y. Kinetics research on fast exothermic reaction between cyclohexanecarboxylic acid and oleum in microreactor. Chemical Engineering Journal, 2011, 169(1-3): 290-298.

[23] Kreutzer M T, Kapteijn F, Moulijn J A. Multiphase monolith reactors: Chemical reaction engineering of segmented flow in microchannels. Chemical Engineering Science, 2005, 60(22): 5895-5916.

[24] Rayleigh L. On the Capillary Phenomena of Jets. Proceedings of the Royal Society of London, 1879, 29(196-199): 71-97.

[25] Taylor G I. The Viscosity of a fluid containing small drops of another fluid. Proceedings of the Royal Society of London Series A, 1932, 138(834): 41-48.

[26] Bretherton F P. The motion of long bubbles in tubes. Journal of Fluid Mechanics, 1961, 14: 3127-3134

[27] Stone H A, Kim S. Microfluidics: Basic issues, applications, and challenges. AIChE Journal, 2001, 47(6): 1250-1254.

[28] Sinton D. Energy: the microfluidic frontier. Lab on a Chip, 2014, 14:3127-3134.

[29] Ghaini A, Kashid M N, Agar D W. Effective interfacial area for mass transfer in the liquid-liquid slug flow capillary microreactors. Chemical Engineering and

Processing: Process Intensification, 2010, 49(4): 358-366.

[30] Haase S, Bauer T. New method for simultaneous measurement of hydrodynamics and reaction rates in a mini-channel with Taylor flow. Chemical Engineering Journal, 2011, 176-177: 65-74.

[31] Sarrazin F, Prat L, Di Miceli N. Mixing characterization inside microdroplets engineered on a microcoalescer. Chemical Engineering Science, 2007, 62(4): 1042-1048.

[32] Fu T, Wu Y, Ma Y. Droplet formation and breakup dynamics in microfluidic flow-focusing devices: From dripping to jetting. Chemical Engineering Science, 2012, 84: 207-217.

[33] Fu T, Ma Y, Funfschilling D. Breakup dynamics of slender bubbles in non-newtonian fluids in microfluidic flow-focusing devices. AIChE Journal, 2012, 58(11): 3560-3567.

[34] Wang X, Zhu C, Fu T. Critical lengths for the transition of bubble breakup in microfluidic T-junctions. Chemical Engineering Science, 2014, 111: 244-254.

[35] Wu Y, Fu T, Zhu C. Bubble coalescence at a microfluidic T-junction convergence: from colliding to squeezing. Microfluidics and Nanofluidics, 2014, 16(1-2): 275-286.

[36] Lu Y, Fu T, Zhu C. Pinch-off mechanism for Taylor bubble formation in a microfluidic flow-focusing device. Microfluidics and Nanofluidics, 2014, 16(6): 1047-1055.

[37] Baroud C N, Willaime H. Multiphase flows in microfluidics. Comptes Rendus Physique, 2004, 5(5): 547-555.

[38] Squires T M, Quake S R. Microfluidics: Fluid physics at the nanoliter scale. Reviews of Modern Physics, 2005, 77(3): 977-1026.

[39] Teh S Y, Lin R, Hung L H. Droplet microfluidics. Lab on a Chip, 2008, 8(2): 198-220.

[40] Stone H A. Interfaces: in fluid mechanics and across disciplines. Journal of Fluid Mechanics, 2010, 645: 1-25.

[41] Paulsen J D, Burton J C, Nagel S R. Viscous to inertial crossover in liquid drop coalescence. Physical Review Letters, 2011, 106(11): 114501.

[42] Ehrfeld W, Hessel V, Lowe H. Microreactors-New technology for medern chemistry [M]. Weinheim: WILEY-VCH, 2000.

[43] Barbier V, Willaime H, Tabeling P. Producing droplets in parallel microfluidic systems. Physical Review E, 2006, 74(4): 046306.

[44] Dreyfus R, Tabeling P, Willaime H. Ordered and disordered patterns in two-phase flows in microchannels. Physical Review Letters, 2003, 90(14): 144505.

[45] Anna S L, Bontoux N, Stone H A. Formation of dispersions using "flow focusing" in microchannels. Applied Physics Letters, 2003, 82(3): 364-366.

[46] Cramer C, Fischer P, Windhab E J. Drop formation in a co-flowing ambient fluid. Chemical Engineering Science, 2004, 59(15): 3045-3058.

[47] Cramer C, Studer S, Windhab E J. Periodic dripping dynamics in a co-flowing liquid-liquid system. Physics of Fluids, 2012, 24(9): 093101.

[48] Guillot P, Ajdari A, Goyon J. Droplets and jets in microfluidic devices. Comptes Rendus Chimie, 2009, 12(1-2): 247-257.

[49] Guillot P, Colin A, Ajdari A. Stability of a jet in confined pressure-driven biphasic flows at low Reynolds number in various geometries. Physical Review E, 2008, 78(1): 016307.

[50] Guillot P, Colin A, Utada A S. Stability of a jet in confined pressure-driven biphasic flows at low Reynolds numbers. Physical Review Letters, 2007, 99(10): 104502.

[51] Thorsen T, Roberts R W, Arnold F H. Dynamic pattern formation in a vesicle-generating microfluidic device. Physical Review Letters, 2001, 86(18): 4163-4166.

[52] Afkhami S, Leshansky A M, Renardy Y. Numerical investigation of elongated drops in a microfluidic T-junction. Physics of Fluids, 2011, 23(2): 022002.

[53] Garstecki P, Fuerstman M J, Stone H A. Formation of droplets and bubbles in a microfluidic T-junction - Scaling and mechanism of break-up. Lab on a Chip, 2006, 6(3): 437-446.

[54] van Steijn V, Kreutzer M T, Kleijn C R. μ-PIV study of the formation of segmented flow in microfluidic T-junctions. Chemical Engineering Science, 2007, 62(24): 7505-7514.

[55] Xu J H, Li S W, Wang Y J. Controllable gas-liquid phase flow patterns and monodisperse microbubbles in a microfluidic T-junction device. Applied Physics Letters, 2006, 88(13): 133506.

[56] Christopher G F, Anna S L. Microfluidic methods for generating continuous droplet streams. Journal of Physics D:Applied Physics, 2007, 40: R319-R336.

[57] de Menech M, Garstecki P, Jousse F. Transition from squeezing to dripping in a microfluidic T-shaped junction. Journal of Fluid Mechanics, 2008, 595: 141-161.

[58] de Menech M. Modeling of droplet breakup in a microfluidic T-shaped junction with a phase-field model. Physical Review E, 2006, 73(3): 031505.

[59] Gupta A, Kumar R. Effect of geometry on droplet formation in the squeezing regime in a microfluidic T-junction. Microfluidics and Nanofluidics, 2009, 8 (6): 799-812

[60] van der Graaf S, Nisisako T, Schroën C G P H. Lattice Boltzmann simulations of droplet formation in a T-shaped microchannel. Langmuir, 2006, 22(9): 4144-4152.

[61] Xu J H, Li S W, Tan J. Correlation of droplet formation in T-junction microfluidic devices:from squeezing to dripping. Microfluidics and Nanofluidics, 2008, 5(711-717.

[62] Cimpeanu R, Papageorgiou D T, Petropoulos P G. On the control and suppression of the Rayleigh-Taylor instability using electric fields. Physics of Fluids, 2014, 26(2): 022105.

[63] Taylor G. Disintegration of water drops in an electric field. Proceedings of the Royal Society of London Series A: Mathematical and Physical Sciences, 1964, 280(1382): 383-397.

[64] Zhang X, Basaran O A. Dynamics of drop formation from a capillary in the presence of an electric field. Journal of Fluid Mechanics, 1996, 326: 239-263.

[65] Notz P K, Basaran O A. Dynamics of drop formation in an electric field. Journal of Colloid and Interface Science, 1999, 213(1): 218-237.

[66] Collins R T, Jones J J, Harris M T. Electrohydrodynamic tip streaming and emission of charged drops from liquid cones. Nature Physics, 2008, 4(2): 149-154.

[67] He P, Kim H, Luo D. Low-frequency ac electro-flow-focusing microfluidic emulsification. Applied Physics Letters, 2010, 96(17): 174103.

[68] Link D R, Grasland-Mongrain E, Duri A. Electric control of droplets in microfluidic devices. Angewandte Chemie International Edition, 2006, 45(16): 2556-2560.

[69] Kim H, Luo D, Link D. Controlled production of emulsion drops using an electric field in a flow-focusing microfluidic device. Applied Physics Letters, 2007, 91(13): 133106.

[70] Gu H, Malloggi F, Vanapalli S, A. Electrowetting-enhanced microfluidic device for drop generation. Applied Physics Letters, 2008, 93(18): 183507.

[71] Tan S H, Nguyen N T. Generation and manipulation of monodispersed ferrofluid emulsions: The effect of a uniform magnetic field in flow-focusing and T-junction configurations. Physical Review E, 2011, 84(3): 036317

[72] Tan S-H, Nguyen N-T, Yobas L. Formation and manipulation of ferrofluid droplets at a microfluidic T-junction. Journal of Micromechanics and Microengineering, 2010, 20(4): 045004.

[73] Wu Y, Fu T, Ma Y. Ferrofluid droplet formation and breakup dynamics in a microfluidic flow-focusing device. Soft Matter, 2013, 9(41): 9792-9798.

[74] Baroud C N, Delville J-P, Gallaire F. Thermocapillary valve for droplet production and sorting. Physical Review E, 2007, 75(4): 046302.

[75] Bransky A, Korin N, Khoury M. A microfluidic droplet generator based on a piezoelectric actuator. Lab on a Chip, 2009, 9(4): 516-520

[76] Stone H A. Dynamics of drop deformation and breakup in viscous fluids. Annual Review of Fluid Mechanics, 1994, 26: 65-102.

[77] Link D R, Anna S L, Weitz D A. Geometrically mediated breakup of drops in microfluidic devices. Physical Review Letters, 2004, 92(5): 054503.

[78] Leshansky A M, Pismen L M. Breakup of drops in a microfluidic T junction. Physics of Fluids, 2009, 21(2): 023303.

[79] Cristini V, Tan Y C. Theory and numerical simulation of droplet dynamics in complex flows - A review. Lab on a Chip, 2004, 4(4): 257-264.

[80] Yamada M, Doi S, Maenaka H. Hydrodynamic control of droplet division in bifurcating microchannel and its application to particle synthesis. Journal of Colloid and Interface Science, 2008, 321(2): 401-407.

[81] Salkin L, Courbin L, Panizza P. Microfluidic breakups of confined droplets against a linear obstacle: The importance of the viscosity contrast. Physical Review E, 2012, 86(3): 036317.

[82] Wu Y, Fu T, Ma Y. Active control of ferrofluid droplet breakup dynamics in a microfluidic T-junction. Microfluidics and Nanofluidics, 2015, 18(1): 19-27.

[83] Fu T, Ma Y, Li H Z. Hydrodynamic feedback on bubble breakup at a T-junction within an asymmetric loop. AIChE Journal, 2014, 60(5): 1920-1929.

[84] Wu Y, Fu T, Zhu C. Asymmetrical breakup of bubbles at a microfluidic T-junction divergence: feedback effect of bubble collision. Microfluidics and Nanofluidics, 2012, 13(5): 723-733.

[85] Adamson D N, Mustafi D, Zhang J X J. Production of arrays of chemically distinct nanolitre plugs via repeated splitting in microfluidic devices. Lab on a Chip, 2006, 6: 1178 -1186.

[86] Belloul M, Engl W, Colin A. Competition between local collisions and collective

hydrodynamic feedback controls traffic flows in microfluidic networks. Physical Review Letters, 2009, 102(19): 194502.

[87] Sessoms D A, Amon A, Courbin L. Complex dynamics of droplet traffic in a bifurcating microfluidic channel: periodicity, multistability, and selection rules. Physical Review Letters, 2010, 105(15): 154501.

[88] Sessoms D A, Belloul M, Engl W. Droplet motion in microfluidic networks: Hydrodynamic interactions and pressure-drop measurements. Physical Review E, 2009, 80(1): 016317.

[89] Song Y, Manneville P, Baroud C N. Local interactions and the global organization of a two-phase flow in a branching tree. Physical Review Letters, 2010, 105(13): 134501.

[90] Fu T, Ma Y, Funfschilling D. Bubble formation and breakup mechanism in a microfluidic flow-focusing device. Chemical Engineering Science, 2009, 64(10): 2392-2400.

[91] Carrier O, Dervin E, Funfschilling D. Formation of satellite droplets in flow-focusing junctions: volume and neck rupture. Microsystem Technologies, 2013,21(3): 499-507.

[92] Tan Y C, Fisher J S, Lee A I. Design of microfluidic channel geometries for the control of droplet volume, chemical concentration, and sorting. Lab on a Chip, 2004, 4(4): 292-298.

[93] Tan Y-C, Lee A P. Microfluidic separation of satellite droplets as the basis of a monodispersed micron and submicron emulsification system. Lab on a Chip, 2005, 5(10): 1178-1183.

[94] Mulligan M K, Rothstein J P. The effect of confinement-induced shear on drop deformation and breakup in microfluidic extensional flows. Physics of Fluids, 2011, 23(2): 022044.

[95] Anna S L, Mayer H C. Microscale tipstreaming in a microfluidic flow focusing device. Physics of Fluids, 2006, 18(12): 121512.

[96] Basaran O A. Small-scale free surface flows with breakup: Drop formation and emerging applications. AIChE Journal, 2002, 48(9): 1842-1848.

[97] Paulsen J D. Approach and coalescence of liquid drops in air. Physical Review E, 2013, 88(6): 063010.

[98] Paulsen J D, Burton J C, Nagel S R. The inexorable resistance of inertia determines the initial regime of drop coalescence. Proceedings of the National

Academy of Sciences of the United States of America, 2012, 109(18): 6857-6861.
[99]Paulsen J D, Carmigniani R, Kannan A. Coalescence of bubbles and drops in an outer fluid. Nature Communications, 2014, 5(3182.
[100] Yang L, Wang K, Tan J. Experimental study of microbubble coalescence in a T-junction microfluidic device. Microfluidics and Nanofluidics, 2012, 12(5): 715-722.
[101] Wang K, Lu Y, Tostado C P. Coalescences of microdroplets at a cross-shaped microchannel junction without strictly synchronism control. Chemical Engineering Journal, 2013, 277: 90-96
[102] Wang K, Lu Y, Yang L. Microdroplet coalescences at microchannel junctions with different collision angles. AIChE Journal, 2013, 59(2): 643-649.
[103] Eggers J, Lister J R, Stone H A. Coalescence of Liquid Drops. Journal of Fluid Mechanics, 1999, 401: 293-310.
[104] Liao Y, Lucas D. A literature review on mechanisms and models for the coalescence process of fluid particles. Chemical Engineering Science, 2010, 65(10): 2851-2864.
[105] Wang K, Lu Y C, Xu J H. Generation of micromonodispersed droplets and bubbles in the capillary embedded T-junction microfluidic devices. AIChE Journal, 2011, 57(2): 299-306.
[106] Bremond N, Thiam A R, Bibette J. Decompressing Emulsion Droplet Favors Coalescence. Physical Review Letters, 2008, 100(2): 024501.
[107] Niu X, Gulati S, Edel J B. Pillar-induced droplet merging in microfluidic circuits. Lab on a Chip, 2008, 8(11): 1837-1841.
[108] Ristenpart W D, Bird J C, Belmonte A. Non-coalescence of oppositely charged drops. Nature, 2009, 461(7262): 377-380.
[109] Priest C, Herminghaus S, Seemann R. Controlled electrocoalescence in microfluidics: Targeting a single lamella. Applied Physics Letters, 2006, 89(13): 134101.
[110] Baroud C N, de Saint Vincent M R, Delville J-P. An optical toolbox for total control of droplet microfluidics. Lab on a Chip, 2007, 7(8): 1029-1033.
[111] Pandey R, Conrad J C. Effects of attraction strength on microchannel flow of colloid-polymer depletion mixtures. Soft Matter, 8(41):2012,
[112] Stark J, Manga M. The motion of long bubbles in a network of tubes. Transport in Porous Media, 2000, 40(2): 201-218.
[113] Eggers J, Smith A F. Free streamline flows with singularities. Journal of Fluid

Mechanics, 2010, 647: 187-200.
[114] Eggers J, Fontelos M A. Isolated inertialess drops cannot break up. Journal of Fluid Mechanics, 2005, 530: 177-180.
[115] Beyzavi A, Nguyen N-T. Programmable two-dimensional actuation of ferrofluid droplet using planar microcoils. Journal of Micromechanics and Microengineering, 2010, 20(1): 015018.
[116] Thoroddsen S T, Takehara K, Etoh T G. Micro-splashing by drop impacts. Journal of Fluid Mechanics, 2012, 706: 560-570.
[117] Sadhal S S. Acoustofluidics 16: acoustics streaming near liquid-gas interfaces: drops and bubbles. Lab on a Chip, 2012, 12(16): 2771-2781.
[118] Thoroddsen S T, Etoh T G, Takehara K. High-speed imaging of drops and bubbles. Annual Review of Fluid Mechanics, 2008, 40: 257-285.
[119] Chaudhuri P, Mansard V, Colin A. Dynamical flow arrest in confined gravity diven flows of soft jammed particles. Physical Review Letters, 2012, 109(3): 036001.
[120] Eggers J. Drop formation - an overview. Journal of Applied Mathmatics and Mechanics, 2005, 85(6): 400-410.
[121] Quintero N V, Song Y, Manneville P. Behavior of liquid plugs at bifurcations in a microfluidic tree network. Biomicrofluidics, 2012, 6(3): 034105.
[122] Sobieszuk P, Aubin J, Pohorecki R. Hydrodynamics and mass transfer in gas-liquid flows in microreactors. Chemical Engineering & Technology, 2012, 35(8): 1346-1358.
[123] Li S B, Ma Y G, Fu T T. The viscosity distribution around a rising bubble in shear-thinning non-newtonian fluids. Brazilian Journal of Chemical Engineering, 2012, 29(2): 265-274.
[124] Mefford O T, Woodward R C, Goff J D. Field-induced motion of ferrofluids through immiscible viscous media: Testbed for restorative treatment of retinal detachment. Journal of Magnetism and Magnetic Materials, 2007, 311(1): 347-353.
[125] Hessel V, Vural Gürsel I, Wang Q. Potential analysis of smart flow processing and micro process technology for fastening process development: Use of chemistry and process design as intensification fields. Chemical Engineering & Technology, 2012, 35(7): 1184-1204.
[126] Fu T, Wu Y, Ma Y. Droplet formation and breakup dynamics in microfluidic flow-focusing devices: From dripping to jetting. Chemical Engineering Science, 2012, 84: 207-217.

[127] Dollet B, van Hoeve W, Raven J-P. Role of the channel geometry on the bubble pinch off in flow focusing devices. Physical Review Letters, 2008, 100(3): 034504.

[128] Cubaud T, Mason T G. Capillary threads and viscous droplets in square microchannels. Physics of Fluids, 2008, 20(5): 053302.

[129] Belloul M, Courbin L, Panizza P. Droplet traffic regulated by collisions in microfluidic networks. Soft Matter, 2011, 7(19): 9453-9458.

[130] Jullien M C, Tsang Mui Ching M J, Cohen C. Droplet breakup in microfluidic T-junctions at small capillary numbers. Physics of Fluids, 2009, 21(7): 072001.

[131] Leshansky A M, Afkhami S, Jullien M C. Obstructed breakup of slender drops in a microfluidic T junction. Physical Review Letters, 2012, 108(26): 264502.

[132] Shao N, Gavriilidis A, Angeli P. Mass transfer during Taylor flow in microchannels with and without chemical reaction. Chemical Engineering Journal, 2010, 160(3): 873-881.

[133] Abate A R, Weitz D A. Faster multiple emulsification with drop splitting. Lab on a Chip, 2011, 11(11): 1911-1915.

[134] Ghaini A, Mescher A, Agar D W. Hydrodynamic studies of liquid-liquid slug flows in circular microchannels. Chemical Engineering Science, 2011, 66(6): 1168-1178.

[135] Seemann R, Brinkmann M, Pfohl T. Droplet based microfluidics. Reports on Progress in Physics, 2012, 75(1): 016601.

[136] Duncanson W, Lin T, Abate A R. Microfluidic synthesis of advanced microparticles for encapsulation and controlled release. Lab on a Chip, 2012, 12(12): 2135-2145.

[137] Salkin L, Schmit A, Courbin L. Passive breakups of isolated drops and one-dimensional assemblies of drops in microfluidic geometries: experiments and models. Lab on a Chip, 2013, 13(15): 3022-3032.

[138] Carrier O, Funfschilling D, Li H Z. Effect of the fluid injection configuration on droplet size in a microfluidic T junction. Physical Review E, 2014, 89(1): 013003.

[139] Glawdel T, Elbuken C, Ren C L. Droplet formation in microfluidic T-junction generators operating in the transitional regime. I. Experimental observations. Physical Review E, 2012, 85(1): 016322.

[140] Glawdel T, Elbuken C, Ren C L. Droplet formation in microfluidic T-junction generators operating in the transitional regime. II. Modeling. Physical Review E, 2012, 85(1): 016323.

[141] Wang W, Xie R, Ju X-J. Controllable microfluidic production of multicomponent multiple emulsions. Lab on a Chip, 2011, 11(9): 1587-1592.

[142] Ganan-Calvo A M, Riesco-Chueca P. Jetting-dripping transition of a liquid jet in a lower viscosity co-flowing immiscible liquid: the minimum flow rate in flow focusing. Journal of Fluid Mechanics, 2006, 553: 75-84.

[143] Ward T, Faivre M, Stone H A. Drop production and tip-streaming phenomenon in a microfluidic flow-focusing device via an interfacial chemical reaction. Langmuir, 2010, 26(12): 9233-9239.

[144] Christopher G F, Noharuddin N N, Taylor J A. Experimental obervations of the squeezing-to-dripping transition in T-shaped microfluidic junctions. Physical Review E, 2008, 78: 036317.

[145] Cordero M L, Gallaire F, Baroud C N. Quantitative analysis of the dripping and jetting regimes in co-flowing capillary jets. Physics of Fluids, 2011, 23(9): 094111.

[146] Li J, Chen H, Stone H A. Breakup of double emulsion droplets in a tapered nozzle. Langmuir, 2011, 27(8) 4324-4327.

[147] Utada A S, Chu L Y, Fernandez-Nieves A. Dripping, jetting, drops, and wetting: The magic of microfluidics. MRS Bulletin, 2007, 32(9): 702-708.

[148] Bedram A, Moosavi A. Droplet breakup in an asymmetric microfluidic T junction. European Physical Journal E, 2011, 34(8): 78.

[149] Hoang D A, Portela L M, Kleijn C R. Dynamics of droplet breakup in a T-junction. Journal of Fluid Mechanics, 2013, 717:R4.

[150] Samie M, Salari A, Shafii M B. Breakup of microdroplets in asymmetric T junctions. Physical Review E, 2013, 87(5): 053003.

[151] Bremond N, Domejean H, Bibette J. Propagation of drop coalescence in a two-dimensional emulsion: A route towards phase inversion. Physical Review Letters, 2011, 106(21): 214502.

[152] Christopher G F, Bergstein J, End N B. Coalescence and splitting of confined droplets at microfluidic junctions. Lab on a Chip, 2009, 9: 1102-1109.

[153] He P Y, Barthes-Biesel D, Leclerc E. Flow of two immiscible liquids with low viscosity in Y shaped microfluidic systems: effect of geometry. Microfluidics and Nanofluidics, 2010, 9(2-3): 293-301.

[154] Ho P-C, Yap Y-F, Nguyen N-T. Thermally mediated droplet formation at a microfluidic T-junction. Micro and Nanosystems, 2011, 3(1): 65-75

[155] Cheung Y N, Qiu H. Characterization of acoustic droplet formation in a

microfluidic flow-focusing device. Physical Review E, 2011, 84(6): 066310.
[156] Nguyen N T. Micro-magnetofluidics: interactions between magnetism and fluid flow on the microscale. Microfluidics and Nanofluidics, 2012, 12(1-4): 1-16.
[157] Afkhami S, Tyler A J, Renardy Y. Deformation of a hydrophobic ferrofluid droplet suspended in a viscous medium under uniform magnetic fields. Journal of Fluid Mechanics, 2010, 663(358-384.
[158] Liu J, Tan S-H, Yap Y F. Numerical and experimental investigations of the formation process of ferrofluid droplets. Microfluidics and Nanofluidics, 2011, 11(2): 177-187.
[159] Liu J, Yap Y F, Nguyen N T. Numerical study of the formation process of ferrofluid droplets. Physics of Fluids, 2011, 23(7): 072008.
[160] Cybulski O, Garstecki P. Dynamic memory in a microfluidic system of droplets traveling through a simple network of microchannels. Lab on a Chip, 2010, 10(4): 484-493.
[161] Fuerstman M J, Garstecki P, Whitesides G M. Coding/decoding and reversibility of droplet trains in microfluidic networks. Science, 2007, 315(5813): 828-832.
[162] Jousse F, Farr R, Link D R. Bifurcation of droplet flows within capillaries. Physical Review E, 2006, 74(3): 036311.
[163] Parthiban P, Khan S A. Filtering microfluidic bubble trains at a symmetric junction. Lab on a Chip, 2011, 12(3): 582-588.
[164] Smith B J, Gaver D P. Agent-based simulations of complex droplet pattern formation in a two-branch microfluidic network. Lab on a Chip, 2010, 10(3): 303-312.
[165] Timgren A, Tragardh G, Tragardh C. Effects of cross-flow velocity, capillary pressure and oil viscosity on oil-in-water drop formation from a capillary. Chemical Engineering Science, 2009, 64(6): 1111-1118.
[166] Calderon A J, Fowlkes J B, Bull J L. Bubble splitting in bifurcating tubes: a model study of cardiovascular gas emboli transport. Journal of Applied Physiology, 2005, 99(2): 479-487.
[167] Hoang D A, Steijn van V, Portela L M. Benchmark numerical simulations of segmented two-phase flows in microchannels using the Volume of Fluid method. Computers & Fluids, 2013, 86: 28-36
[168] Mefford O T, Woodward R C, Goff J D. Field-induced motion of ferrofluids

through immiscible viscous media: Testbed for restorative treatment of retinal detachment. Journal of Magnetism and Magnetic Materials, 2007, 311(1): 347-353.

[169] Fuerstman M J, Lai A, Thurlow M E. The pressure drop along rectangular microchannels containing bubbles. Lab on a Chip, 2007, 7: 1479-1489.

[170] Christopher G F, Anna S L. Passive breakup of viscoelastic droplets and filament self-thinning at a microfluidic T-junction. Journal of Rheology, 2009, 53(3): 663-683.

[171] Luo R, Wang L. Liquid velocity distribution in slug flow in a microchannel. Microfluidics and Nanofluidics, 2011, 12(1-4): 581-595.

[172] Thulasidas T C, Abraham M A, Cerro R L. Bubble-train flow in capillaries of circular and square cross section. Chemical Engineering Science, 1995, 50(2): 183-199.

[173] Baroud C N, Tsikata S, Heil M. The propagation of low-viscosity fingers into fluid-filled branching networks. Journal of Fluid Mechanics, 2006, 546: 285-294.

[174] Calderon A J, Eshpuniyani B, Fowlkes J B. A boundary element model of the transport of a semi-infinite bubble through a microvessel bifurcation. Physics of Fluids, 2010, 22(6): 061902.

[175] Panizza P, Engl W, Hany C. Controlled production of hierarchically organized large emulsions and particles using assemblies on line of co-axial flow devices. Colloids and Surfaces A-Physicochemical and Engineering Aspects, 2008, 312(1): 24-31.

[176] Zhao C-X, Miller E, Cooper-White J J. Effects of fluid-fluid interfacial elasticity on droplet formation in microfluidic devices. AIChE Journal, 2011, 57(7): 1669-1677.

[177] Lu Y, Fu T, Zhu C. Scaling of the bubble formation in a flow-focusing device: Role of the liquid viscosity. Chemical Engineering Science, 2014, 105(213-219.

[178] Lister J R, Stone H A. Capillary breakup of a viscous thread surrounded by another viscous fluid. Physics of Fluids, 1998, 10(11): 2758-2764.

[179] Liao Y C, Basaran O A, Franses E I. Effects of dynamic surface tension and fluid flow on the oscillations of a supported bubble. Colloids and Surfaces a-Physicochemical and Engineering Aspects, 2006, 282(183-202.

[180] Mietus W G P, Matar O K, Lawrence C J. Droplet deformation in confined shear and extensional flow. Chemical Engineering Science, 2002, 57(7): 1217-1230.

[181] De Bruijn R A. Tipstreaming of drops in simple shear flows. Chemical

Engineering Science, 1993, 48(2): 277-284.
[182] Eggleton C D, Tsai T-M, Stebe K J. Tip streaming from a drop in the presence of surfactants. Physical Review Letters, 2001, 87(4): 048302.
[183] Moyle T M, Walker L M, Anna S L. Predicting conditions for microscale surfactant mediated tipstreaming. Physics of Fluids, 2012, 24(8): 082110.
[184] Schwartz L W, Princen H M, Kiss A D. On the motion of bubbles in capillary tubes. Journal of Fluid Mechanics, 1986, 172: 259-275.
[185] Kreutzer M T, Kapteijn F, Moulijn J A. Inertial and interfacial effects on pressure drop of Taylor flow in capillaries. AIChE Journal, 2005, 51(9): 2428-2440.
[186] de Korte R J, Schouten J C, van den Bleek C M. Controlling bubble coalescence in a fluidized-bed model using bubble injection. AIChE Journal, 2001, 47(4): 851-860.
[187] Li D. Coalescence between small bubbles: Effects of surface tension gradient and surface viscosities. Journal of Colloid and Interface Science, 1996, 181(1): 34-44.
[188] Li H Z, Mouline Y, Choplin L. Chaotic bubble coalescence in non-Newtonian fluids. International Journal of Multiphase Flow, 1997, 23(4): 713-723.
[189] Lin T-J, Lin G-M. Mechanisms of in-line coalescence of two-unequal bubbles in a non-Newtonian fluid. Chemical Engineering Journal, 2009, 155(3): 750-756.
[190] Prince M J, Blanch H W. Bubble coalescence and break-up in air-sparged bubble columns. AIChE Journal, 1990, 36(10): 1485-1499.
[191] Stover R L, Tobias C W, Denn M M. Bubble coalescence dynamics. AIChE Journal, 1997, 43(10): 2385-2392.
[192] Taki K, Tabata K, Kihara S-i. Bubble coalescence in foaming process of polymers. Polymer Engineering and Science, 2006, 46(5): 11.
[193] Case S C, Nagel S R. Coalescence in low-viscosity liquids. Physical Review Letters, 2008, 100(8): 084503.
[194] Chen D J, Cardinaels R, Moldenaers P. Effect of confinement on droplet coalescence in shear flow. Langmuir, 2009, 25(22): 12885-12893.
[195] Zagnoni M, Le Lain G, Cooper J M. Electrocoalescence mechanisms of microdroplets using localized electric fields in microfluidic channels. Langmuir, 2010, 26(18): 14443-14449.
[196] Zagnoni M, Baroud C N, Cooper J M. Electrically initiated upstream coalescence cascade of droplets in a microfluidic flow. Physical Review E, 2009, 80(4): 046303.

[197] Zhang X, Basaran O A, Wham R M. Theoretical prediction of electric field-enhanced coalescence of spherical drops. AIChE Journal, 1995, 41(7): 1629-1639.

[198] Tan Y-C, Ho Y, Lee A. Droplet coalescence by geometrically mediated flow in microfluidic channels. Microfluidics and Nanofluidics, 2007, 3(4): 495-499.

[199] Lai A, Bremond N, Stone H A. Separation-driven coalescence of droplets: an analytical criterion for the approach to contact. Journal of Fluid Mechanics, 2009, 632: 97-107.

[200] Paulsen J. Approach and coalescence of liquid drops in air. Physical Review E, 2013, 88(6): 063010.

[201] Paulsen J D, Carmigniani R, Kannan A. Coalescence of bubbles and drops in an outer fluid. Nature Communications, 2014, 5: 3182.

[202] Bird J, Ristenpart W, Belmonte A. Critical angle for electrically driven coalescence of two conical droplets. Physical Review Letters, 2009, 103(16): 164502

[203] Afkhami S, Tyler A J, Renardy Y. Deformation of a hydrophobic ferrofluid droplet suspended in a viscous medium under uniform magnetic fields. Journal of Fluid Mechanics, 2010, 663: 358-384.

[204] Nguyen N-T. Micro-magnetofluidics: interactions between magnetism and fluid flow on the microscale. Microfluidics and Nanofluidics, 2011, 12(1-4): 1-16.

[205] Tokarev A, Lee W-K, Sevonkaev I. Sharpening the surface of magnetic paranematic droplets. Soft Matter, 2014, 10(12): 1917-1923.

[206] Kadivar E. Magnetocoalescence of ferrofluid droplets in a flat microfluidic channel. Europhysics Letters, 2014, 106(2): 24003.

[207] Mahajan M P, Tsige M, Taylor P L. Paramagnetic liquid bridge in a gravity-compensating magnetic field. Physics of Fluids, 1998, 10(9): 2208-2211.

[208] Yokota M, Okumura K. Dimensional crossover in the coalescence dynamics of viscous drops confined in between two plates. Proceedings of the National Academy of Sciences of the United State of America, 2011, 108(16): 6395-6398.

[209] Yoon Y, Baldessari F, Ceniceros H D. Coalescence of two equal-sized deformable drops in an axisymmetric flow. Physics of Fluids, 2007, 19: 102102

[210] Yoon Y, Borrell M, Park C C. Viscosity ratio effects on the coalescence of two equal-sized drops in a two-dimensional linear flow. Journal of Fluid Mechanics, 2005, 525(355-379.

[211] Eggers J. Nonlinear dynamics and breakup of free-surface flows. Reviews of

Modern Physics, 1997, 69(3): 865-929.

[212] Day R F, Hinch E J, Lister J R. Self-similar capillary pinchoff of an inviscid fluid. Physical Review Letters, 1998, 80(4): 704-707.

[213] Talimi V, Muzychka Y S, Kocabiyik S. A review on numerical studies of slug flow hydrodynamics and heat transfer in microtubes and microchannels. International Journal of Multiphase Flow, 2012, 39: 88-104.

[214] Wörner M. Numerical modeling of multiphase flows in microfluidics and micro process engineering: a review of methods and applications. Microfluidics and Nanofluidics, 2012, 12(6): 841-886.

[215] Dupas J, Verneuil E, Ramaioli M, Forny L, Talini L, and Lequeux F. Dynamic wetting on thin film of soluble polymer : Effects of non-linearities in the sorption isotherm. Langmuir, 2013, 29, 12572.

Publications

1. ***Y Wu***, T Fu, C Zhu, Y Lu, Y Ma, HZ Li. Asymmetrical breakup of bubbles at a microfluidic T-junction divergence: feedback effect of bubble collision，*Microfluidics and Nanofluidics*, 2012, 13(5), 723-733.
2. T Fu, ***Y Wu***, Y Ma, HZ Li. Droplet formation and breakup dynamics in microfluidic flow-focusing devices: From dripping to jetting, *Chemical Engineering Science*, 2012, 84, 207-217.
3. ***Y Wu***, T Fu, Y Ma, HZ Li. Ferrofluid droplet formation and breakup dynamics in a microfluidic flow-focusing device, *Soft Matter*, 2013, 9, 9792-9798.
4. ***Y Wu***, T Fu, C Zhu, Y Ma, HZ Li. Bubble coalescence at a microfluidic T-junction convergence: from colliding to squeezing, *Microfluidics and Nanofluidics*, 2014, 16(1), 275-286.
5. ***Y Wu***, T Fu, Y Ma, HZ Li. Active control of ferrofluid droplet breakup dynamics in a microfluidic T-junction, *Microfluidics and Nanofluidics*, 2015, 18(1), 19-27.
6. ***Y Wu***, T Fu, C Zhu, X Wang, Y Ma, HZ Li. Shear-induced tail breakup of particles flowing in a straight microfluidic channel, *Chemical Engineering Science*, under revision.
7. ***Y Wu***, T Fu, Y Ma, HZ Li. Coalescence and breakup dynamics of ferrofluid droplets under various magnetic fields, to be submitted.
8. ***Y Wu***, T Fu, Y Ma, HZ Li. Deformation of ferrofluid droplet in the presence of a permanent magnet, to be submitted.
9. ***Y Wu***, T Fu, Y Ma, HZ Li. The formation of satellite droplets due to the breakup of neck filament at the presence of surfactants, to be submitted.

Acknowledgements

I also express my deep gratitude to my advisor (In China), Prof. Youguang Ma, I feel so glad to have you as my coach. I admire your constructive way of criticizing. I truly appreciate I can always count on your help in each aspect of work and life. In particular, many thanks for your helps in my application for permanent post. You are now and will always be my advisor.

Second to none, I would like to thank my advisor (In France), Prof. Huai-Zhi Li, for giving me the opportunity to work with him. Your expertise and passion for research, as well as their support and encouragement during my study is truly appreciated. You always be lenient to my ignorance and help me grow into a capable researcher. I feel very proud of our research work and I look forward to continue our pleasant student-teacher relationships forever.

My whole experience would not have been as rewarding without the help of other members of my lab. Many thanks to Dr. Taotao Fu, Denis Funfschilling and Chunying Zhu, who give me vast valuable advices and initiate the droplet research within our group. My gratitude goes to my fellow colleagues, Jiankai Jiang and Xiaoda Wang, that have also traversed the long and winding road of graduate studies with me. Their assistance during the whole stages of my thesis was invaluable and their outlooks on life and research were truly motivating.

Great thanks to Xiaofeng Jiang, who has tackled any job given to her with exceptional ability. I would also like to thank several other members that attended group meetings and provided valuable input with regards to my work.

I am deeply grateful to my family whose support is truly appreciated. I am very grateful to my family, my parents, Feng Wu and Cuiping Hu and my sister, Min Wu, who have been behind me all the way.